Parton distributions and small X physics

Peter John Sutton

Parton distributions and small x physics

A thesis presented for the degree of

Doctor of Philosophy

by

Peter John Sutton

University of Durham
Department of Physics
September 1992

ABSTRACT

We determine the parton distributions of the pion from a consistent next-to-leading order analysis of several high statistics $\pi^{\pm}N$ experiments including both Drell-Yan and prompt photon production. The results are compared with earlier distributions and with the predictions of lattice QCD.

We study the general behaviour of parton distributions at small x and, in particular, the predictions of the Lipatov equation. The very-small-x behaviour of the gluon distribution in a proton is obtained by solving this equation with a suitable nonlinear shadowing term incorporated. We find, with decreasing x, the emergence of an $x^{-\lambda}$ behaviour *and* the eventual taming of this singular behaviour by the shadowing term. We compare our dynamically generated gluon distribution with (i) the results of a recent next-to-leading order QCD structure function analysis which incorporated both a singular $x^{-1/2}$ behaviour and shadowing corrections, (ii) the double-leading-leading logarithm approximation (DLLA) and (iii) the semiclassical approximation of the DLLA.

Finally, we examine the proposal that deep-inelastic (x, Q^2) scattering events which contain an identified jet, with transverse momentum squared $k^2 \simeq Q^2$, allow an ideal determination of the QCD behaviour at very small x. We solve the relevant Lipatov equation to predict the shape of the jet spectrum in such events and discuss whether it will be possible to observe such jets at the HERA ep collider.

Declaration

I declare that no material in this thesis has previously been submitted for a degree at this or any other University.

All the research work in this thesis has been carried out in collaboration with Professor A. D. Martin together with contributions from Professor J. Kwiecinski, Dr. R.G. Roberts and Dr. W.J. Stirling. Material in Chapters 4,6,7 and 8 has been published in

Parton distributions for the pion extracted from Drell-Yan and prompt photon experiments
P.J. Sutton, A.D. Martin, R.G. Roberts and W.J. Stirling, *Phys. Rev.* **D45**, 2349, 1992

QCD predictions for the behaviour of the parton distributions at small x
J. Kwiecinski, A.D. Martin and P.J. Sutton *Phys. Rev.* **D44**, 2640, 1991

The small x behaviour of the gluon
J. Kwiecinski, A.D. Martin and P.J. Sutton *Phys. Lett.* **B264**, 199, 1991

Deep-inelastic events containing a measured jet as a probe of QCD behaviour at small x
J. Kwiecinski, A.D. Martin and P.J. Sutton *Phys. Rev.* **D46**, 921, 1992

Probing the Lipatov singular small x behaviour at HERA
J. Kwiecinski, A.D. Martin, P.J. Sutton *Phys. Lett.* **B287**, 254, 1992

Identifying the Lipatov $x^{-\lambda}$ behaviour at HERA
J. Kwiecinski, A.D. Martin and P.J. Sutton *Contribution to DESY Zeuthen Workshop on Deep Inelastic Scattering*, Teupitz, Germany, Apr 6—10, 1992

Acknowledgments

Firstly, I would like to thank my supervisor, Professor Alan Martin, for his patience and helpfulness over the last three years, and also Jan Kwiecinski, Dick Roberts and James Stirling for their many excellent contributions to the work presented in this thesis. Thanks also go to the many students who have helped make the top floor of the physics department such an enjoyable place to work. Of these a few deserve special mention — David Barclay, Duncan Curtis, Foster Langbein, Neil Shaban and David Summers — they have been both friends and colleagues. I was lucky enough to share an office with Foster and David B. during my three years and I will miss them both. Farewell guys, it was nice knowing you.

Amongst those outside of high-energy physics, I would like to thank Ian Smail, John Barbour, Caroline Budden, Andrew Poole, Peter Rowbotham, Lee Wilson and Paul Young. Without these people my time in Durham wouldn't have been nearly so much fun. Thanks also to fellow Londoner, David Nunn, who has proved himself to be such a good friend since our early undergraduate days.

Finally, and most importantly, I would like to thank my family for their love and encouragement throughout the last three years. Dad, Sheila, John, Sarah and Auntie Eileen have together been a continual source of strength and support — without which this thesis would not have been possible. It is to them, therefore, that I would like to dedicate this work.

Peter Sutton

Durham 1992.

Contents

1 Introduction

By the 1960s there were many reasons to believe that the hadrons (such as the proton and the pion) were not truly fundamental particles, but were made up of some other, unknown, elementary units. In 1964 Gell-mann and Zweig proposed that these units were a family of spin $\frac{1}{2}$ particles which they named quarks [1]. In their theory each hadron was composed of either three quarks or a quark and anti-quark pair. Thus the characteristic which determined the nature of each hadron was not the number of its constituent particles (unlike atomic theory), but rather the types or *flavours* of quarks from which it was constructed. For example, the proton was proposed to consist of two 'up' type quarks and a 'down' quark, whilst for a neutron the combination was two down quarks and a single up quark. However, the lack of any observations of these quarks meant that they were regarded as mathematical entities, rather than real particles. Then, in 1968, the Stanford Linear Accelerator (SLAC) began experiments with high energy electron beams fired at a target of liquid hydrogen [2]. These experiments revealed the presence of hard scattering centres within the proton, thus proving, beyond any doubt, that it truly was a composite particle. The newly discovered pieces within the proton, the so-called 'partons' [3], were quickly identified as the quarks of Gell-mann and Zweig's theory.

Despite the successes of the quark model, it still possessed several puzzling features. These included the apparent absence of multiple quark combinations such as qq, $qqqq$ and $qq\bar{q}$ as well as free quarks. A further problem was the baryon Δ^{++}, the quantum numbers

of this particle now appeared to cause a violation of the Pauli exclusion principle. These mysteries were eventually explained by the introduction of another degree of freedom — 'colour'. In this modified theory quarks carry a colour charge which is either red, green or blue. Observed particles are required to be 'colourless', that is to say, colour singlets, and so the only allowable quark combinations turn out to be exactly the triple quark and quark-antiquark configurations above. The introduction of colour led to a theory of quark interactions in which colour can be exchanged via massless bosons called gluons. The presence of these gluons, in turn, enables quark-antiquark pairs (the so-called sea quarks) to be created from the vacuum. Today, the resulting 'gauge' theory of Quantum Chromodynamics (QCD) forms part of "The Standard Model" of particle physics.

The colour force of QCD is unlike any other fundamental force in nature. The attraction that it produces between the quarks actually increases as they move further apart and decreases as they move closer together. As a result it is not possible to observe free quarks. Instead they are permanently confined within (colourless) hadrons. In order to learn about the nature of QCD from experiment it is necessary to collide a probe with an entire hadron. Only then is it possible to study the nature of the quarks contained within. Fortunately the nature of the collision is simpified by the unusual behaviour of the colour force. As we have mentioned, the force between quarks is small when they are close together and hence they can be treated as effectively free particles. This property is known as *asymptotic freedom* and means that it is possible to neglect the various interactions between the quarks when probing the hadron with a high energy particle. Figure 1.1 shows how this type of high-energy interaction can be separated out into a hard (high-energy) scattering process and a soft (low-energy) process.

The cross section thus 'factorises' into two independent pieces and may be written as

$$\sigma = \sum_i f_{i/h} \otimes \hat{\sigma}_i \tag{1.1}$$

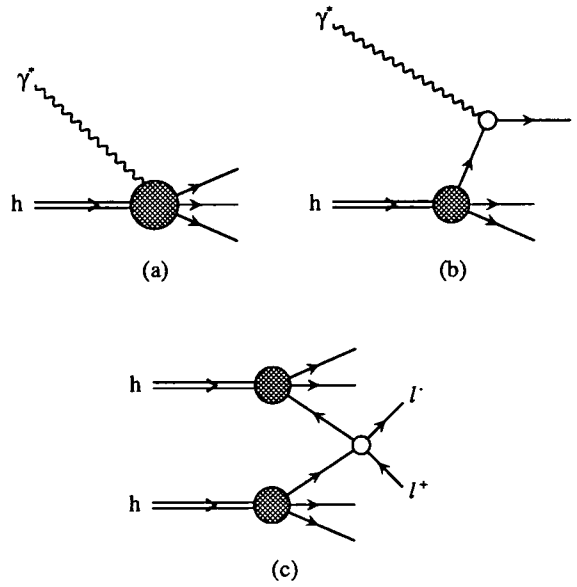

Figure 1.1. a) A diagrammatic representation of a virtual photon, γ^*, interacting with a hadron. b) In QCD the interaction 'factorises' into a hard scattering part (represented by the upper blob) and a soft part (shown shaded). The hard scattering process is independent of the hadron, h, in which the parton involved in the hard scattering, was travelling. Likewise, the soft part is independent of the hard scattering interaction. As a result, the soft part is the same for processes such as (c) the production of leptons via parton-parton annihilation.

Here $\hat{\sigma}_i$ represents the QCD subprocess relevant to the hard scattering whilst the functions $f_{i/h}$ contain the information about the soft part of the interaction. The hard scattering term, $\hat{\sigma}_i$, can be calculated using standard perturbative QCD techniques. It is free from the effects of long-distance (non-perturbative) physics and is independent of the type of hadron in which the struck quark was travelling. This information is instead contained entirely within the soft part of the interaction. Each function, $f_{i/h}$, can be interpreted as the probability of finding a parton of type i inside a hadron h and carrying a particular fraction, x, of the total hadronic momentum. These functions are known as 'the parton distributions' for the hadron and cannot be calculated within perturbation theory. Instead

it is (at present) necessary to extract them from experiment. Fortunately there is now in existence a large amount of high statistics data on hadron-hadron and hadron-lepton interactions. These data, together with the $\hat{\sigma}_i$ calculated to next-to-leading order in perturbation theory, have enabled the parton distributions to be determined to reasonable accuracy for momentum fractions, x, between $0.02 \sim 0.8$ for the proton and $0.3 \sim 0.8$ for the pion.

Whilst the hard scattering part of the interaction is independent of the parent hadron, the soft part is independent of the hard scattering interaction. As a result the parton distributions for one process are the same for all hard scattering processes. This property is known as *universality.* If we have reliable parton distributions then we can make predictions for almost any QCD processes — including those that have yet to be observed. Consider, for example, a possible mechanism for the production of a Higgs boson, shown in Fig. 1.2. If M_H is the mass of the Higgs boson produced and $\sqrt{s}$ is the centre of mass energy for the collision, then the reaction will depend on the gluons which carry a momentum fraction, $x \sim M_H/\sqrt{s}$. For a Higgs mass of around 100 GeV and an SSC energy of $\sqrt{s} = 40$ TeV this fraction is $x \sim O(10^{-3})$. A knowledge of the parton distributions in this region of low x is, therefore, very important for the prediction of such processes at future colliders. However, as we shall see, the equations which govern the behaviour of parton distributions at such small values of x are very different from those at large x.

The subject of this thesis is the parton distributions of hadrons at both large and small values of the momentum fraction, x. We examine the extraction of parton distributions from experimental data at large x, and in particular we look at the case for the pion. At small x we concern ourselves with the predictions of perturbative QCD for the parton distributions in this (as yet) unexplored region. These topics are dealt with in more-or-less independent sections. We begin in Chapter 2 at large x with a brief review of the deep-inelastic scattering process, its calculation within QCD and the nature of parton

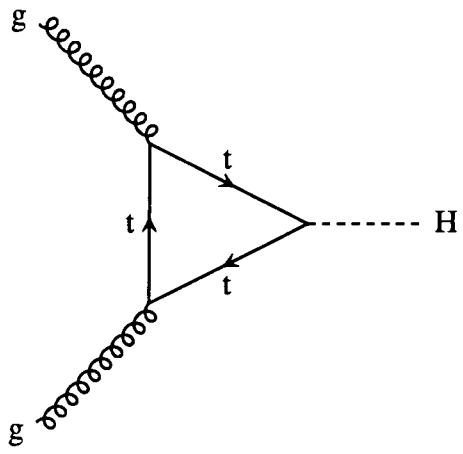

Figure 1.2. A possible process for the production of a Higgs boson.

distributions. Following this in chapter 3 we describe the Drell-Yan and prompt photon processes which, together with deep-inelastic scattering, have become the standard processes from which parton distribution data are extracted. In chapter 4 we then examine the parton distributions of the pion and extract new next-to-leading order distributions from the available high statistics (Drell-Yan and prompt photon) data. After this we turn our attention to small x physics and the QCD predictions for the parton distributions in this region. Although there are currently no data below $x \sim 10^{-2}$ for $Q^2 \gg \Lambda^2_{\rm QCD}$, this situation will soon change with the arrival of new colliders such as HERA, the LHC and SSC. It is therefore important to have reliable predictions for the behaviour of the parton distributions at small x. In Chapter 5 we review the relevant equations which govern the behaviour of parton distributions in the small x region. Then, based on these equations, we make some predictions in Chapter 6 for the gluon distribution and its shape at low values of x. In Chapters 7 and 8 we turn our attention to the future experiments which we expect to yield valuable information on the physics of small x. Finally, in Chapter 9 we give our conclusions.

2 Deep-inelastic scattering, structure functions and parton distributions

2.1 The structure of the proton

The single most important method for probing the structure of the proton is deep-inelastic scattering [4]. The basic process $lp \rightarrow lX$ is shown in Fig. 2.1 and consists of a high-energy lepton scattering from a proton via the exchange of a virtual photon, γ^*. It is, of course, also possible for other gauge bosons, such as Z^0s or Ws to be exchanged, but we will not consider them here. The energy of the photon is high enough to reveal the constituent particles inside the hadron, whilst the interaction is sufficiently violent to cause the proton to disintegrate. Deep-inelastic scattering was the original process used at SLAC to reveal the constituent particles within the proton and since those early experiments it has become a powerful test of QCD. It is now indispensible for the measurement of the parton distributions within the proton as well as a means of determining the strong coupling constant, α_s. The relevant kinematic variables for the scattering are

$$q = k - k' , \qquad \nu = \frac{P.q}{M} \qquad \text{and} \qquad W^2 = (P+q)^2 \tag{2.1}$$

where M is the proton's mass and the four momenta are those shown in Fig. 2.1. In the lab. frame the four momenta are given by

$$P_\mu = (M,0,0,0) \qquad k_\mu = (E,k) \qquad k'_\mu = (E',k') \tag{2.2}$$

and so ν corresponds to

$$\nu = E - E' \tag{2.3}$$

namely, the energy lost by the lepton. The virtual photon is timelike ($q^2 < 0$) and so it is convenient to introduce the positive variable

$$Q^2 = -q^2 > 0 . \tag{2.4}$$

In terms of the scattering angle, θ, of the lepton and its initial and final energies, Q^2 is given by

$$Q^2 = 4EE'\sin^2(\theta/2) \tag{2.5}$$

and the scattering can thus be completely described in terms of the two independent variables ν and Q^2.

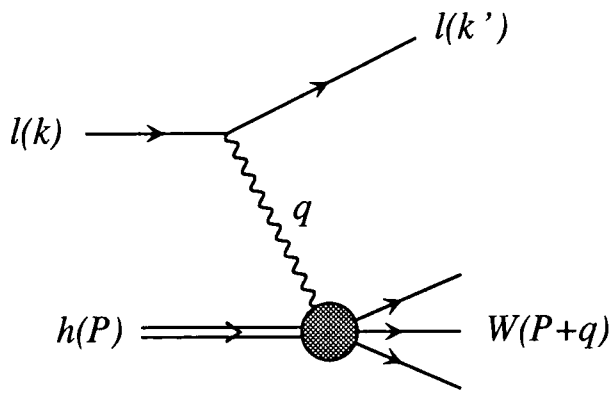

Figure 2.1. The deep-inelastic scattering process in which a virtual photon, γ^*, probes a proton.

The cross section for the process, summed and averaged over spins, can be written as the product of a leptonic tensor, $L_{\mu\nu}$, and a hadronic tensor $W_{\mu\nu}$.

$$\frac{\mathrm{d}^2\sigma}{\mathrm{d}\Omega \mathrm{d}E'} \sim L_{\mu\nu}W^{\mu\nu} \tag{2.6}$$

Where Ω is the solid angle. The leptonic tensor contains only the scattering information relevant to the upper part of the process shown in Fig. 2.1. Consequently it is independent of the nature of the lower (hadronic) vertex and can be calculated from electroweak theory. Our ignorance of the whole process is, instead, contained entirely within the hadronic tensor which describes the lower part of the Feynman diagram. Although this tensor is non-perturbative (and thus at present unknown), it is possible to use symmetry and current conservation arguments to constrain its form [5]. The most general tensor which satisifies these conditions is

$$W^{\mu\nu} = W_1\left(-g^{\mu\nu} + \frac{q^\mu q^\nu}{q^2}\right) + W_2\frac{1}{M^2}\left(P^\mu - \frac{P.q}{q^2}q^\mu\right)\left(P^\nu - \frac{P.q}{q^2}q^\nu\right) \qquad (2.7)$$

where the W_i's are functions of the Lorentz scalar variables that can be constructed from the four momenta at the hadronic vertex. It is straightforward to show that the cross section can be written as

$$\frac{\mathrm{d}^2\sigma}{\mathrm{d}\Omega\mathrm{d}E'} = \frac{\alpha^2}{4E^2\sin^4\theta/2}\left[W_2(\nu,q^2)\cos^2(\theta/2) + 2W_1(\nu,q^2)\sin^2(\theta/2)\right] . \qquad (2.8)$$

In order to proceed further, however, it is necessary to make some assumptions about the interaction between the virtual photon and the proton. Originally this problem was solved using the parton model and then, more formally, with QCD.

Before we discuss these theories, however, it is useful to introduce the dimensionless variables

$$x = \frac{Q^2}{2P.q} \qquad \text{and} \qquad y = \frac{P.q}{P.k} \qquad (2.9)$$

where the four momenta are shown in Fig. 2.1. The ranges of x and y are given by

$$0 \leq x \leq 1 \qquad \text{and} \qquad 0 \leq y \leq 1 \qquad (2.10)$$

The first of these variables is known as Bjørken x and, as we shall see, it plays a very important rôle in the parton model of deep-inelastic scattering.

2.2 The parton model

In the parton model the interaction at the hadron vertex is assumed to be an elastic scattering from a single point-like constituent inside the proton (Fig. 2.2). The process can thus be calculated in terms of the photon-parton interaction and the total cross section will be dependent on the probability for the photon to find such a parton inside the proton.

Parton model calculations must be made in a frame in which the proton has a very large (effectively infinite) momentum and all of its partons are travelling in the same direction. In this frame the timescale for the photon-parton interaction is much shorter than that for the parton-parton interactions which, consequently, can be ignored. The final results of the calculation can be Lorentz transformed back into the lab. frame in which they are required.

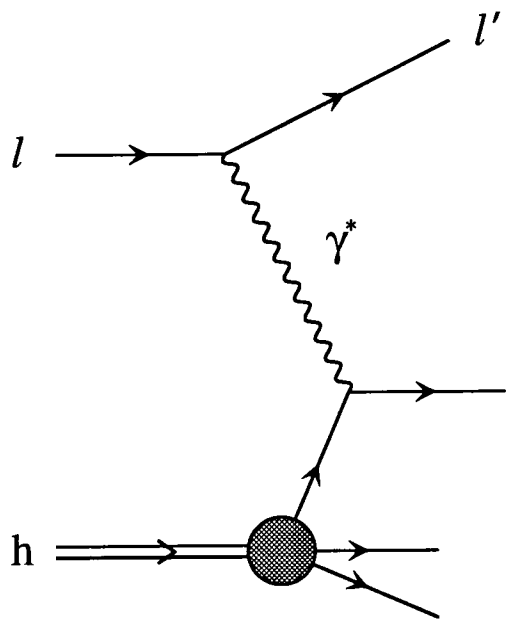

Figure 2.2. The parton model picture of deep-inelastic scattering. The virtual photon, γ^*, interacts with a point-like constituent of the proton, a parton.

When the momenta of the partons transverse to the proton's momentum are neglected, it is possible to assume that each parton carries a fraction ξ of the original proton's momentum, that is

$$p_\mu \;=\; \xi P_\mu \tag{2.11}$$

Since the parton which takes part in the interaction remains close to its mass shell, both before and after the scattering, we find that

$$(\xi P + q)^2 \;\simeq\; 2\xi P.q + q^2 \;\simeq\; 0 \tag{2.12}$$

where the particle masses have been neglected, and consequently

$$\xi \;=\; \frac{Q^2}{2P.q} \;=\; x\,. \tag{2.13}$$

That is to say, in the parton model, the Bjørken scaling variable x can be identified as the fraction of the proton's momentum carried by the struck parton. The probability for a parton to carry such a fraction is, however, not predicted by the parton model. These probabilites are described by the parton distributions, $f_{i/h}(x)$, where $f_{i/h}(x)\mathrm{d}x$ represents the number of partons of type i carrying a fraction between x and $x + \mathrm{d}x$ of the total hadronic momentum. The various parton distributions are required to satisfy certain sum rules which reflect the conservation of physical quantities. Firstly, the total number of quarks of each type i, present within a hadron, should agree with the number predicted by the original quark model of Gell-Mann and Zweig. Before this number can be calculated, it is necessary to take account of the excess numbers of quarks generated by the creation of quark-antiquark pairs. If we define the valence quark distributions to be

$$u_v \;=\; u(x,Q^2) - \bar{u}(x,Q^2) \tag{2.14}$$

and

$$d_v \;=\; d(x,Q^2) - \bar{d}(x,Q^2) \tag{2.15}$$

then the number of up valence quarks inside the proton is then given by

$$\int_0^1 \mathrm{d}x\, u_v \;=\; 2 \tag{2.16}$$

and similary for down quarks we have

$$\int_0^1 \mathrm{d}x\, d_v \;=\; 1\,. \tag{2.17}$$

A further constraint on the form of the parton distributions comes from the conservation of momentum. The total of all the various partons' momenta must add up to that of the proton and consequently we require

$$\sum_i \int_0^1 (xP) f_{i/h}(x)\mathrm{d}x \;=\; P \tag{2.18}$$

and so

$$\sum_i \int_0^1 (x) f_{i/h}(x)\mathrm{d}x \;=\; 1\,. \tag{2.19}$$

Once the probability of finding a parton within the proton is defined, it is possible to compute the previously unknown functions, $W_1(\nu, Q^2)$ and $W_2(\nu, Q^2)$. The resulting expressions are found to be [5]

$$\nu W_2(\nu, Q^2) \to F_2(x) \;=\; \sum_i e_i^2 x f_i(x)$$

and

$$M W_1(\nu, Q^2) \to F_1(x) \;=\; \frac{1}{2x} F_2(x)\,. \tag{2.20}$$

Notice that the functions $F_1(x)$ and $F_2(x)$ depend only on x and not Q^2. They are said to demonstrate Bjørken scaling. Consequently, the differential cross section which contains these structure functions

$$Q^4 \frac{\mathrm{d}\sigma}{\mathrm{d}x\mathrm{d}y} \;=\; 4\pi\alpha^2 s \left[(1-y)F_2(x) + \frac{1}{2} y^2 2x F_1(x)\right] \tag{2.21}$$

also scales. This behaviour was observed by the original SLAC experiments, however, later experiments were to reveal that, in reality, the cross sections deviate from the predictions of scaling. In order to understand how this comes about, it is necessary to modify the parton model to include the processes predicted by perturbative QCD.

2.3 QCD corrections to the parton model

The inclusion of QCD interactions into the parton model immediately leads to the prediction that Bjørken scaling is violated. Indeed, this prediction was one of the first successes of perturbative QCD. The relevant $O(\alpha_s)$ QCD corrections to deep-inelastic scattering are shown in Fig. 2.3.

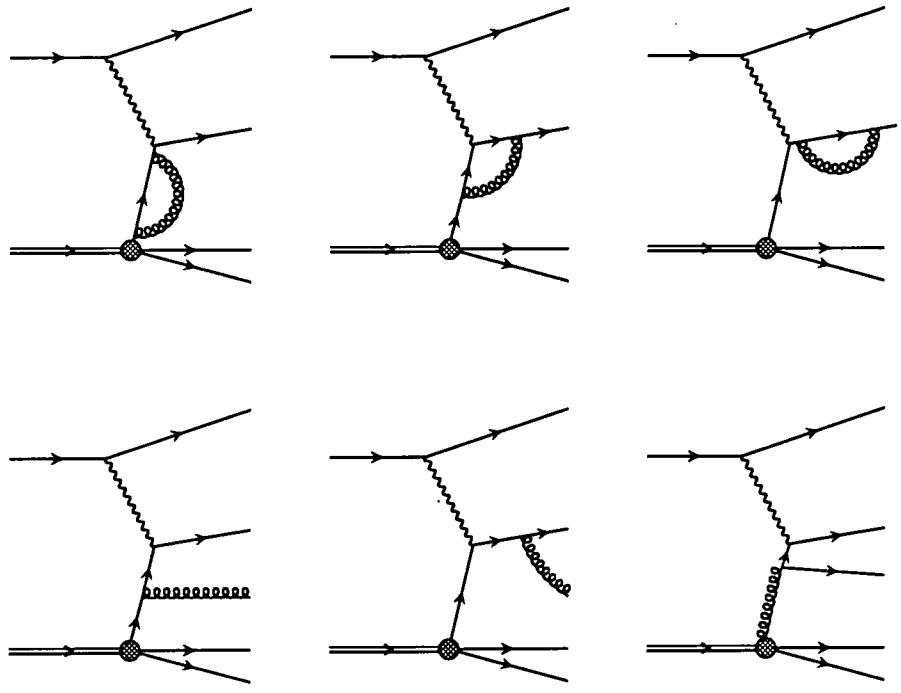

Figure 2.3. $O(\alpha_s)$ corrections to deep-inelastic scattering.

As before, the interactions between separate partons can be neglected, since, in the appropriate frame, they occur on timescales much longer than that of the photon-parton interaction. In addition, however, there also exist processes of the type shown in Fig. 2.4

which are known as *higher twist* contributions. In principle, higher twist diagrams are very dangerous as they prevent the factorization of the cross section into the relevant hard and soft parts. Fortunately, however, it can be shown [6] that these processes are suppressed by $O(1/Q^2)$ and thus, at large Q^2, can be neglected.

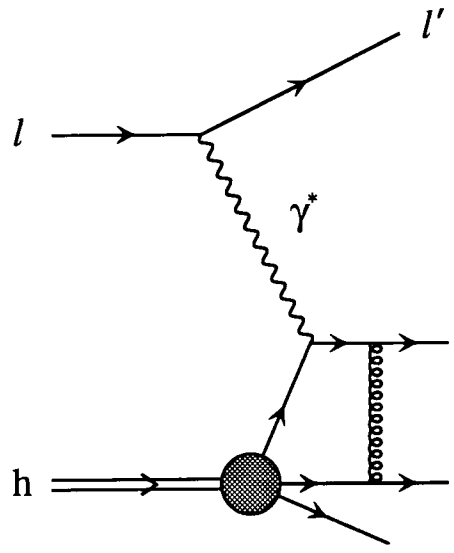

Figure 2.4. An illustration of a *higher twist* effect. The contributions from such processes are suppressed by a factor $1/Q^2$ and thus can be ignored at large Q^2.

In QCD each parton can be imagined as being surrounded by a cloud of virtual particles which are continually being created and annihilated. As the Q^2 of the virtual photon grows its ability to probe down to shorter distances increases and it will eventually begin to resolve the particles contained within this cloud. As a result, the momentum distribution of the partons, as measured by the probing photon, will depend on Q^2 and it is this dependence which leads to the violation of Bjørken scaling. Not only does QCD predict the generation of a Q^2 behaviour for the parton distributions, but it also tells us

the form of this dependence. In order to gain some understanding of how this comes about it is instructive to examine one of the processes which involves the emission of a parton.

Consider, for example, the process shown in Fig. 2.5 in which a quark radiates a gluon. Here the quark, which initially has a momentum p, emits a gluon and consequently reduces its momentum to zp where z is some fraction, $0 < z < 1$. The remainder of the momentum, $(1-z)p$, is carried away by the radiated gluon.

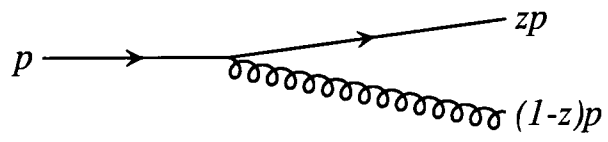

Figure 2.5. A quark carrying a momentum, p radiates a gluon thereby reducing its momentum to zp. The remaining momentum $(1-z)p$ is carried away by the gluon.

It is possible to calculate this process in perturbation theory and thus obtain the probability for its occurrence. The result is found to depend on the function

$$\frac{\alpha_s(Q^2)}{2\pi} \mathrm{P}_{qq}(z) \log(Q^2/\mu^2) \tag{2.22}$$

where $\mathrm{P}_{qq}(z)$ is known as a *splitting function* and is given by

$$\mathrm{P}_{qq} = \frac{4}{3}\left(\frac{1+z^2}{1-z}\right) \tag{2.23}.$$

The $\log(Q^2/\mu^2)$ term in Eq. (2.22) originates from the integration over the transverse momentum of the quark propagator, where μ^2 is some lower cut-off. Equation 2.22 thus has two potential sources of singularities. The first occurs when $z = 1$ and is due to

soft (low energy) gluon emission. This singularity is cancelled by the inclusion of virtual corrections into the $q \to qg$ process and leads to a modified splitting function of the form

$$\mathrm{P}_{qq} = \frac{4}{3}\left(\frac{1+z^2}{1-z}\right)_+ = \frac{4}{3}\left[\frac{1+z^2}{(1-z)_+} + \tfrac{3}{2}\delta(1-z)\right] \tag{2.24}$$

where the '+'-prescripton is defined by

$$\int_x^1 \mathrm{d}z \frac{f(z)}{(1-z)_+} = f(1)\ln(1-x) + \int_x^1 \mathrm{d}z\, \frac{f(z)-f(1)}{(1-z)}\,. \tag{2.25}$$

The second cause for concern comes from the divergencies which originate from the emission of gluons collinear to the original quark. This corresponds to the limit μ tends to zero and is only true for massless particles. Although this pole can be regularized with a finite quark mass (or some other suitable scale, μ^2) the resulting logarithms of $\log(Q^2/\mu^2)$, are large and ruin the perturbative expansion of the process. The answer here is to absorb these logarithms into a redefinition of the physically observable parton distributions, $f_{i/h}(x, Q^2)$. This procedure can be consistently carried out order by order in perturbation theory [7] and restores a small expansion parameter to the perturbation series. As well as absorbing all of the collinear divergencies, it is also possible to absorb (arbitrarily) parts of the higher-order expressions for the hard scattering process. In order to remove the ambiguities that this can create, it is necessary to specify a *factorisation scheme.* Each scheme thus specifies exactly which terms are absorbed into the definitions of the parton distributions.

The effects of each of the possible parton splittings such as Eq. (2.24) determines how the parton distributions change (or *evolve*) with Q^2. The expressions which describe this evolution are the *Altarelli-Parisi* equations (or, more correctly, the Dokshitzer-Gribov-Lipatov-Altarelli-Parisi equations) [8]. At leading-order in QCD they are given by

$$\frac{\mathrm{d}q(x,Q^2)}{\mathrm{d}\log Q^2} = \frac{\alpha_s(Q^2)}{2\pi}\int_x^1 \frac{\mathrm{d}y}{y}\left[\mathrm{P}_{qq}\left(\tfrac{x}{y}\right)q(y,Q^2) + \mathrm{P}_{qg}\left(\tfrac{x}{y}\right)g(y,Q^2)\right] \tag{2.26}$$

and

$$\frac{\mathrm{d}g(x,Q^2)}{\mathrm{d}\log Q^2} = \frac{\alpha_s(Q^2)}{2\pi}\int_x^1 \frac{\mathrm{d}y}{y}\left[\sum_q \mathrm{P}_{qg}\left(\tfrac{x}{y}\right)q(y,Q^2) + \mathrm{P}_{gg}\left(\tfrac{x}{y}\right)g(y,Q^2)\right] \qquad (2.27)$$

Although the Altarelli-Parisi equations are not capable of determining the parton distributions outright, they are nevertheless very important. They predict exactly how the parton distributions will change with variations in the scale, Q^2. With these equations it is therefore possible to determine the parton distributions at any value of Q^2, provided we know their form at some other scale, Q_0^2. Of course, obtaining such a set of parton distributions is not easy. Until suitable progress is made in non-perturbative calculations we have little choice but to obtain these distributions from the analysis of experimental data.

2.4 Extracting parton distributions from experimental data

Before any steps are taken to determine a set of parton distributions it is necessary to choose a factorization scheme. As was mentioned earlier, the choice of scheme removes the ambiguities present beyond leading order in both the definitions of the parton distributions and in the expressions for the hard-scattering subprocesses. Once a scheme has been chosen it is possible to proceed. The first step is to choose a scale Q_0^2 at which to introduce an initial estimate for the various parton distributions present in the hadron. This choice of scale should be such that $Q_0^2 \gg \Lambda^2$ in order to ensure that perturbation theory is valid. However, it should also be chosen low enough to avoid the need to evolve towards smaller values of Q^2. The reason lies in the nature of the Altarelli-Parisi equations which are much more stable to evolution upwards towards larger values of Q^2, than downwards to lower values. Due to this consideration typical choices of the initial scale, Q_0^2, are usually around 4 GeV^2.

The initial estimates for the parton distributions take the form of parametrizations in x and of course it is technically possible to choose any parametrization that one likes. However, there are both physical and pragmatical reasons for choosing parametrizations which possess certain properties. The more thought one gives to this initial choice, the less work is necessary at later (and more time consuming) stages of the analysis. One possible choice of parametrization is

$$f_i(x, Q_0^2) \;=\; A_i x^{\delta_i}(1-x)^{\eta_i} \tag{2.28}$$

where the A_i, δ_i and η_i's are (initially) free parameters determining the distributions of the gluon and each flavour of valence and sea quark. The theoretical motivation for the form of (2.28) is discussed below. Even this "simple" choice appears, at first sight, to introduce a large number of free parameters to be determined. If we consider the situation for the proton, for example, then we see that there seems to be at least twenty of them. Fortunately, the situation is not as bad as it appears because some of them are constrained. Firstly, the sum rules of Eqs. (2.14) and (2.15) determine the normalization parameters, A_u and A_d, of the up and down valence quark distributions respectively. For example, for the case of the up-valence quark the sum rule

$$\int_0^1 \mathrm{d}x\; A_u x^{\delta}(1-x)^{\eta} \;=\; 2 \tag{2.29}$$

implies that

$$A_u \;=\; 2\frac{\Gamma(\delta+\eta+2)}{\Gamma(\delta+1)\Gamma(\eta+1)}\,, \tag{2.30))}$$

and a similar argument can be applied to the down quark normalization. There is one further sum rule that can be used to constrain the number of free parameters. This is the momentum conservation sum rule of Eq. (2.19) and it enables us to determine one further normalization parameter. Traditionally this is taken to be the gluon parameter, A_g. Finally, it is also possible to reduce the number of free parameters present in the sea quark distributions. In this case the number of such quarks is not well defined and

consequently, it is not possible to constrain their normalizations parameters via a sum rule. However, it is possible to relate the distributions of each flavour of anti-quark, using the experimental observation [9] that

$$\bar{u}(x,Q^2) \simeq \bar{d}(x,Q^2) \simeq 2\bar{s}(x,Q^2) \,. \tag{2.31}$$

for low values of Q^2. With the approximation that this relationship is true at our initial scale, Q_0^2, it is then only necessary to parameterize the total quark sea defined by

$$S(x,Q_0^2) \;=\; 2[\bar{u}+\bar{d}+\bar{s}] \,. \tag{2.32}$$

Also, if we have chosen Q_0^2 to be low enough, then the heavy quark distributions will be negligible and we can set

$$c(x,Q_0^2) \;=\; \bar{c}(x,Q_0^2) \;=\; 0 \tag{2.33}$$

together with both the top and bottom quark distributions. Instead, the heavy quark content of the hadron can be generated during the evolution to higher Q^2. The effect of all of these constraints is to reduce the number of free parameters down to an acceptable number. For the example case that we have chosen there would be only nine free parameters (not including $\Lambda_{\rm QCD}$) necessary to determine the parton distributions of the proton. For a simpler hadron, such as the pion, there would be only seven.

Once we have a set of suitably parametrized parton distributions, we need to choose some inital values for the parameters. These will eventually change as we compare the predictions with the data, but, as before, the better our inital choice is, the less work (or rather the less computer time) we will need to spend later on. Furthermore, if a parameter is not well determined by the data, then we may need to fix it at some (theoretically motivated) value.

Fortunately, there are methods which can suggest the approximate limiting behaviour for the parton distributions at both $x \to 1$ and $x \to 0$. The $x \to 1$ behaviour of the parton

distributions can be predicted by counting the number of "spectator" quarks present in the hadron. These spectator quarks do not participate in the interaction (hence their name) but still carry some fraction of the hadron's momentum. the more of these quarks that are present, the less likely it will be that a parton will be found carrying almost all of the hadron's momentum and there exist appropriate counting rules [10] to reflect this. These rules predict that as $x \to 1$ the parton distributions should behave as

$$f_i(x) \sim (1-x)^{2n_s-1} \tag{2.34}$$

where n_s is the number of spectator quarks present in the hadron. So, for example, at large x, the gluon distribution should behave approximately as

$$g(x) \sim (1-x)^5 \tag{2.35}$$

for the proton, where there are three spectator quarks, whilst

$$g(x) \sim (1-x)^3 \tag{2.36}$$

for the pion, with two spectators. Meanwhile, the predictions for the small x behaviour are provided by Regge theory (see Chapter 5). This predicts that the low x behaviour of each parton distribution is determined by the nature of a particular "Regge trajectory" and leads to a behaviour as $x \to 0$ of the form

$$f_i(x) \sim x^{-\delta} \tag{2.37}$$

with $\delta \simeq 1$ for the gluon and sea quarks and $\delta \simeq 1/2$ for the valence quarks. Together, these theories not only suggest possible values for the initial parameters η_i and δ_i, but also provide the original motivation behind the choice of parametrization that we adopted in Eq. (2.28).

The above procedure allows for the generation of an initial set of parton distributions at the scale Q_0^2. It is now possible to utilize the Altarelli-Parisi equations to determine the

parton distributions at any Q^2. Together with the appropriate expressions for the hard scattering processes, it is thus possible to generate predictions which can be compared with experiment. This comparison will determine the "quality" of the choice of parameters and so, by iterating the procedure, it is possible to determine the parameters which give the best agreement with the data. Of course, in practice the process of parameter fitting can be rather complicated. Care must be taken to avoid the problems caused by the discrepancies between different data sets, as well as those arising from correlated parameters, local minima and systematic errors (to mention but a few). However, once the process is complete the property of universality ensures that the final parton distributions can be used to predict a wide range of different experimental processes. This alone makes the task worthwhile.

3 Drell-Yan and prompt photon processes

3.1 Introduction

There are several processes in addition to deep-inelastic scattering which we need to study in order to extract an accurate set of parton distributions. Two important ones are the Drell-Yan process [11] and prompt photon production [12]. They are especially important processes for determining the pion parton distributions as there have been no deep-inelastic scattering experiments which have used pion targets. In the case of the Drell-Yan process the dominant mechanism proceeds via quark-antiquark annihilation $q\bar{q} \rightarrow \gamma^*$. As a result, it can provide the information necessary to determine the pion's valence quark distribution. This is in contrast to the situation for proton-proton collisions where the Drell-Yan process is valuable because it probes the sea quark distribution through $q_v \bar{q}_{\rm sea} \rightarrow \gamma^*$. Lastly we are going to look at prompt photon (sometimes called direct photon) production. This is important because it directly probes the gluon distribution. For both deep-inelastic scattering and Drell-Yan the gluon enters only as a small effect at next-to-leading order, whereas for prompt photon production the gluon enters at leading order via $gq \rightarrow \gamma q$. In this chapter we shall study both processes in turn.

3.2 The Drell-Yan process

3.2.1 Introduction

The Drell-Yan process corresponds to the production, in hadronic collisions, of a lepton pair with a large invariant mass M^2. The first experimental results were published in 1970 by Christenson *et al.* [13] who were studying massive μ-pair production from high energy protons incident on nuclei. Subsequently, Drell and Yan suggested a 'naïve' model [14] for the interaction in terms of the recently developed parton model. They proposed that the production mechanism consists of the annihilation of a quark and anti-quark into a virtual photon which subsequently "decays" into a lepton pair (Fig. 3.1).

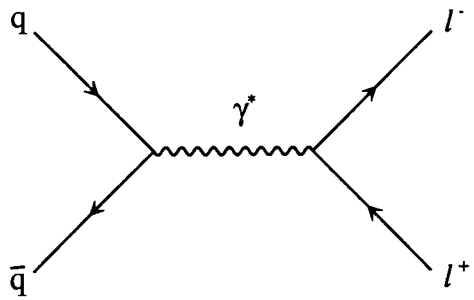

Figure 3.1. The Drell-Yan process at leading order.

Notice that in this process the virtual photon is timelike ($q^2 > 0$) as opposed to the spacelike ($q^2 < 0$) photon of deep-inelastic scattering. The total cross section for the sub-process ($q\bar{q} \rightarrow \gamma^* \rightarrow \mu^+\mu^-$) can be obtained very simply from the QED process $e^+e^- \rightarrow \mu^+\mu^-$. The only differences are due to the presence of a fractional quark charge,

e_q, and an extra factor of $\frac{1}{3}$ necessary to average over the three different quark colours. We therefore have

$$\hat{\sigma}(q\bar{q} \to \gamma^* \to \mu^+\mu^-) \;=\; \frac{1}{3} \cdot \frac{4\pi\alpha^2 e_q^2}{3m^2} \tag{3.1}$$

Here M^2 represents the invariant mass of the muon pair and is given by

$$M^2 = (p_q + p_{\bar{q}})^2 \;\simeq\; 2x_1x_2P_1.P_2 \;=\; x_1x_2s \tag{3.2}$$

The total cross section is, as usual, obtained by convoluting the subprocess with the corresponding parton distributions of the parent hadrons which yields

$$\frac{\mathrm{d}\sigma}{\mathrm{d}M^2} \;=\; \frac{4\pi\alpha^2}{9M^2}\sum_q e_q^2 \int \mathrm{d}x_1 \int \mathrm{d}x_2 \left[f_q(x_1, M^2) f_{\bar{q}}(x_2, M^2) + (q \leftrightarrow \bar{q})\right] \delta(\hat{s} - M^2)\,, \tag{3.3}$$

where we have introduced the variable τ defined by

$$\tau \;=\; x_1x_2 \;=\; \frac{M^2}{s}\,. \tag{3.4}$$

If we now write the expression for the cross section in the form

$$M^4 \frac{d\sigma}{dM^2} \;=\; \mathcal{F}(\tau) \tag{3.5}$$

then we find it is no longer dependent on the invariant mass, M^2, but only on the dimensionless variable τ. This 'scaling' behaviour is analogous to that of deep-inelastic scattering. Of course, it is only strictly true in the context of the naïve parton model, in which the parton distributions do not depend on M^2. Nevertheless, when the data are plotted in the form of (3.5) they clearly demonstrates this scaling behaviour to a good approximation.

The one remaining Drell-Yan variable which we need to introduce is Feynman x

$$x_F \;=\; x_1 - x_2\,. \tag{3.6}$$

This has the advantage of being easily measured by experiment as it can be obtained from the relationship

$$x_F = \frac{2p_L}{\sqrt{s}} \tag{3.7}$$

where p_L is the longitudinal momentum of the muon pair. The range of x_F is given by

$$-1 + \tau \leq x_F \leq 1 - \tau \tag{3.8}$$

corresponding to the cases for which either of the variables x_1 or x_2 is equal to one.

When compared directly with experimental data, the theoretical predictions are found to be consistently smaller by a factor of almost two. This ratio between data and theory is known as the K factor

$$K = \frac{\sigma_{\text{exp}}}{\sigma_{\text{theory}}} \simeq 1.8 \tag{3.9}$$

At first sight such a large discrepancy seems quite alarming. Fortunately, however, when the $O(\alpha_s)$ corrections are included into the theory this ratio becomes consistent with one.

3.2.2 Higher-order corrections

The $O(\alpha_s)$ corrections to the Drell-Yan process fall into two categories. The first consists of the 'annihilation' processes and includes both the virtual gluon graph of Fig. 3.2a and the real gluon emission graphs of Fig. 3.2b and c. The remaining contributions come from the 'Compton' processes shown in Fig. 3.3

The calculations for these corrections were first performed by Altarelli *et al* [15] and Kubar *et al* [16]. The resulting expressions for the differential cross section are rather long, although the interested reader can find the relevant formulae in Appendix A.

One uncertainty, which is always present in theoretical calculations, is the choice of the renormalisation scale for the running coupling, α_s. The renormalisation group equations

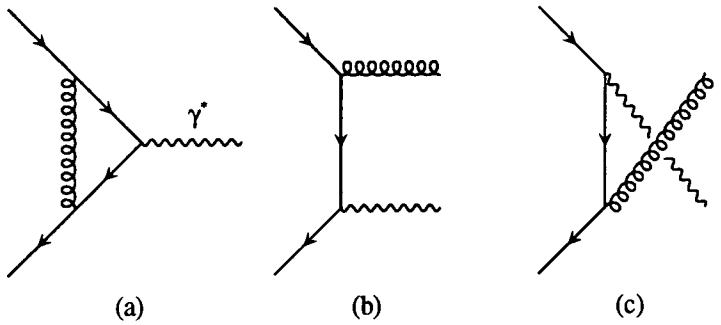

Figure 3.2. Annihilation graph contributions to the $O(\alpha_s)$ corrections to the Drell-Yan process. a) Vertex correction (virtual gluon); (b,c) gluon production.

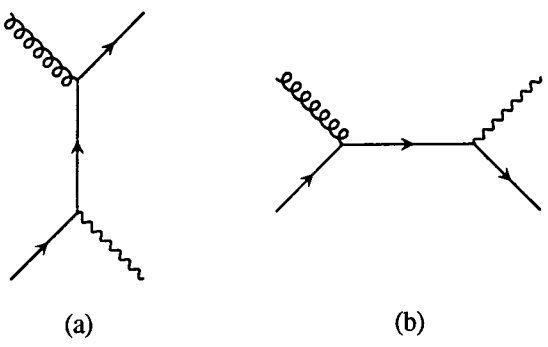

Figure 3.3. Compton graph contributions to the $O(\alpha_s)$ corrections to the Drell-Yan process.

tell us that the all-orders cross section must be independent of this scale choice. However, we can only work at a finite order in perturbation theory, and, as a result, we find that our predictions have an unphysical dependence on the scale, μ. There are various schemes for choosing the 'best' scale. For the Drell-Yan process it is traditional to choose the scale $\mu^2 = M^2$ as this removes logarithms of μ^2/M^2 from the perturbative expansion and so (in principle) should reduce the size of the $O(\alpha_s^2)$ terms and higher. The recent calculations

of the Drell-Yan cross section to second-order [17] should help shed further light on the 'optimum scale' choice.

3.2.3 Drell-Yan experiments

There have been many lepton pair production experiments since 1970. For a review of some of the more recent ones see Freudenreich [18]. At present the experiments which have accumulated the highest statistics are shown in Table 3.1.

Table 3.1 *High statistics Drell-Yan experiments.*

Experiment	Beam	Target
E605 [19]	p	Cu
NA10 [20]	π^-	H_2 and W
E615 [21]	$\pi^\pm$	W

All of these experiments included data taking with intermediate or heavy nuclei targets (such as tungsten). This has the effect of increasing the statistics to an acceptable level. Unfortunately it also introduces systematic errors through the unknown nuclear effects produced inside the target. It is now fairly well accepted that the parton distributions of heavy nuclei are not the same as those inside the proton or neutron [22]. The only way of learning about these effects is to perform experiments on a range of nuclear targets and try and analyse the results. This approach was adopted by the E772 collaboration [23].

3.3 Prompt photon production

The final process that we are going to examine is prompt photon production. Even though the creation of a photon is suppressed by a factor α/α_s when compared with the

equivalent jet production cross section, it does have the advantage that the photon represents a clean jet. It is therefore free from the ambiguities inherent in any jet reconstruction technique. Moreover, modern day experiments have luminosities which are high enough to generate large numbers of events despite the reduction due to the electromagnetic coupling.

The two basic mechanisms responsible for prompt photon production are $q\bar{q} \rightarrow \gamma g$ and $qg \rightarrow \gamma q$ as shown in Figs 3.4a and 3.4b respectively.

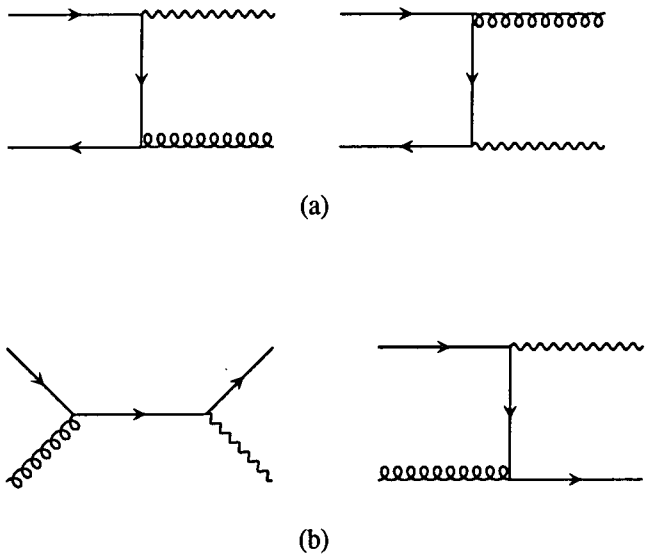

Figure 3.4. Leading order contributions to prompt photon production. (a) the annihilation diagrams. (b) the Compton diagrams.

These diagrams show that, unlike the Drell-Yan and deep-inelastic scattering processes, the gluon enters at leading order. We can therefore expect this process to be an extremely useful mechanism for determining the gluon distribution. The relative importance of the Compton diagrams depends on the nature of both the beam and the target

and also on the kinematical region of the variables. For $p\bar{p}$ and $\pi^- p$ interactions there is the possibility of valence-valence annihilation and so these diagrams tend to dominate. However, at high energies the contribution from the Compton terms increases and eventually overtakes that of the annihilation terms. For the case of $\pi^+ p$ collisions, the reduction in the available number of valence quarks for the annihilation subprocess allows the Compton diagrams to dominate at even lower energies. For pp scattering the absence of valence-valence annihilation means that the Compton terms always dominate.

The differential cross section for prompt photon production at leading order is

$$E_\gamma \frac{\mathrm{d}^3\sigma}{\mathrm{d}^3 p_\gamma} = \sum_{i,j} \int \mathrm{d}x_1 \int \mathrm{d}x_2 \, f_i(x_1, m^2) f_j(x_2, m^2) \, \frac{\hat{s}}{\pi} \frac{\mathrm{d}\hat{\sigma}}{\mathrm{d}t} \, \delta(\hat{s} + \hat{t} + \hat{u}) \tag{3.10}$$

where the sub-process cross section, $\mathrm{d}\hat{\sigma}/\mathrm{d}\hat{t}$, is given by

$$\frac{\mathrm{d}\hat{\sigma}}{\mathrm{d}\hat{t}} = \frac{-e_q^2}{3} \left[\frac{\hat{u}}{\hat{s}} + \frac{\hat{s}}{\hat{u}} \right] \frac{\pi \alpha \alpha_s(\mu^2)}{\hat{s}^2} \qquad \text{(Compton)}$$

and

$$\frac{\mathrm{d}\hat{\sigma}}{\mathrm{d}\hat{t}} = \frac{8e_q^2}{9} \left[\frac{\hat{u}}{\hat{t}} + \frac{\hat{t}}{\hat{u}} \right] \frac{\pi \alpha \alpha_s(\mu^2)}{\hat{s}^2} \qquad \text{(Annihilation)} \tag{3.11}$$

with

$$\hat{s} = x_1 x_2 s, \quad \hat{t} = -x_1 p_T \sqrt{s} e^{-y} \qquad \text{and} \qquad \hat{u} = -x_2 p_T \sqrt{s} e^{y} \tag{3.12}$$

where y is the rapidity of the photon defined by

$$y = \frac{1}{2} \ln \left(\frac{E + p_L}{E - p_L} \right) \tag{3.13}$$

and p_T and p_L are the transverse and longitudinal momenta of the photon respectively.

As with the Drell-Yan process, the leading order prediction and the data are not fully in agreement, although the factor is not as large as in the former case. Once again, the inclusion of higher-order terms brings the theoretical predictions in line with the data.

3.3.1 Higher-order corrections to prompt photon production

The next-to-leading order QCD corrections have been calculated by Aurenche *et al* [24]. The resulting expressions are not available in the literature, the authors felt that they were too lengthy, and so they are only available in FORTRAN. Consequently we do not reproduce them here.

As before, the calculation of the cross section requires a choice of both the factorisation scale, m, and the renormalisation scale μ. One possible choice is $m^2 = \mu^2 = p_T^2$, however, this can cause several problems. Firstly, it seems to prevent any possible agreement between several different prompt photon experiments and, secondly, it indicates a gluon distribution for the proton which is incompatible with deep-inelastic scattering experiments [24]. Consequently, a different choice of scale has been suggested, that determined by the 'principle of minimum sensitivity' [25]. This principle is based on the observation that the physical cross section (and thus the cross section calculated to all-orders, $\sigma^{(\mathrm{all})}$) is independent of the choice of scale and that, as a result

$$\mu \frac{\partial \sigma^{(\mathrm{all})}}{\partial \mu} = 0 \tag{3.14}$$

and

$$m \frac{\partial \sigma^{(\mathrm{all})}}{\partial m} = 0 \tag{3.15}$$

are true for all choices of the scales m and μ. The principle of minimal sensitivity states that we should pick scales such that our truncated expressions (which do depend on μ and m) also satisfy these conditions. That is,

$$\mu \left. \frac{\partial \sigma}{\partial \mu} \right|_{\substack{m_{\mathrm{opt}} \\ \mu_{\mathrm{opt}}}} = 0 \tag{3.16}$$

and

$$m \left. \frac{\partial \sigma}{\partial m} \right|_{\substack{m_{\mathrm{opt}} \\ \mu_{\mathrm{opt}}}} = 0 \tag{3.17}$$

The factorisation scale and the renormalisation scale have thus been chosen to minimize the variation in the cross section under a change of scales. With such a choice it has been shown [24] that the inconsistences mentioned above disappear.

3.3.2 Prompt photon experiments

The first prompt photon experiments with fixed targets began in the early eighties [26]. For a review of some of the recent ones see Aurenche and Whalley [27]. The experiments which have accumulated the highest statistics to date are shown in Table 3.2.

Table 3.2 *High statistics prompt photon experiments.*

Experiment	Beam	Target
WA70 [28]	p, $\pi^{\pm}$	H_2
UA2 [29]	$\bar{p}$	p
E706 [30]	p, $\pi^{\pm}$, $K^{\pm}$	Be and Cu
CDF [31]	$\bar{p}$	p

Unlike the Drell-Yan and deep-inelastic scattering processes these data are mostly taken on light targets and consequently suffer very little from EMC-type [22] effects.

3.4 Summary

Both the Drell-Yan process and prompt photon production are excellent processes for the determination of parton distributions. This is the result of several factors. Firstly, the relevant expressions have been calculated up to next-to-leading order; secondly, there have been several high statistics experiments performed in recent years and, lastly, each process is sensitive to a different type of distribution (quarks for Drell-Yan and gluons for prompt photon production). Each process is thus complementary to the other.

In the following chapter we are going to use both Drell-Yan and prompt photon production data to determine the parton distributions contained within the pion.

4 Parton distributions for the pion extracted from Drell-Yan and prompt photon experiments

4.1 Introduction

The parton distributions of the nucleons are now well determined by global analyses of a whole range of precise data for deep inelastic lepton-nucleon scattering, Drell-Yan and prompt photon production. The most recent analyses [32] include the next-to-leading order (NLO) QCD contributions. However, much less is known about the parton distributions of other hadrons.

There now exists data from several high statistics experiments on pion-nucleon and pion-nucleus collisions. These experiments include both Drell-Yan and prompt photon production. If we assume that the nucleon distributions are precisely known, these data can be used to determine the parton distributions of the pion. In the past, several attempts [33] have been made to extract such information either from subsets of the data or from earlier measurements of the processes. Until now, however, there has been no simultaneous QCD analysis at next-to-leading order of all of the recent high precision pion data. Besides being of interest in their own right and to compare with the nucleon distributions, the parton distributions of the pion are needed for checking the predictions of lattice QCD and will be valuable for estimates of processes at HERA based on the vector meson dominance model of the photon, albeit with the vector meson approximated by a pseudoscalar.

Here we perform a NLO analysis of the Drell-Yan and prompt photon πN data. Since the nucleon distributions are much better determined than those of the pion, it is sufficient to fix on a single set of partons for the proton and to use the πN data to determine only the structure of the pion. We work in the $\overline{\rm MS}$ scheme and we use the HMRS(B) set of parton distributions of the proton [34]. Hence we take the same value of $\Lambda_{\overline{\rm MS}}$ (with four flavours) as obtained by HMRS, namely

$$\Lambda^{(4)}_{\overline{\rm MS}} = 190 \text{ MeV}. \tag{4.1}$$

The quark distributions are defined in the universal $\overline{\rm MS}$ factorization scheme. We use the following parametrization to describe the parton distributions of the pion (π^-) at $Q^2 = Q_0^2 = 4$ GeV^2 :

$$xV_\pi = A_V x^\alpha (1-x)^\beta \tag{4.2}$$

$$xS_\pi \equiv 2x[u + \bar{d} + \bar{s}] = A_s (1-x)^{\eta_s} \tag{4.3}$$

$$xg = A_g (1-x)^{\eta_g} \tag{4.4}$$

where $V_\pi = \bar{u}_V = d_V$ and A_V is determined in terms of α and β by the flavour content of the pion. A_s is taken as a free parameter, so that A_g is determined by η_g and the momentum sum rule. We make the assumption that at $Q^2 = Q_0^2$ the pion sea is SU(3) symmetric. That is we assume

$$u = \bar{d} = \bar{s}. \tag{4.5}$$

Suppressing the strange quark distribution relative to an SU(2) symmetric sea, as, for example, in the proton, would have little effect given the fairly large uncertainty in the sea distribution. The charm distribution of the pion is generated through the evolution equations assuming that the charm quark is massless and that $c(x, Q_0^2) = 0$. There are thus a total of five free parameters to be determined by the data (α, β, A_s, η_s and η_g). We find that the valence quark distributions of the pion are primarily determined by the Drell-Yan data and that the gluon distribution of the pion is mainly constrained by the π^+

prompt photon production process, $\pi^+ p \to \gamma X$; the process $\pi^- p \to \gamma X$ being dominated by $q\bar{q}$ annihilation [35].

4.2 Valence distributions and the Drell-Yan data

The dominant QCD process contributing to Drell-Yan production, $\pi^{\pm} N \to \mu^+ \mu^- X$, is $q\bar{q}$ annihilation, and hence, in principle, these data determine both the valence and the sea quark distributions of the pion. Unfortunately at present there is no available experimental information at sufficiently small x_π ($x_\pi \lesssim 0.2$) to allow an unambiguous determination of the sea quark distribution of the pion. However this ambiguity does not lead to appreciable uncertainties in the determination of the valence (and gluon) distributions from data at larger x_π values.

Recently the calculation of the Drell-Yan cross-section up to order $\alpha_s^2(Q^2)$ [17] has been completed, although the differential form is not available. Here we work consistently at next-to-leading order and we therefore use the expressions of Kubar *et al* [16] suitably modified to the $\overline{\rm MS}$ regularization scheme (as given in Appendix A). In order to compare theory with experiment we calculate the double differential cross-section

$$\frac{{\rm d}^2\sigma}{{\rm d}x_{\rm F}{\rm d}\sqrt{\tau}}$$

where

$$x_{\rm F} = x_\pi - x_N \qquad \text{and} \qquad \tau = x_\pi x_N = \frac{M^2}{s}, \tag{4.6}$$

x_π and x_N are, at leading order, the Bjørken x variables of the pion and target nucleon respectively, M is the invariant mass of the muon pair and $\sqrt{s}$ is the centre of mass energy.

In calculating the cross-sections we use the full next-to-leading order expressions (with no exponentiated terms) and the 'natural' choice of scale $Q^2 = M^2$. We multiply our

theoretical cross-sections by an extra free parameter K' to allow for higher order QCD contributions to the cross-section as well as uncertainties in the overall experimental normalization. It should be noted that there exists some correlation between this factor and the parameters α and β. Fortunately our fits seem to indicate values of K', α and β that appear very reasonable.

We analyse two independent sets of high statistics Drell-Yan data obtained from a π^- beam incident on a tungsten target, $\pi^- W \to \mu^+\mu^- X$, by the NA10 and E615 collaborations respectively. To extract the pion distributions from these data it is necessary to allow for the presence of nuclear effects. As mentioned earlier, we use the HMRS(B) distributions for the proton. This means that we need to correct for the fact that the Drell-Yan data were taken on a heavy nuclear target. We do this by multiplying the parametrized cross-section by a smooth function

$$R = \frac{\mathrm{d}\sigma(\pi W \to \mu^+\mu^- X)}{\mathrm{d}\sigma(\pi D \to \mu^+\mu^- X)}, \tag{4.7}$$

corrected for isoscalarity effects. It is expected from QCD factorization that R will depend only on the target x_N, and not x_π. This is consistent with the experimental measurements of R. The observed values of R [36] are shown in Fig. 4.1 as a function of x_N, and are well described by the straight line

$$R = -0.55 x_N + 1.1. \tag{4.8}$$

We use this form in the results presented here, although we estimate the uncertainty due to nuclear effects by correcting the predictions with other forms for R, including $R = 1$.

The CERN NA10 experiment [20, 18] has accumulated the highest statistics Drell-Yan data (155,000 events). This experiment measured the differential cross-section at two separate beam energies, 194 GeV/c and 286 GeV/c, for a π^- beam on a tungsten target. We choose to perform a fit to the combined data of both energies in a mass range $4.16 < M < 8.34$ GeV/c^2. This region, between the J/ψ and the Υ resonances,

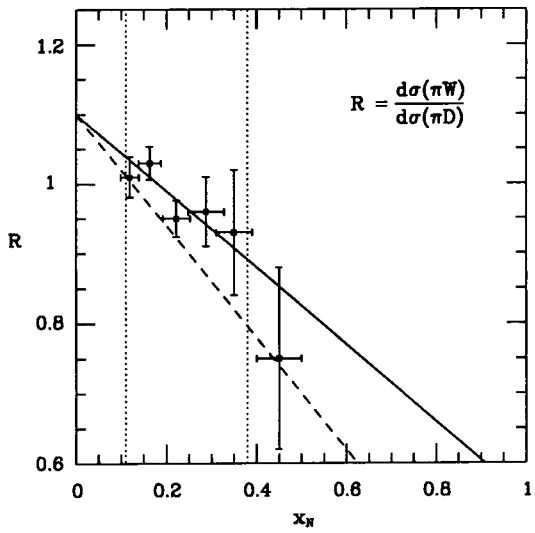

Figure 4.1. The ratio $d\sigma(\pi^- W \to \mu^+\mu^- + X)/d\sigma(\pi^- D \to \mu^+\mu^- + X)$ as a function of x_N. The data points are from Ref. [36]. The solid straight line is $R = -0.55x_N + 1.1$, the dashed one is $R = -0.8x_N + 1.1$. The vertical dotted lines indicate the range of x_N values spanned by the NA10 data included in our fit.

is where the relative errors are smallest and also where NLO QCD is most in agreement with the NA10 data. At higher values of $\sqrt{\tau}$ there is some deviation of the data from the predictions of our QCD analysis. The reasons for this are not clear. We avoid these problems by cutting out this high $\sqrt{\tau}$ region. In addition to this restriction we reject the lowest bin at both energies because of possible background contamination [20]. The regions we are fitting are thus: $0.24 < \sqrt{\tau} < 0.42$ at 194 GeV/c and $0.21 < \sqrt{\tau} < 0.36$ at 286 GeV/c. We also discount data points with $x_F < 0$ because of possible reinteraction effects.

To begin we compare the partons determined from several different fits to these data in which η_g is kept fixed at $\eta_g = 2.1$. The Drell-Yan cross-section is not very sensitive to this parameter and, as we shall see in the next section, η_g is well determined by the prompt photon data; $\eta_g = 2.1 \pm 0.4$. We first vary the parameters α, β, K'_{194} and K'_{286} to

achieve an optimum fit to the CERN NA10 Drell-Yan data. Set 1 of Table 4.1 is obtained by fitting only to the Drell-Yan data with $x_\pi > 0.35$ where the pion sea is irrelevant.

Table 4.1 *The values of the parton parameters of the pion obtained by fitting to the NA10 data of Ref.* [20] *for various choices of the sea quark distribution. Set 1 shows the effect of fitting only to data points for which* $x_\pi > 0.35$. *Fits 2 to 5 show the effect of steadily increasing the sea from one which carries 5% of the pion's momentum at* $Q^2 = Q_0^2$, *to one which carries 20%. The parameters in brackets are held fixed during each fit.*

fit	α	β	A_s	η_s	η_g	K'_{194}	K'_{286}	χ^2/# data
1	0.65	1.07	(-)	(-)	(2.1)	1.30	1.38	48/52
2	0.59	1.08	(0.3)	(5.0)	(2.1)	1.39	1.48	157/62
3	0.61	1.08	(0.6)	(5.0)	(2.1)	1.39	1.48	58/62
4	0.64	1.08	(0.9)	(5.0)	(2.1)	1.33	1.41	54/62
5	0.61	1.02	(1.2)	(5.0)	(2.1)	1.34	1.41	52/62

The remainder of the fits in Table 4.1 include the Drell-Yan data down to $x_\pi \simeq 0.2$ where the pion sea cannot be neglected. Rather than assume a form for the sea quarks we perform a range of fits in which the sea carries an increasing fraction of the pion's momentum. Figure 4.2 shows the various sea distributions that we consider and in a later plot (Fig. 4.10) we will show the effect of their contribution to the overall quark distribution. It can be seen from Table 4.1 that the value of β is hardly affected until the sea distribution becomes quite large ($\langle xS_\pi \rangle \sim 0.2$). The value of α is, as should be expected, more sensitive, but for those sea distributions for which a good description is obtained (fits 3,4,5) the value of α changes only by 0.03 and, moreover, is comparable with the value obtained in fit 1. The valence parameters shown in Table 4.1 can be seen to be in good agreement with those of Ref. [18].

Sets 6 and 7 (Table 4.2) show the effect of varying the nuclear function R. Fit 6 is a repeat of fit 4 but with no correction applied for the effect of the heavy nucleus, that is with R of (7) replaced by $R = 1$. Fit 7 shows the effect of an extreme nuclear correction,

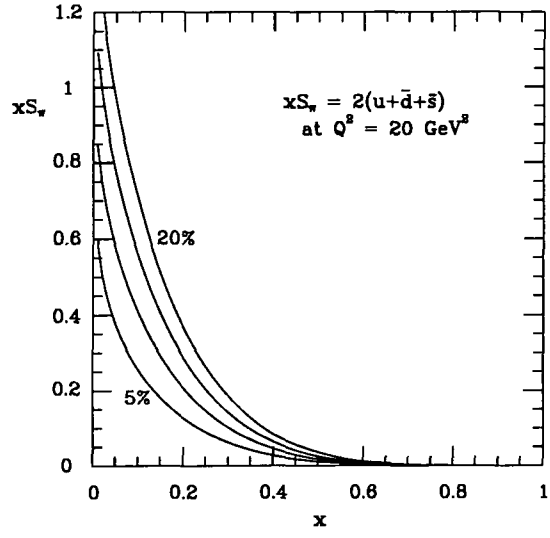

Figure 4.2. The range of sea distributions, $xS_\pi = 2x(u + \bar{d} + \bar{s})$, at $Q^2 = 20$ GeV^2 that we include in our fits to the NA10 and E615 Drell-Yan data. The distributions carry 5%, 10%, 15% and 20% of the pion's momentum at $Q^2 = Q_0^2 = 4$ GeV^2.

described by $R = -0.8x_N + 1.1$ and shown by the dashed line of Fig. 4.1. These two fits show the sensitivity of the parameters to nuclear effects, although, as can be seen from Fig. 4.1, they more than span the range of "nuclear" uncertainty.

For comparison, we next analyse the data of the Fermilab E615 experiment [21] (36000 events). These data are also obtained from a π^- beam on a tungsten target and so we can use the same function R as we used in the fits 1 to 5. The E615 data that we study are in the mass range $4.03 < M < 8.53$ GeV/c^2 for a beam energy of 252 GeV. This corresponds to the range $0.185 < \sqrt{\tau} < 0.392$. Sets 8-12 of partons listed in Table 4.3 are obtained by fitting to these data (and can be compared with sets 1-5 of Table 4.1 obtained from the NA10 data). We find that the E615 data for the two highest $\sqrt{\tau}$ bins in this analysis lie consistently above the best fit curve and so we have repeated the fits omitting these two bins, that is to say we fit the range $0.185 < \sqrt{\tau} < 0.346$. The results are listed in Table 4.2.

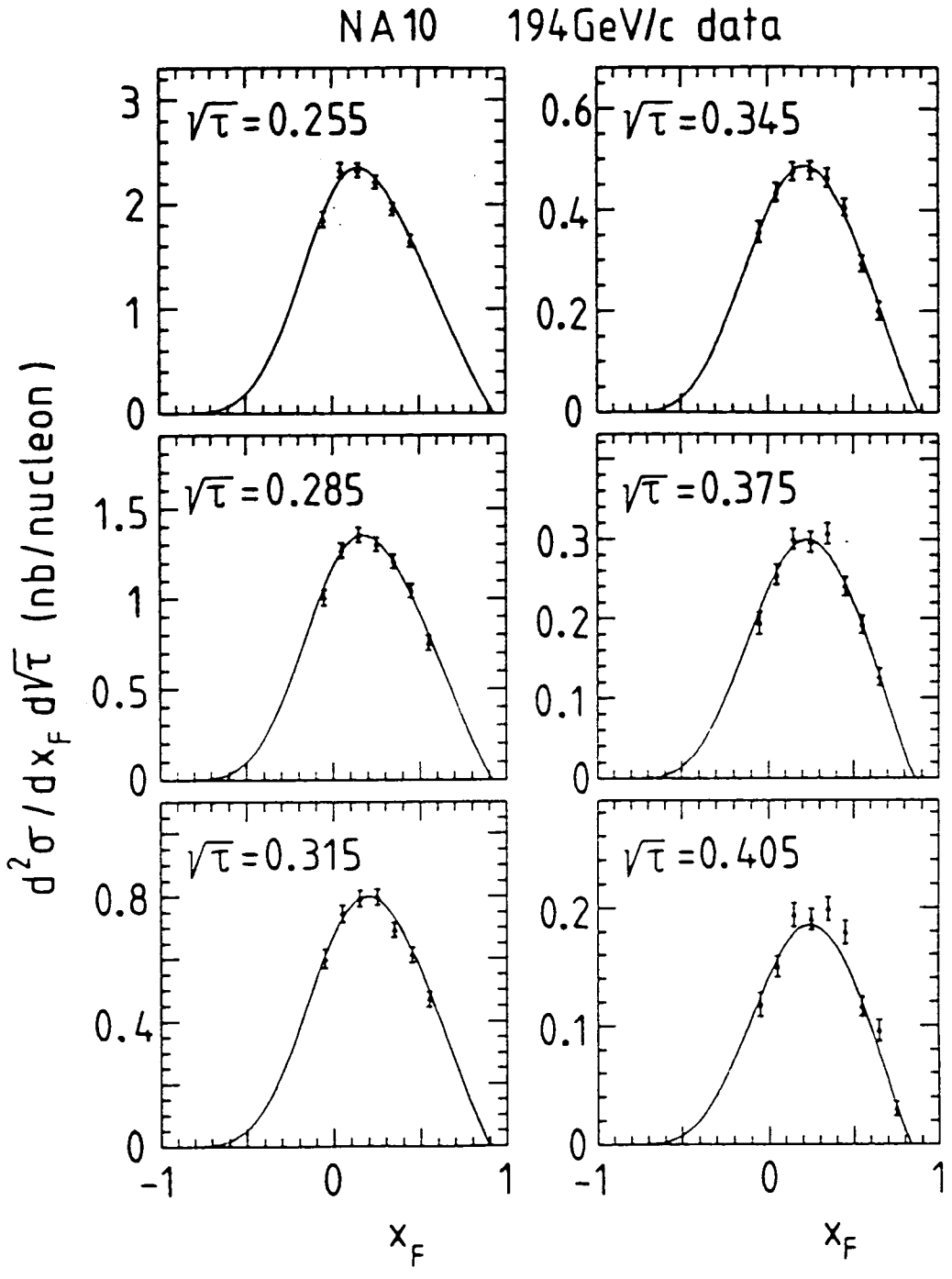

Figure 4.3. Drell-Yan data from the NA10 collaboration [20] for 194 GeV/c π^- on W, together with their description in terms of the NA10 parton distributions of Table 4.7. The points with $x_F < 0$ are not included in the fit.

Table 4.2 *Parameters obtained in fits to the NA10 data using two extreme choices for the function R. Set 6 shows the effect of omitting nuclear effects, $R = 1$, whereas set 7 is obtained from assuming a very pronounced nuclear effect, $R = -0.8x_N + 1.1$. The parameters in brackets are held fixed during each fit.*

fit	α	β	A_s	η_s	η_g	K'_{194}	K'_{286}	χ^2/# data
6	0.65	1.05	(0.9)	(5.0)	(2.1)	1.29	1.38	58/62
7	0.62	1.06	(0.9)	(5.0)	(2.1)	1.44	1.51	82/62

Table 4.3 *Parameters obtained by fitting to the E615 data of Ref.* [21] *(inclusive of the two high $\sqrt{\tau}$ bins) using various input sea quark distributions. Set 8 shows the effect of fitting only to data points for which $x_\pi > 0.35$. Fits 9 to 12 show the effect of steadily increasing the sea from one which carries 5% of the pion's momentum at $Q^2 = Q_0^2$, to one which carries 20%. The parameters in brackets are held fixed during each fit.*

fit	α	β	A_s	η_s	η_g	K'_{252}	χ^2/# data
8	0.59	1.13	(-)	(-)	(2.1)	1.23	83/69
9	0.63	1.16	(0.3)	(5.0)	(2.1)	1.18	90/78
10	0.66	1.16	(0.6)	(5.0)	(2.1)	1.11	91/78
11	0.67	1.15	(0.9)	(5.0)	(2.1)	1.07	91/78
12	0.71	1.16	(1.2)	(5.0)	(2.1)	1.00	92/78

Table 4.4 *Parameters obtained by fitting to the E615 data of Ref.* [21] *(exclusive of the two high $\sqrt{\tau}$ bins) using various input sea quark distributions. Set 13 shows the effect of fitting only to data points for which $x_\pi > 0.35$. Fits 14 to 17 show the effect of steadily increasing the sea from one which carries 5% of the pion's momentum at $Q^2 = Q_0^2$, to one which carries 20%. The parameters in brackets are held fixed during each fit.*

fit	α	β	A_s	η_s	η_g	K'_{252}	χ^2/# data
13	0.58	1.11	(-)	(-)	(2.1)	1.20	43/52
14	0.59	1.15	(0.3)	(5.0)	(2.1)	1.22	50/61
15	0.66	1.18	(0.6)	(5.0)	(2.1)	1.11	50/61
16	0.64	1.14	(0.9)	(5.0)	(2.1)	1.11	52/61
17	0.67	1.15	(1.2)	(5.0)	(2.1)	1.05	53/61

Finally we repeat the fit to both the NA10 and E615 data with the valence parameters fixed at the values obtained from the analysis of the other data set. The only free parameters are thus the overall normalization K' factors. The results of these fits can be seen in Tables 4.5 and 4.6. It appears that the main difference between the NA10 and E615 data sets is one of normalization as reflected in the difference between the K' factors.

Table 4.5 *Fits 18 and 19 show how well the valence distributions obtained from the NA10 analysis can describe the data of the E615 experiment by only varying the normalization parameter K'_{252}. The parameters in brackets are held fixed during each fit.*

fit	α	β	A_s	η_s	η_g	K'_{252}	χ^2/# data
18	(0.64)	(1.08)	(0.9)	(5.0)	(2.1)	1.08	102/78
19	(0.64)	(1.08)	(0.9)	(5.0)	(2.1)	1.06	61/61

Table 4.6 *Fit 20 shows how well the valence distributions obtained from the E615 analysis can describe the data of the NA10 experiment by only varying the normalization parameters K'_{194} and K'_{286}. The parameters in brackets are held fixed during each fit.*

fit	α	β	A_s	η_s	η_g	K'_{194}	K'_{286}	χ^2/# data
20	(0.64)	(1.15)	(0.9)	(5.0)	(2.1)	1.37	1.43	66/62

Table 4.7 *The optimum choice of parameters of the pion distributions derived from all the various fits to the NA10 and E615 Drell-Yan data, together with the fits to the WA70 prompt photon data as described in section 4.3.*

Expt.	α	β	A_s	η_s	η_g
NA10	0.64 ± 0.03	1.08± 0.02	0.9± 0.3	5.0	2.1± 0.4
E615	0.64 ± 0.03	1.15± 0.02	0.9± 0.3	5.0	2.1± 0.4

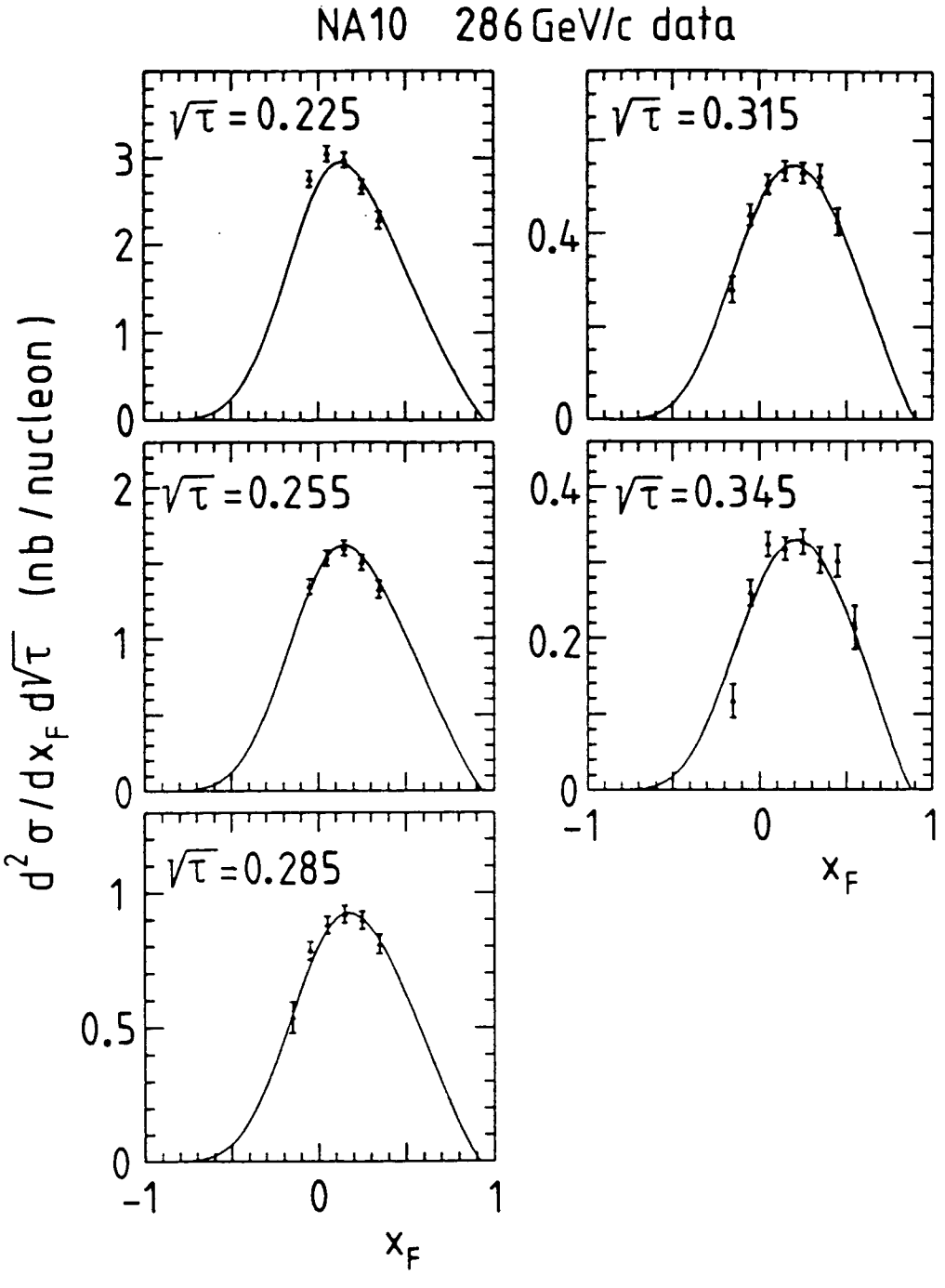

Figure 4.4. Drell-Yan data from the NA10 collaboration [20] for 286 GeV/c π^- on W, together with their description in terms of the NA10 parton distributions of Table 4.7. The points with $x_F < 0$ are not included in the fit.

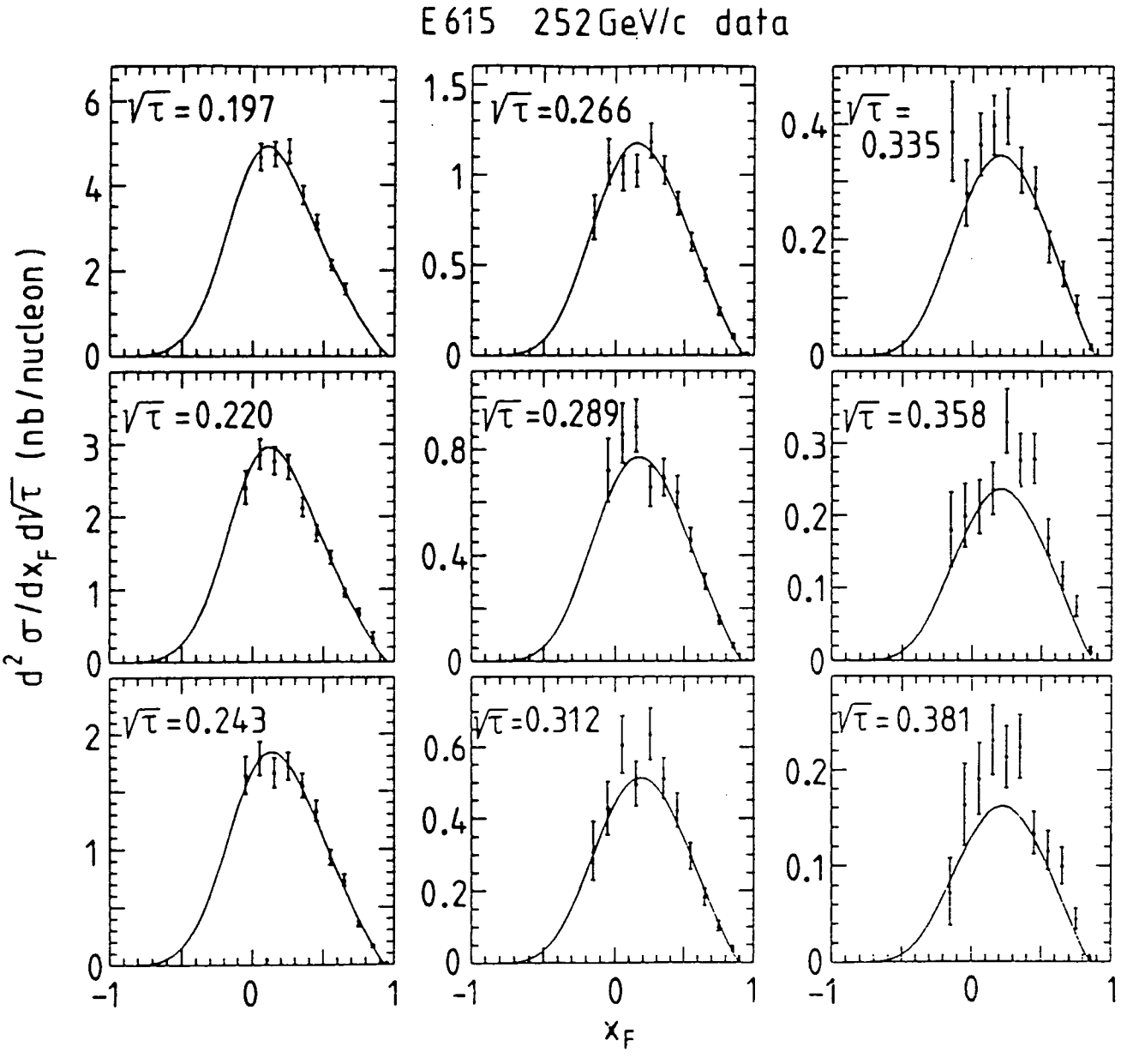

Figure 4.5. Drell-Yan data from the E615 collaboration [21] for 252 GeV/c π^- on W, together with their description in terms of the E615 parton distributions of Table 4.7. The points with $x_F < 0$ are not included in the fit.

As a result of all of the fits to, in turn, two different data sets we see that a consistent value of the parameter α is obtained, but that the parameter β differs slightly according to whether the NA10 or E615 data are used. We find that $\alpha = 0.64 \pm 0.03$ for both the NA10 and E615 data, but that $\beta = 1.08 \pm 0.02$ for NA10, whereas $\beta = 1.15 \pm 0.02$ for E615. For reference these parameter values are collected in Table 4.7; the resulting description of the NA10 and E615 Drell-Yan data is shown in Figs. 4.3, 4.4 and 4.5, while Fig. 4.6 compares the two sets of parton distributions at $Q^2 = 5$ GeV^2.

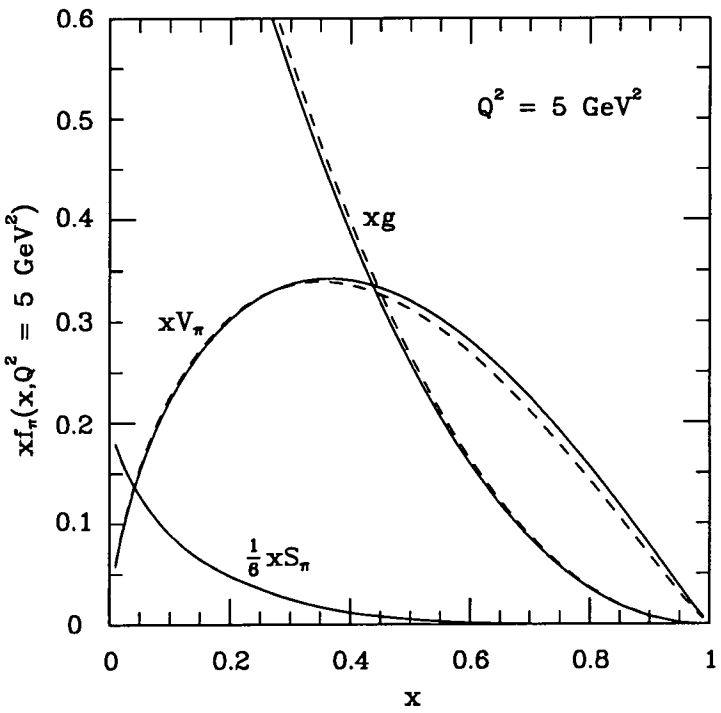

Figure 4.6. The parton distributions of Table 4.7 obtained from the fits to the NA10 (solid curves) and E615 (dashed curves) Drell-Yan data evolved to $Q^2 = 5$ GeV^2.

We note that the errors quoted above do not include those due to the uncertainties in the proton distributions. In order to explore the effect of changing these distributions we

use the four sets of partons (B135, B160, B200, B235) of Ref. [37]. These four sets span the range of acceptable proton distributions and each corresponds to a different value of $\Lambda^{(4)}_{\overline{\rm MS}}$ namely,

$$\Lambda^{(4)}_{\overline{\rm MS}} = 135,\ 160,\ 200,\ 235\ \ {\rm MeV}.$$

We find from the resulting fits to the NA10 data that the optimum value of α varies between 0.62 and 0.64. It therefore remains within the error determined from the fits which use the HMRS(B) set of partons. The value of β increases from 1.07 to 1.12 as the choice of proton distributions varies from B235 to B135 (and $\Lambda^{(4)}_{\overline{\rm MS}}$ decreases). However, it is clear that the uncertainty in β is still dominated by the disagreement between the two different sets of Drell-Yan data. None of the results of the following sections are particularly sensitive to this small difference in β. That is to say, they do not change beyond their quoted errors. We, therefore, use the valence parameters from our NA10 analysis in what follows. We give preference to the NA10 data not only because it has higher statistics, but also because it was the NA10 collaboration which measured the function R. It thus seems more consistent to use their data. Although E615 has data points at higher values of $x_{\rm F}$, these correspond to lower values of x_N where the form of R has not been measured.

4.3 The gluon distribution

The Drell-Yan data does not put any effective constraints on the shape of the gluon distribution of the pion. The gluon dependence only enters at next-to-leading order and even this contribution is considerably smaller than those arising from the other next-to-leading order processes. By contrast the gluon enters at leading order in the prompt photon processes, $\pi^{\pm}p \to \gamma X$. Moreover, in $\pi^{+}p \to \gamma X$, the $gq \to \gamma g$ contribution to the

cross-section is large, if not larger, than that of the $q\bar{q} \to \gamma g$ annihilation diagrams. We determine the gluon distribution of the pion from the data of the CERN WA70 [28] prompt photon experiment. The valence quarks are held fixed at the values determined by the NA10 Drell-Yan data. The calculation of the cross-section for prompt photon production is then performed beyond leading order using the 'principle of minimal sensitivity' to determine the optimized factorization and renormalization scales as described in Ref. [25]. Fig. 4.7 shows, in terms of contours of constant χ^2, the quality of the combined fit to the WA70 π^+ and π^- data as a function of $\langle xg \rangle$ and η_g.

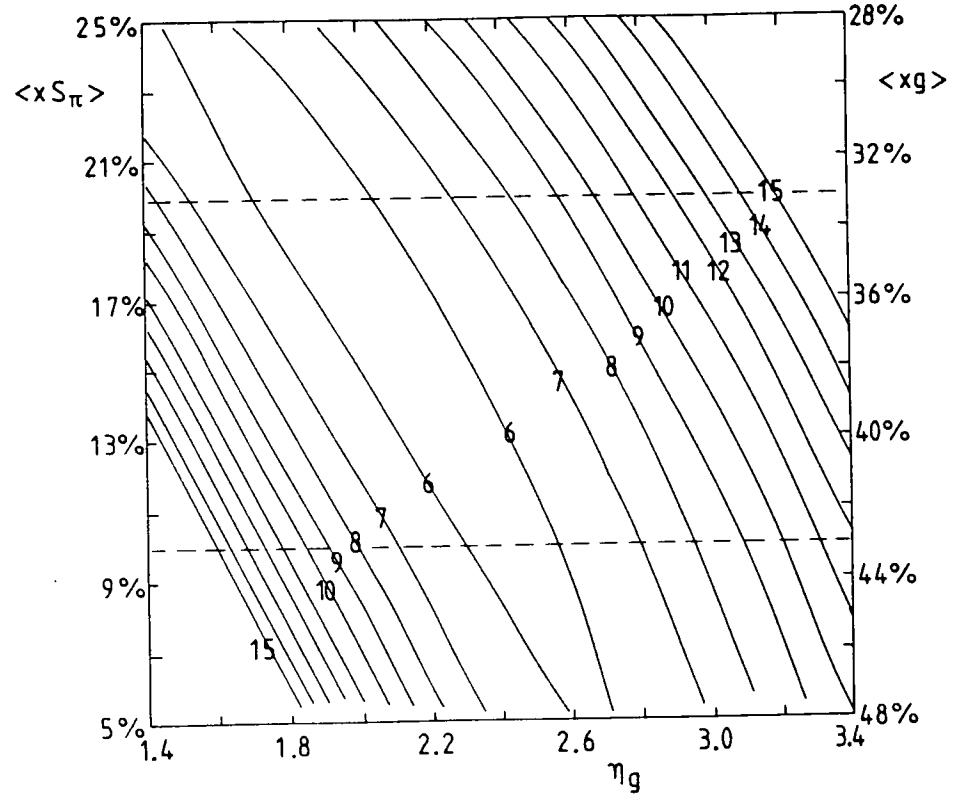

Figure 4.7. Contours of constant χ^2 (with a spacing of 0.5 units) in the plane of $\langle xg \rangle$ and η_g. χ^2 measures the quality of the description of the WA70 prompt photon data $\pi^+ p \to \gamma X$ and $\pi^- p \to \gamma X$ using the valence distributions of Table 4.7 obtained by fitting to the NA10 Drell-Yan data. The valence quarks carry about 47% of the pion momentum; the left and right hand vertical scales show the fraction carried by the sea and gluon respectively. The preferred region lies between the dashed lines.

Now in the proton the gluons are known to carry about 50% of the momentum at $Q^2 = Q_0^2 = 4$ GeV^2. However, for a pion, the valence quarks themselves carry $\frac{2\alpha}{\alpha+\beta+1} \simeq 47\%$ of its momentum at this Q^2. We have found that a sea quark distribution carrying only 5% of the pion momentum gives an unacceptable fit to the NA10 Drell-Yan data (see, for example, set 2 of Table 4.1), so we make the reasonable assumption that the sea quarks carry between 10% and 20% of the pion's momentum, and correspondingly the gluon must carry between 43% and 33% of the momentum. (This is consistent with the original measurement of NA3 [38] who found $\langle xg \rangle = 0.47 \pm 0.15$). We can see from Fig. 4.7 that if we impose the above limit on $\langle xg \rangle$ then the value of η_g which best describes the prompt photon data is $\eta_g = 2.1 \pm 0.4$. Fig. 4.8 shows the fit to the WA70 prompt photon data obtained using $\eta_g = 2.1$. Although the $\pi^- p \to \gamma X$ data do not constrain the gluon, they do serve as a consistency test of the quark distributions obtained from the Drell-Yan data.

An independent determination of the gluon from WA70 data has been made by Aurenche *et al.* [35] using a different choice of proton distributions. Their results are based purely on an analysis of the prompt photon data and thus rely on earlier, and simpler, analyses of Drell-Yan data for the values of certain valence and sea quark parameters. For example, they keep the value of β fixed at 0.85 whereas our analysis favours a larger value ($\beta \simeq 1.1$). For completeness we compare their pion distributions with ours in Fig. 4.9.

4.4 The sea distribution

So far we have seen that the valence quark distribution of the pion, and the exponent η_g of the gluon, are fairly well constrained by Drell-Yan and prompt photon data. The outstanding ambiguity is the size and form of the sea quark distribution of the pion.

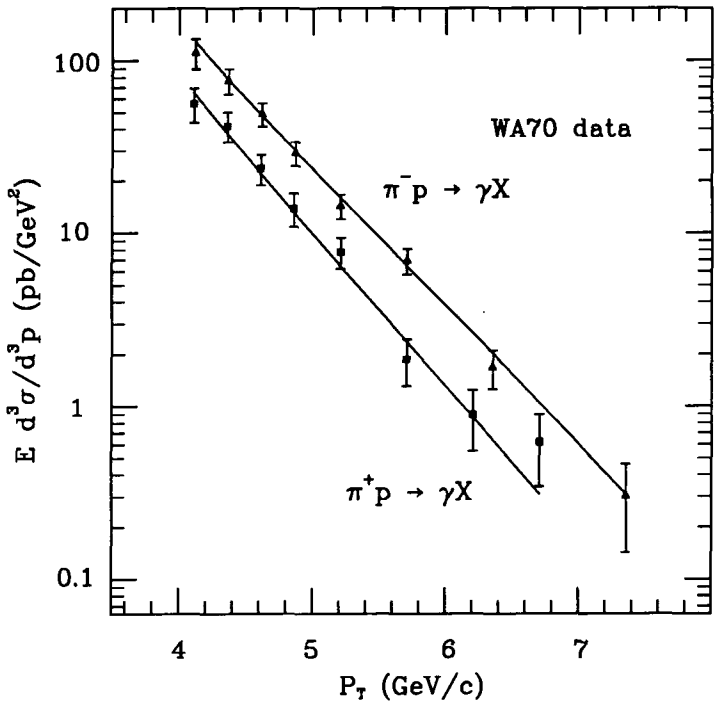

Figure 4.8. Data on the transverse momentum distribution of the photon produced in $\pi^{\pm}p$ collisions at $\sqrt{s}$ = 22.94 GeV from the WA70 collaboration [28] (corrected to y=0) together with the description obtained using the parton distributions from our NA10 and WA70 fits of Table 4.7.

Owens [39] assumed that the sea carried a fraction 0.15 of the momentum of the pion with a $(1-x)^{\eta_s}$ 'starting' distribution at $Q_0^2 = 4$ GeV^2 with $\eta_s = 5$. This value of η_s is to be expected from naïve spectator quark counting arguments. The NA3 collaboration [38], found that their $\pi N \to \mu^+\mu^- X$ data were compatible with a pion sea which carried momentum fraction 0.19, with $\eta_s = 8.4$ at $Q_0^2 \sim 20$ GeV^2. An advantage of the NA3 experiment was the use of π^+ as well as π^- beams. Although the valence distributions of both pions are the same from isospin symmetry, they contribute to the Drell-Yan process differently through the factors of the quark charge squared. However, unlike the proton, where deep inelastic scattering data exist down to $x_N \simeq 0.03$, the pion data exist only

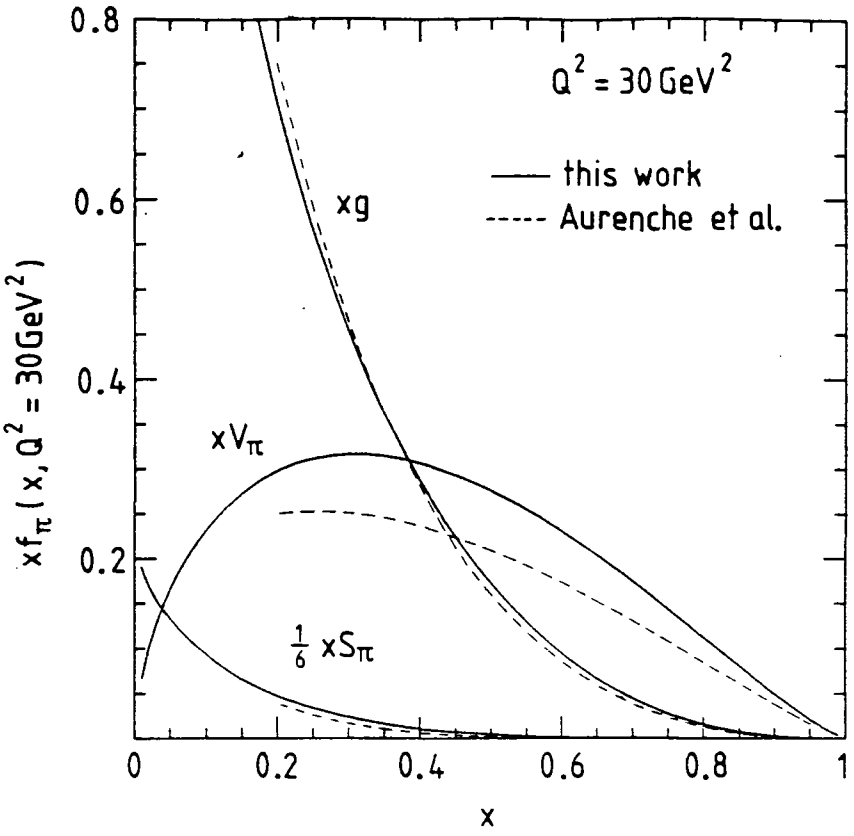

Figure 4.9. A comparison of the pion distributions at $Q^2 = 30$ GeV^2 of Ref. [35] with the equivalent distributions of Table 4.7 which are obtained by fitting to the NA10 Drell-Yan data and WA70 prompt photon production data.

for $x_\pi \gtrsim 0.2$. Unfortunately it is not consistent for us to assume that the sea takes the same form as that of the NA3 parametrization. This is because of the different theoretical inputs used by NA3. Fig. 4.10 shows the distribution $u(x,Q^2) + \bar{u}(x,Q^2)$ as given by the NA3 collaboration at $Q^2 = 20$ GeV^2 compared with our distribution for which we include a range of sea distributions. It is clear that the NA3 quark distributions have a very different form and so it would be meaningless to attempt to incorporate their sea distribution in our analysis. As the NA3 data has never been fully published it is not possible to re-analyse their measured cross-sections to extract a consistent sea distribution. Fortunately, we have seen above that the sea has relatively little influence on our determination of the valence

quark parameters α and β. As we noted in the previous section, the main uncertainty in η_g arises through our lack of knowledge of how the remaining momentum is divided between the sea and gluons (see Fig. 4.7). We have imposed reasonable bounds on this division and varied the sea accordingly. The effect of the variation of the sea is shown in Fig. 4.10. Further experiments with high statistics π^+ and π^- beams, ideally with data below $x_\pi \sim 0.2$, are needed in order to determine more accurately the pion sea.

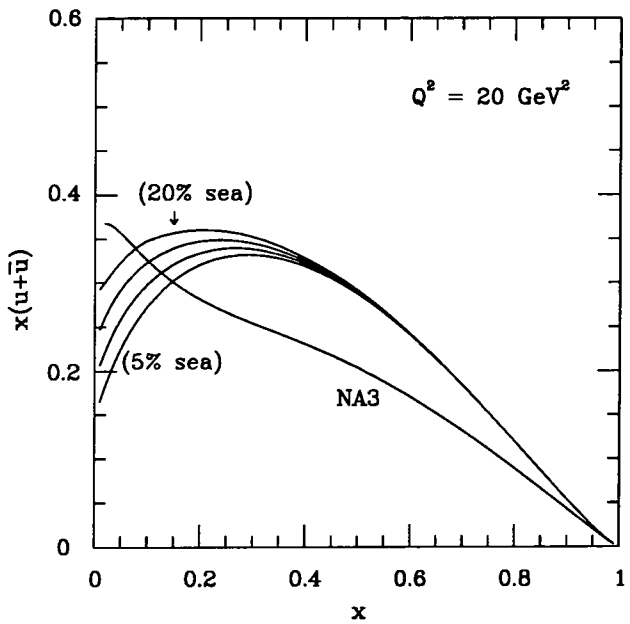

Figure 4.10. A comparison of the NA3 [38] parton distribution $u(x,Q^2) + \bar{u}(x,Q^2)$ at $Q^2 = 20$ GeV^2 with the equivalent distributions of Table 4.7 which were fitted to the NA10 Drell-Yan data. The effect of varying the sea quark distribution is shown.

4.5 Pion Moments

In order to compare with lattice QCD calculations we calculate the first two moments

of the pion valence quark distributions

$$2\langle xV_\pi\rangle = 2\int_0^1 dx\; xV_\pi\,, \tag{4.9}$$

$$2\langle x^2V_\pi\rangle = 2\int_0^1 dx\; x^2V_\pi\,. \tag{4.10}$$

The Q^2 dependence of these moments for the distributions of Table 4.7 obtained from the NA10 data can be seen in Fig. 4.11. At $Q^2 = Q_0^2 = 4$ GeV^2 we have $xV_\pi = A_V x^\alpha(1-x)^\beta$ and thus

$$2\langle xV_\pi\rangle\Big|_{Q^2=Q_0^2} = \frac{2\alpha}{\alpha+\beta+1}\,, \tag{4.11}$$

$$2\langle x^2V_\pi\rangle\Big|_{Q^2=Q_0^2} = \frac{2\alpha\,(\alpha+1)}{(\alpha+\beta+1)\,(\alpha+\beta+2)}\,. \tag{4.12}$$

Equations (4.11) and (4.12) show that the moments are more sensitive to the uncertainty in α than in β.

The first two moments have also been calculated from first principles using lattice QCD [40]. The values at $Q^2 = 49$ GeV^2 are

$$\begin{aligned} 2\langle xV_\pi\rangle &= 0.46 \pm 0.07\,, \\ 2\langle x^2V_\pi\rangle &= 0.18 \pm 0.05 \end{aligned} \tag{13}.$$

This is to be compared with our values

$$\begin{aligned} 2\langle xV_\pi\rangle &= 0.40 \pm 0.02\,, \\ 2\langle x^2V_\pi\rangle &= 0.16 \pm 0.01 \end{aligned} \tag{14}.$$

at the same value of Q^2. The lattice calculation is thus consistent with our phenomenological analysis. It is to be expected that the lattice calculation will be higher than the experimental result as the lattice calculation uses the quenched approximation and hence does not contain any sea quarks. This means that the valence quarks will carry slightly more of the momentum. This effect is included in the quoted error for the lattice moments [40].

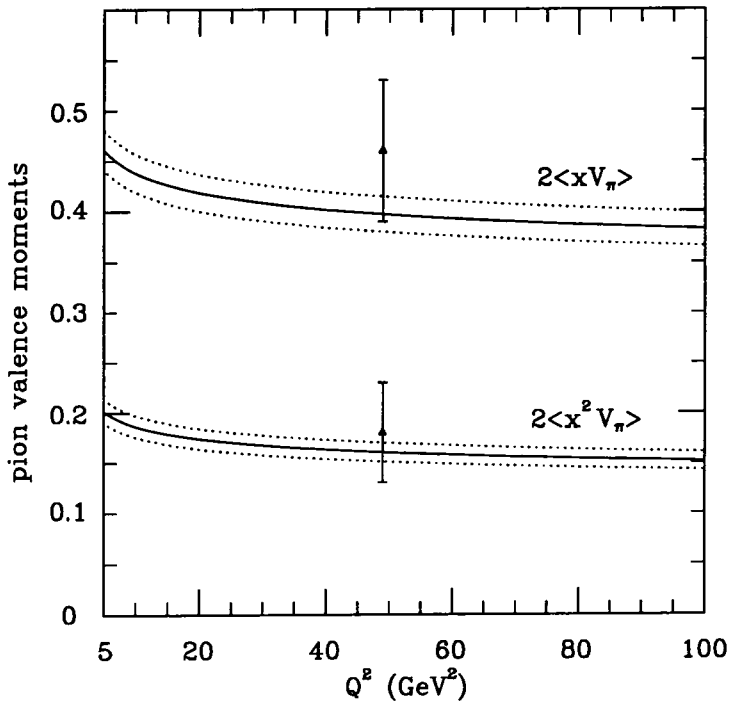

Figure 4.11. The first two moments of the pion valence distribution (solid lines) as predicted from the fit to the Drell-Yan data of NA10 compared with the predictions of lattice QCD [40]. The uncertainty in the valence parameters marks out the regions bounded by the dotted lines.

4.6 Summary

We have determined the parton distributions of the pion using all the relevant available high statistics pion data for Drell-Yan and prompt photon production. We perform a next-to-leading order analysis adopting the same techniques that HMRS [34] used to determine the parton distributions of the proton, except that since we fit to πN data we need to input proton distributions (HMRS) to determine those of the pion.

We find that we are able to obtain a consistent simultaneous description of the NA10 and E615 Drell-Yan data up to normalization factors; the small difference in the parton

distributions is shown in Fig. 4.6. These data primarily determine the valence quark distribution of the pion, whereas the main constraint on the form of the gluon distribution comes from WA70 data on prompt photon production from $\pi^+ p$ interactions.

Of course due to the absence of deep inelastic scattering data we would not expect the pion distributions to be so precisely determined as those of the proton. However, the main deficiency is the lack of pion data with $x_\pi \lesssim 0.2$ to pin down the sea quark distribution. The standard counting rule $(1-x)^5$ form of the sea gives satisfactory fits, but the normalisation is not well determined; a sea which carries either a 10% or 20% fraction of the pion momentum at $Q^2 = 4$ GeV^2 fits the existing data equally well. The fit deteriorates if the fraction is much smaller, and for larger fractions the gluon momentum fraction becomes unacceptably small (recall that the valence quarks carry 47% of the pion's momentum at $Q^2 = 4$ GeV^2). The ambiguity in the sea has little effect on the determination of the valence quark distributions, although it contributes to the uncertainty in the determination of the $(1-x)$ exponent of the gluon, $\eta_g = 2.1 \pm 0.4$, as shown in Fig. 4.7.

Table 4.8 *The parameters of the initial parton distributions of the pion obtained from fitting NA10 and WA70 data and which correspond, respectively, to the sea quarks carrying 10%, 15%, 20% of the momentum of the pion at Q^2=4 GeV^2. The distributions evolved in Q^2 are available as a FORTRAN package as described in the text.*

α	β	A_s	η_s	η_g
0.64	1.08	0.6	5.0	2.4
0.64	1.08	0.9	5.0	2.1
0.64	1.08	1.2	5.0	1.8

Three sets of parton distributions of the pion, which span the ambiguity in the sea, are available as a FORTRAN package in the form of (x, Q^2) grids, together with an interpolation routine, from the PDFLIB compilation in the CERN library [41]. These sets are evolved (to next-to-leading order) from initial distributions given by the parameters

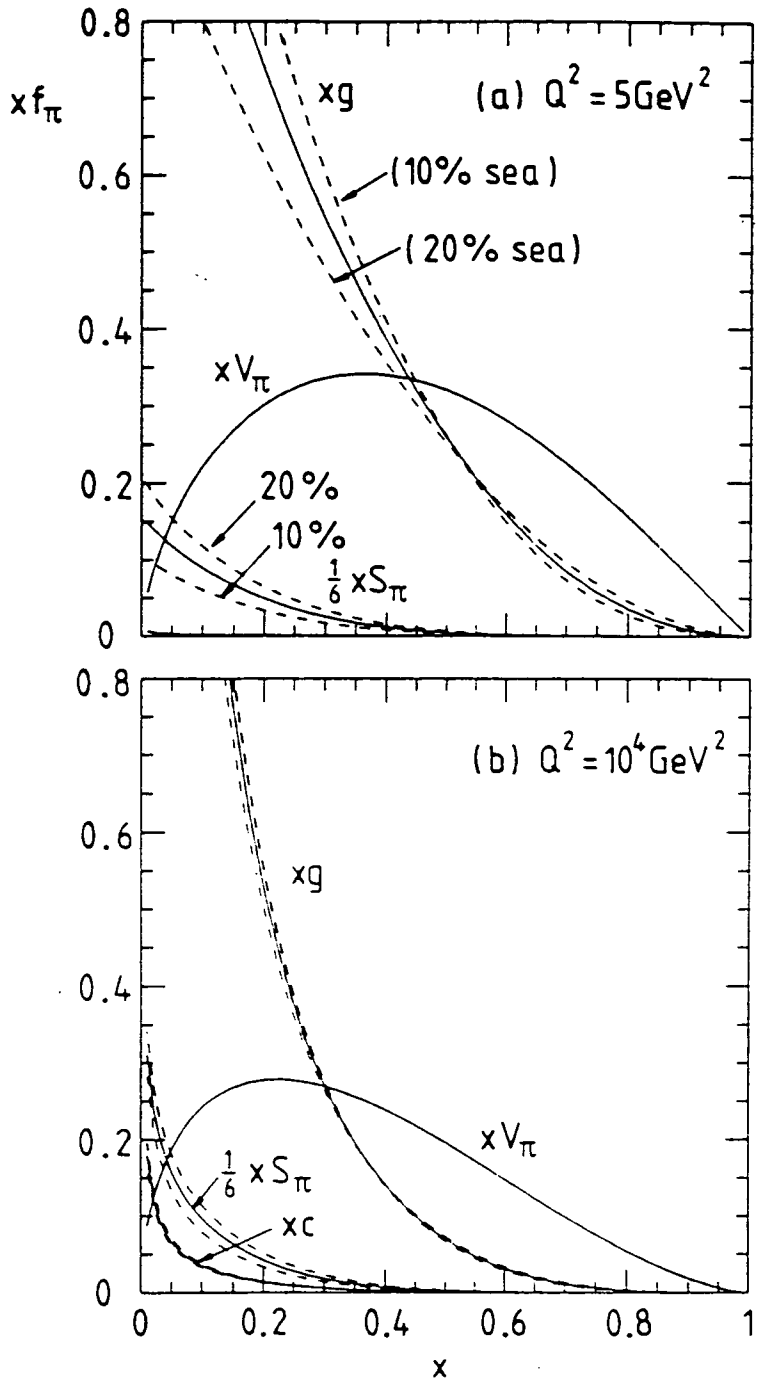

Figure 4.12. The parton distributions of Table 4.8 evolved to (a) $Q^2 = 5$ GeV^2 and (b) $Q^2 = 10^4$ GeV^2. The set for which the sea quarks carry 15% of the pion's momentum at $Q^2 = 4$ GeV^2 is shown as a solid line, and the remaining two sets, for which the sea quarks carry 10% and 20% of the momentum, as dashed lines. The sea quark distribution is defined as $xS_\pi = 2x(u+\bar{d}+\bar{s})$; also shown is the charm quark distribution, $xc = x\bar{c}$.

in Table 4.8 and correspond to sea quark distributions carrying 10%, 15% and 20% of the momentum of the pion; the central set is the optimum solution (shown in Table 4.7) which we obtained by fitting to the NA10 Drell-Yan data. Figs. 12a and 12b show these three distributions evolved to $Q^2 = 5$ GeV^2 and $Q^2 = 10^4$ GeV^2 respectively. The pion distributions are useful for future fixed target physics with pion beams and for (vector) meson dominance applications. Finally we note our results are consistent with the QCD lattice computations of the pion distributions.

5 The small x behaviour of parton distributions

5.1 Introduction

We are now looking ahead to the next generation of colliders. These new machines will have much higher centre of mass energies and will probe the structure of the hadrons at much smaller values of x than ever before. They will form the new testing ground for the standard model and so reliable parton distributions in the relevant (x, Q^2) regions are of vital importance. Meanwhile, the analysis of current fixed target experiments will soon be complete. From these experiments physicists have managed to determine (to reasonable accuracy) the parton distributions of both the nucleon and the pion [32, 42]. The drawback is that the results are only applicable in the region of x covered by the available data ($x \gtrsim 0.01$ for $Q^2 \gtrsim 4$ GeV^2). Obviously for predictions relevant to future colliders there is a need for reliable parton distributions at smaller values of x.

Understanding the behaviour of parton distributions at small Bjørken x is complicated by the eventual failure of perturbation theory in the limit $x \to 0$. This, the so-called "Regge limit", contrasts with the limit $Q^2 \to \infty$ of perturbative QCD. As a result, any perturbative study at small x must be careful to avoid straying into this non-perturbative region.

In this chapter we review the necessary theoretical tools for a perturbative analysis of the small x region. In particular, we examine how QCD at small x differs from the familiar QCD of large x. The phenomenological consequences arising from these differences and their implications for the HERA *ep* collider will then be studied in the remaining chapters.

We begin by defining exactly what is meant by "small x". Recall from Chapter 2 that Bjørken x is given by

$$x = \frac{Q^2}{2P.q} = \frac{Q^2}{2M\nu} \qquad \text{(in the lab frame)} . \tag{5.1}$$

The so-called "small x" region corresponds to the limit

$$2M\nu \gg Q^2 \tag{5.2}$$

where Q^2 is kept large, so that perturbation theory is still valid. Now the centre-of-mass energy squared, s, for the photon-proton subprocess is given by

$$s = (P+q)^2 = -Q^2 + 2P.q + M^2 \tag{5.3}$$

and so the limit (5.2) also corresponds to the (Regge) limit $s \gg Q^2$. In this limit perturbative QCD is expected to breakdown as higher twist $(1/Q^2)$ terms grow and become as large as the leading twist contribution [43]. Despite this failure, it is expected that an intermediate region exists in which perturbative QCD is still applicable. In this transition region we must firstly resum the large logarithms of $1/x$ which occur in the perturbative expansion, and secondly, we must include a subset of Feynman diagrams which are usually neglected. These diagrams represent some of the parton annihilation processes which can become important at small x. Without these diagrams the parton densities can grow without restraint, resulting in cross sections which violate unitarity.

We will begin by considering some of the details of the old 'Regge theory' which pre-dates QCD. This theory proved to be very successful at explaining many of the features observed in strong interaction physics and some of the ideas contained within its

phenomenology have now been given QCD interpretations. In particular the concept of a perturbative Pomeron is very important to QCD at low x. Unfortunately, the general relationship between the two theories is not well understood and we can only hope that further study of the small x region will improve our knowledge in this area.

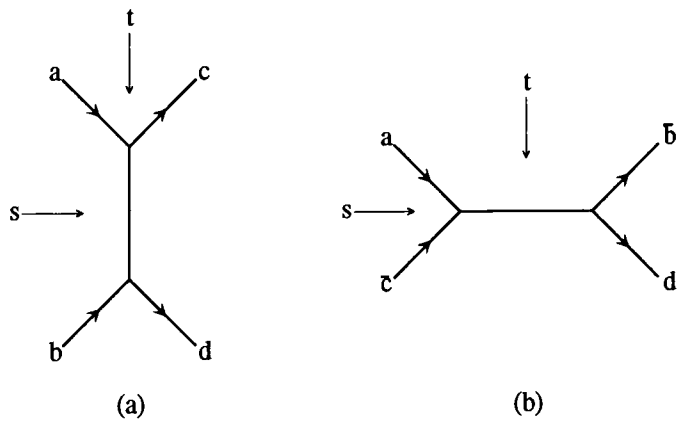

Figure 5.1. (a) The s-channel diagram relevant to the scattering $ab \rightarrow cd$ via particle exchange in the t-channel. Each exchanged particle has $q^2 < 0$ and so can never come close to its mass shell condition $q^2 = m^2$. Crossing s and t leads to the process $a\bar{c} \rightarrow \bar{b}d$, shown in (b), in which the exchange particles now exist in the s-channel with $q^2 > 0$. We expect that the scattering amplitude for process (b) will contain poles when $q^2 \simeq m^2$ and we can therefore approximate the scattering amplitude by the sum of these poles. The relationship between the scattering amplitude for (b) and the scattering amplitude for (a) is given by Regge theory.

5.2 Regge theory

Regge theory originated in the sixties as a way of describing the scattering of strongly interacting particles [44]. Before the discovery of quarks and gluons, the absence of fundamental fields resulted in calculations based instead on the "S-matrix" which describes

the scattering between particles

$$S = I + iA \,. \tag{5.4}$$

Here I is the unit matrix representing processes in which the particles do not interact and A is the scattering amplitude. Regge theory's success was based on its ability to describe the structure of the scattering amplitude for the process $ab \to cd$ (shown in Fig. 5.1a) in terms of the particles created in the crossed process $a\bar{c} \to \bar{b}d$ (Fig. 5.1b). First of all it is necessary to write the scattering amplitude for the above t-channel process in terms of a partial-wave expansion, namely

$$A(s,t) = \sum_{l=0}^{\infty}(2l+1)A_l(t)P_l(z_t) \,. \tag{5.5}$$

Unfortunately this equation is only valid in the physical t-channel region, (where, for equal masses, $t > 4m^2$ and $s < 0$) rather than in the physical s-channel region (where, for equal masses, $s > 4m^2$ and $t < 0$) where we want to use it. If we try applying Eq. (5.5) in the physical s-channel region then we find that the presence of high-spin particles produces an unacceptable behaviour at large s of the form

$$A(s,t) \sim P_l(z_t) \sim {z_t}^l \sim s^l \tag{5.6}$$

and such a rapid growth of the amplitude with s is forbidden by unitarity constraints [45]. Instead it is necessary to define an analytic continuation of the partial wave amplitude, $A_l(t)$, to complex values of the angular momentum l. Regge theory then predicts that the scattering amplitude in the physical s-channel region is given (at large s) by the formula

$$A(s,t) = \sum_i \beta_i(t) s^{\alpha_i(t)} \tag{5.7}$$

where the contributions from the t-channel exchange particles now lie on so-called "Regge trajectories", $\alpha(t)$. Each of these Regge trajectories describes the (t-dependent) position of a pole in the complex l plane

$$l = \alpha(t) \tag{5.8}$$

Whenever the real part of such a trajectory passes through an even integer $2n$ (or, if the trajectory has an odd signature, through an odd integer, $2n+1$) there exists a particle of spin $2n$ $(2n+1)$ and mass $m = \sqrt{t}$. All of the particles (bound states and resonances) lying on any one trajectory are found to share the same internal quantum numbers (such as charge and flavour) and differ only in their masses and spins. Fermionic particles are likewise found to lie on Regge trajectories connecting half-integer spin. When the Regge pole trajectories are plotted as $Re(\alpha)$ versus t they appear as approximately straight lines with slopes $\alpha' \simeq 1$ GeV^2 (as shown in Fig. 5.2).

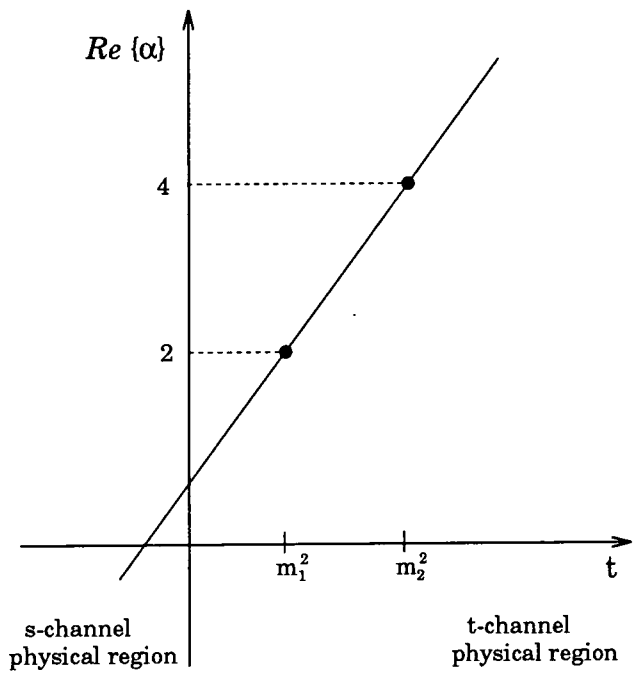

Figure 5.2. A typical Regge trajectory. This trajectory connects a particle of mass m_1^2 and spin 2 with a particle of mass m_2^2 and spin 4.

If we compare Eq. (5.6) and Eq. (5.7) then we see that, although they both predict a behaviour of the form $A \sim s^l$, the crucial difference is now the t-dependence arising from Eq. (5.8). The resulting behaviour is now physically acceptable when $A(s,t)$ is

continued into the physical s-channel region. The trajectories effectively reduce the high-spin, $\alpha_i(m_i^2) = l$, term of the physical t-channel region to the much lower $\alpha(t < 0)$ value inside the physical s-channel region.

With the aid of the optical theorem the relationship (5.7) can reveal the behaviour of the total cross section, $\sigma_{\rm tot}(a + b \to X)$, in the high-energy limit, $s \to \infty$. The optical theorem relates the imaginary part of the forward ($t = 0$) scattering amplitude to the total cross section via

$$\text{Im } A \;=\; s\sigma \tag{5.9}$$

and consequently we see that Regge theory predicts a behaviour

$$\sigma \;\sim\; s^{\alpha(0)-1} \tag{5.10}$$

for the total cross section at high energy. The value of the trajectory function $\alpha(t)$ at $t = 0$ is known as the Regge intercept and from Eq. (5.10) we see that it is the intercept which controls the high-energy behaviour of the cross section.

The early scattering experiments found that the high-energy behaviour of the cross section was approximately $\sigma \sim$ const. If this is due to a dominant Regge pole trajectory then, from Eq. (5.10), this trajectory must have an intercept $\alpha(0) \sim 1$. However, all of the trajectories corresponding to known t-channel particle exchanges have intercepts less than one and so their contributions to σ diminish with increasing energy. The proposed exchange [46] which generates the dominant Regge trajectory is known as "the Pomeron" (Fig. 5.3) and is responsible for elastic and diffractive scattering (i.e. processes in which there is no net flavour transfer between the particles). Although it was originally thought to have an intercept of 1 due to the observed behaviour $\sigma \sim$ constant, more recent scattering data show σ rises slowly with s which suggests an effective Pomeron intercept of about 1.1. In QCD, each of the Regge poles describing t-channel particle exchange (the Reggeons) can be represented in terms of quark-antiquark pairs and so the question naturally arises as to

the nature of the Pomeron exchange. The most obvious candidate is some kind of multiple (colourless) gluon exchange, although this has yet to be verified. Indeed, the precise nature of the Pomeron is still obscure and it may well turn out to be some complicated object which only simulates the properties of a pole at currently available energies.

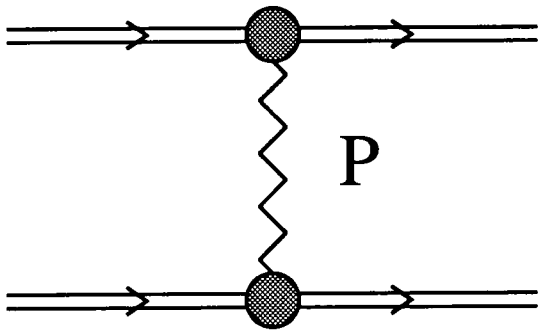

Figure 5.3. Diffractive scattering of two protons via Pomeron exchange.

We may apply these Regge arguments to the virtual photon-parton cross section and hence estimate, in the parton model, the small x behaviour of the quark and gluon distributions [47]. Noting

$$\sigma \propto \sum_i x f_i \sim \sum_R s^{\alpha_R(0)-1} \tag{5.11}$$

we have

$$f_i \sim s^{\alpha} \sim \nu_i^{\alpha} \sim x^{-\alpha} \tag{5.12}$$

as $x \to 0$, where α is the leading Regge intercept for parton i. Hence the (flavour-transfering) valence quarks are expected to behave as $xq_v \sim x^{1/2}$, (reflecting their dependence on the leading meson trajectory), whilst the (flavour independent) sea-quark and gluon distributions are controlled by the Pomeron intercept and are thus expected to behave as xq_s, $xg \sim$ const.

5.3 Perturbative QCD at small x

The traditional evolution equations of QCD, namely the Altarelli-Parisi equations (2.26, 2.27), are not valid at small x. The problem is that they neglect logarithms of $(1/x)$. Under normal circumstances we can ignore these logarithms, but obviously as $x \to 0$ they become important. The equation which correctly sums these $\log(1/x)$ terms was first written down by Balitsky, Fadin, Kuraev and Lipatov and is known as the Lipatov or BFKL equation [48, 49]. This is the equation we must solve if we wish to study the physics of the small x region. However, before we go on to study it in detail we will examine a simpler case which demonstrates many of the features of interest and is applicable to the small x, large Q^2 region. It is called the double leading logarithm approximation (DLLA).

The DLLA is based on a summation of large logarithms of both $1/x$ and Q^2. That is to say, only terms in the perturbative expansion which include logarithms of both $1/x$ and Q^2 are retained. In physical (or axial) gauges these large logarithms are generated by a particular subset of Feynman diagrams, of which a typical example is shown in Fig. 5.4a. This diagram can be viewed as a space-time picture of a parton losing longitudinal momenta, xP, via the emission of other partons. In the DLLA the parton also gains transverse momenta, k_T^2, during this process.

The evolution of Fig. 5.4a is related, via the optical theorem, to the so-called "ladder diagrams" shown in Fig. 5.4b. At small values of x the dominant contribution to the cross section comes from ladder diagrams with only gluons present. This is because the s dependence of the cross section is determined by the spins of the t channel particles and the largest contribution comes from spin 1 gluons rather than spin 1/2 quarks. Of course, we intuitively expect the gluon to be the dominant parton at small x because the valence quark distributions vanish as $x \to 0$, whilst the sea quarks are driven by the gluon via $q\bar{q}$ production.

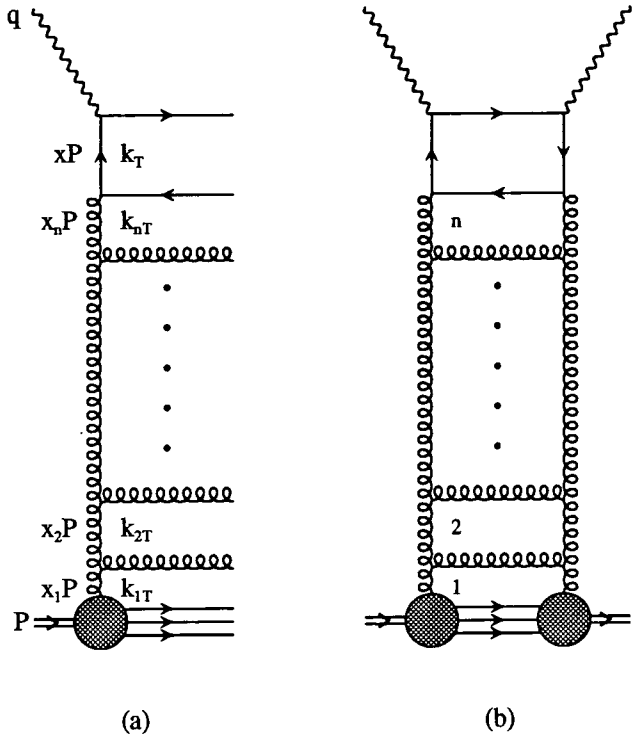

Figure 5.4. Diagrammatic representation for probing the gluon content of the proton at high Q^2. In the DLLA the transverse (k_{iT}) and longitudinal (x_iP) are strongly ordered along the chain. On squaring the amplitude of Fig. (a) we generate the ladder diagram of Fig. (b).

In the DLLA the parton evolution produces a strong ordering of the transverse momenta.

$$Q^2 \gg k_{n_T}^2 \gg k_{n-1_T}^2 \gg \ldots \gg k_{1_T}^2 \gg Q_0^2 \,. \tag{5.13}$$

Whilst the usual ordering of the longitudinal momenta

$$x \lesssim x_n \lesssim \ldots \lesssim x_2 \lesssim x_1 \lesssim 1 \tag{5.14}$$

becomes strong as well, so that

$$x \ll x_n \ll \ldots \ll x_2 \ll x_1 \ll 1 \tag{5.15}$$

With these approximations it can be shown [50] that each rung of a ladder will generate a $\log k_T^2$ and a $\log(1/x)$ term from the relevant nested integrations. The contribution, T_n, from a diagram with n rungs satisfies (for a fixed coupling α_s) the recurrence relation

$$T_n \sim \frac{3\alpha_s}{\pi}\left[\frac{1}{n}\ln(\frac{1}{x})\right]\left[\frac{1}{n}\ln(k_T^2)\right]T_{n-1} \tag{5.16}$$

The sum of all such ladders then yields

$$xg(x,Q^2) = \sum_n \frac{(\frac{1}{4}u^2)^n}{(n!)^2} = \mathrm{I}_0(u) \tag{5.17}$$

where $u^2/4 = 3\alpha_s \ln(Q^2)\ln(1/x)/\pi$ and I_0 is a modified Bessel function. At small x this behaves as

$$xg(x,Q^2) \sim \exp\left[2\sqrt{3\alpha_s \ln(Q^2)\ln(1/x)/\pi}\right] . \tag{5.18}$$

If we include the running of the coupling, α_s, then $\alpha_s \ln(Q^2)$ becomes $\xi(Q^2) \propto \ln(\ln(Q^2))$. We see from Eq. (5.18) that the resulting gluon distribution increases faster than any power of $\ln(1/x)$, but slower than any (negative) power of x. Of course, at finite Q^2 we need to sum all the leading logarithms of $1/x$, not just those which accompany a logarithm of Q^2. This more general summation is known as the leading $\log(1/x)$ approximation (LL$(1/x)$A), the product of which is the Lipatov equation. In order to obtain the leading $1/x$ terms it is necessary to drop the strong ordering of the transverse momenta, k_T^2, and integrate over the full k_T phase space. As a result the Feynman diagrams which generate the Lipatov equation turn out to be rather complex. As well as diagrams with a ladder-like structure, there are also non-ladder contributions from diagrams with virtual corrections [51]. This multiple-gluon exchange is sometimes referred to as "the Lipatov Pomeron" in analogy to the "soft" Pomeron of Regge theory. However, it should be stressed that the two objects are quite different. The first describes hard (perturbative) interactions, whilst the second describes soft processes and therefore exists outside of the domain of perturbation theory.

Both the LL$(1/x)$A and the DLLA formalisms predict the general evolution of a gluon with momenta xP and k_T^2 from an equation of the form

$$f(x,k_T^2) = f^{(0)}(x,k_T^2) + \int dk'^2_T\, K(k_T,k'_T) \int_x^1 \frac{dx'}{x'} f(x',k'^2_T) \tag{5.19}$$

where

$$f(x,k_T^2) \equiv \left.\frac{\partial\,(xg(x,Q^2))}{\partial \ln(Q^2)}\right|_{Q^2=k_T^2} \tag{5.20}$$

That is to say f corresponds to the unintegrated gluon distribution. The difference between the DLLA evolution equation and the Lipatov (LL$(1/x)$) equation is contained only in the form of the kernel K. For the DLLA the kernel is particularly simple, having the form

$$K(k_T,k'_T) \;=\; \frac{3\alpha_s}{\pi}\,\frac{1}{k_T^2}\,\theta(k_T^2 - k'^2_T) \tag{5.21}$$

where the θ function arises from the strong ordering of the transverse momenta in the ladder diagram of Fig. 5.4. For the Lipatov equation the kernel is more complicated

$$K(k,k') = \frac{3\alpha_s}{\pi}\,k^2\left\{\frac{1}{k'^2|k'^2-k^2|} - \beta(k^2)\,\delta(k^2-k'^2)\right\} \tag{5.22}$$

where we have written $k^2 \equiv k_T^2$ for the transverse momenta. The function β is given by

$$\beta(k^2) = \int \frac{dk'^2}{k'^2}\left\{\frac{1}{|k'^2-k^2|} - \frac{1}{(4k'^4+k^4)^{\frac{1}{2}}}\right\}. \tag{5.23}$$

The first term in Eq. (5.23) corresponds to diagrams with only real gluon emission, whereas the second allows for those diagrams with virtual corrections. The apparent singularity at $k'^2 = k^2$ cancels between the real and virtual corrections to the kernel. The inhomogeneous term $f^{(0)}(x,k^2)$ represents the gluon-proton coupling as indicated by the shaded region of Fig. 5.4. Examples of the simplest contributions to $f^{(0)}$ are the diagrams shown in Fig. 5.5 in which the gluons are radiated from valence quarks. If $f^{(0)}(x,k^2)$ was generated by only these types of diagrams then it would be expected to vanish at $k^2 = 0$ and to be independent of x in the small x limit.

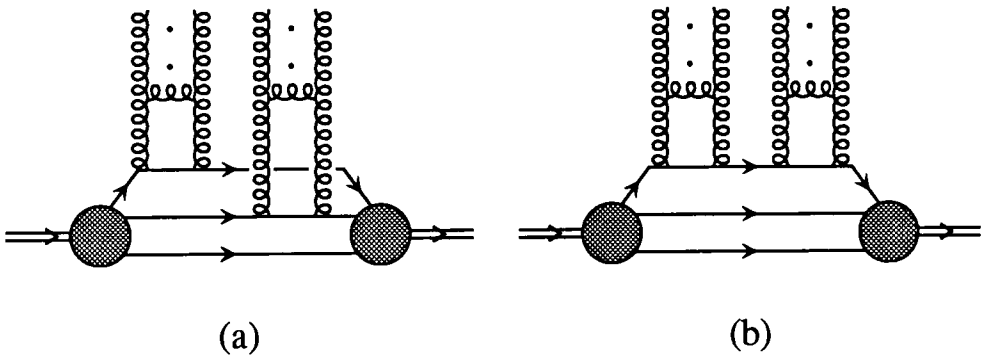

Figure 5.5. Two possibilites for the coupling of the proton to the gluon ladders. In (a) the ladders arise from different constituents of the proton, and in (b) from the same constituent.

Inserting the kernel (5.22) into Eq. (5.19) we find

$$x\frac{\partial f(x,k^2)}{\partial x} = \frac{3\alpha_s(k^2)}{\pi}k^2\int_0^\infty \frac{dk'^2}{k'^2}\left[\frac{f(x,k'^2)-f(x,k^2)}{|k'^2-k^2|}+\frac{f(x,k^2)}{(4k'^4+k^4)^{\frac{1}{2}}}\right] \qquad (5.24)$$

where we have dropped the inhomogeneous term corresponding to the variation of $f^{(0)}$ with x, namely, $\partial f^{(0)}(x,k^2)/\partial \ln(1/x)$. This equation presents various problems when one attempts a solution. The first is that with a running coupling the equation is divergent at low values of k^2. A second problem is that the equation is based on the perturbative form of the gluon propagator and thus again ceases to be valid at low k^2. Both of these difficulties reflect the fact that the low k^2 part of the integration is actually in the non-perturbative region. In order to avoid these problems it is necessary to adopt one of several possible procedures. One method is to try and model the physics in the low k^2 region, for example by including non-perturbative gluon propagators in the calculation, alternatively one can simply cut off the lower limit of integration at some suitably small (but still perturbative) value of k^2. The hope is that when perfoming calculations in the "semi-hard region" (where $k^2 \gtrsim 4$ GeV^2 and x is small) that these non-perturbative effects

are not particularly important. In what follows we shall adopt this second procedure and impose a cut-off, k_0^2, on the transverse momenta exchanged by the perturbative gluons. We shall explore in the following chapter the sensitivity of the results to the value of this arbitrary cut-off. In particular we shall study the effect on the overall normalization of the gluon distribution, and more importantly, on the behaviour of the leading eigenvalue λ_{max} of the Lipatov kernel.

What about the upper limit of Eq. (5.24)? Traditionally it is taken to be infinity, but there have been various suggestions that one should impose an ultra violet cut-off, k_F^2 [52]. In practice, the presence of an upper cut-off greatly simplifies the numerical analysis of such an equation, and we shall use this fact to our advantage in the next chapter. Fortunately it appears that the exact nature of the upper limit is somewhat irrelevant when the coupling is allowed to run [53]. We can therefore write the Lipatov equation in the form

$$x\frac{\partial f(x,k^2)}{\partial x} = \frac{3\alpha_s(k^2)}{\pi}k^2\int_{k_0^2}^{k_F^2}\frac{dk'^2}{k'^2}\left[\frac{f(x,k'^2)-f(x,k^2)}{|k'^2-k^2|}+\frac{f(x,k^2)}{(4k'^4+k^4)^{\frac{1}{2}}}\right]. \tag{5.25}$$

This is the equation that we shall solve in Chapter 6 to determine the gluon distribution, $xg(x,Q^2)$. We shall be able to compare its solutions with our expectation that — at sufficiently small x — the solution will be controlled by the leading eigenvalue, $\lambda_{\max}$, of the Lipatov kernel. This small x behaviour takes the form

$$xg(x,Q^2) \sim x^{-\lambda_{\max}}\, h(Q^2) \tag{5.26}$$

where $\lambda_{\max}$ is given by

$$\lambda_{\max} = \frac{3\alpha_s}{\pi}4\ln 2 \tag{5.27}$$

for a fixed coupling α_s [54] and

$$\frac{3.6}{\pi}\alpha_s(k_0^2) \;\leq\; \lambda_{\max} \;\leq\; \frac{12\ln 2}{\pi}\alpha_s(k_0^2) \tag{5.28}$$

when the coupling is allowed to run [55]. From Eq. (5.27) we see that if $\alpha_s \sim 0.2$ then $\lambda_{\max} \sim 0.5$ and so we expect an x behaviour of $xg \sim x^{-1/2}$ as $x \to 0$. This behaviour is far more stable to evolution in Q^2 than that of the older, more traditional distributions

$$xg(x, Q_0^2) = A_g x^{\delta}(1-x)^{\eta} \tag{5.29}$$

obtained from "starting" parton distributions at $Q^2 = Q_0^2$ with the choice $\delta = 0$. This choice of δ was motivated by the original expectation that the Pomeron intercept was $\alpha_p(0) = 1$ and results in a starting distribution which behaves as

$$xg(x, Q_0^2) \to \text{ constant} \qquad \text{as} \quad x \to 0\,. \tag{5.30}$$

The parametrization (5.30) does not, however, maintain this behaviour as Q^2 increases, but becomes much steeper at small x. Moreover, any downwards evolution in Q^2 produces negative values for the gluon distribution. These problems do not arise in parametrizations with $\delta < 0$ which are very stable to Q^2 evolution. Indeed, with an initial parametrization based on the solution of the Lipatov equation (for example, (5.29) with $\delta = -0.5$), it is possible to evolve upwards in Q^2 with the Altarelli-Parisi equations and still retain the Lipatov-like behaviour of the distribution. This procedure has been adopted in some recent NLO fits [50, 56].

5.4 Shadowing

If the gluon density increases without constraint at small x then it will produce cross sections which violate the limit known as "the Froissart bound" [45]. This bound determines the upper limit for the growth of the cross section (at asymptotically large values of s) and is based on analyticity and unitarity constraints. It shows that the cross section

cannot increase faster than $\ln^2(s)$ as $s \to \infty$ (or, equivalently, as $x \to 0$). Obviously there must be some mechanism which limits the growth of the gluon distribution at small x and thus prevents the cross section from increasing too rapidly. Indeed, it should be fairly clear that if the density of gluons inside the proton becomes large, then the probability for two gluons to interact and recombine into a single gluon is no longer negligible. These recombination processes are able to counteract the increase due to gluon emission. Figure 5.6 shows a typical recombination process in which two gluon ladders fuse into a single ladder. These "fan diagrams" do not generate large logarithms of $1/x$ or Q^2, instead their inherent smallness is compensated by the size of the gluon distribution itself.

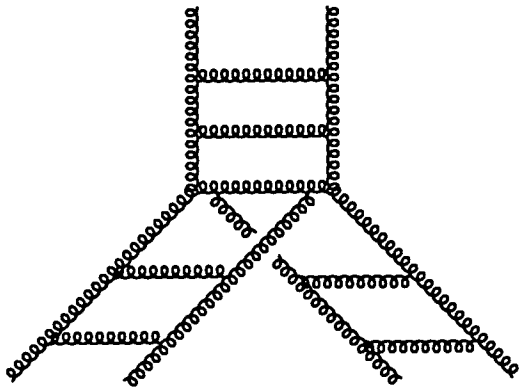

Figure 5.6. Diagrammatic representation of one of the recombination processes which give rise to the quadratic shadowing term present in Eq. (5.33).

It is possible to see, roughly, where these recombination processes become important in the gluon's evolution by studying a simple geometrical picture. Consider a frame in which the proton momentum P is large and also $xP \gg Q$. In this frame a measurement of $g(x, Q^2)$ probes a gluon of transverse size $1/Q$ but much smaller longitudinal size $\sim 1/Px$,

so that the proton appears as a thin disk (see Fig. 5.7). As a result we can neglect the longitudinal dimension and work only in terms of the transverse area. The important parameter is then

$$W \sim \frac{n_g \hat{\sigma}}{\pi R^2}, \tag{5.31}$$

where n_g is the number of gluons in the cell $(\mathrm{d}x/x)\mathrm{d}Q^2$, $\hat{\sigma}$ is the gluon-gluon cross section and πR^2 is the transverse area of the proton. If we note that the number of gluons, n_g, is simply $xg(x,Q^2)$ and that the gluon-gluon cross section is given by $\hat{\sigma} \sim \alpha(Q^2)/Q^2$ then we see that

$$W \sim \frac{\alpha_s(Q^2)}{\pi R^2 Q^2} xg(x,Q^2)\,. \tag{5.32}$$

When this parameter becomes large ($\sim O(\alpha_s)$) our geometrical picture suggests that the interactions between individual gluons will become important. Each gluon within the $(\mathrm{d}x/x)\mathrm{d}Q^2$ cell occupies a transverse area $\sim 1/Q^2$ and thus the total area covered by gluons is simply n_g/Q^2. As x decreases n_g will increase and there must come a point at which $n_g/Q^2 > \pi R^2$ (see Fig. 5.7). At this point the gluons will overlap within the proton, and thus gluon-gluon interactions can no longer be neglected.

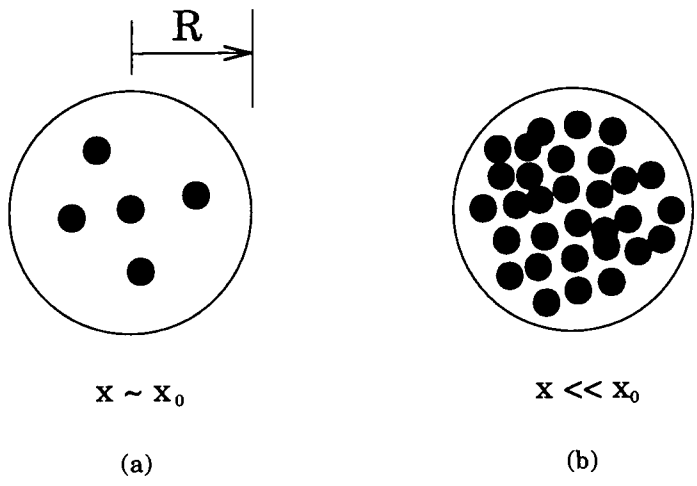

Figure 5.7. How the proton in the frame $xP \gg Q^2$ appears to a gluonic probe at (a) $x \sim x_0$ and (b) $x \ll x_0$.

In the above argument the radius R was assumed to be that of the proton ($R \sim 5$ GeV^{-1}). This is dependent on the gluons ladders coupling to different partons as shown in Fig. 5.5a. However, it has been argued that the gluon ladders may couple to the same parton (Fig. 5.5b) leading to higher gluon concentrations in this parton's vicinity. Such "hot-spots" would require a smaller value of R to reflect the faster onset of gluon-gluon interactions around the radiating parton and a suitable value should, therefore, represent the transverse size of a (valence) quark, $R \sim 2$ GeV^{-1}. Both these cases are of course a simplification of the actual situation. In reality the parameter R is generated from the coupling of the gluon ladders to the proton of which Figs 5.5a and 5.5b are only the simplest possible diagrams. The true R parameter can thus be expected to depend slightly on both x and Q^2.

Our next step is to include the effects of recombination into the gluon evolution equation. The relevant shadowing term has been calculated by Mueller and Qiu [57] and leads to a modified evolution equation of the form

$$x\frac{\partial f(x,k^2)}{\partial x} = \frac{3\alpha_s(k^2)}{\pi}k^2\int_{k_0^2}^{k_F^2}\frac{dk'^2}{k'^2}\left[\frac{f(x,k'^2)-f(x,k^2)}{|k'^2-k^2|}+\frac{f(x,k^2)}{(4k'^4+k^4)^{\frac{1}{2}}}\right] - \frac{81\alpha_s^2(k^2)}{16R^2k^2}[xg(x,k^2)]^2\,. \tag{5.33}$$

This is often referred to as the Gribov-Levin-Ryskin (GLR) equation [51]. Notice that, as written, the non-linear shadowing term is not part of the LL($1/x$) approximation. It is based on a strong ordering of the transverse momenta inside the triple vertex which couples two gluon ladders into a single gluon ladder (Fig. 5.8).

In principle we should replace the $[xg(x,k^2)]^2$ term in the non-linear part with

$$\left[\int_{k_0^2}^{\infty}\frac{\mathrm{d}k'^2}{k'^2}V(k,k')f(x,k'^2)\right]^2 \tag{5.34}$$

where $V(k,k')$ specifies the structure of the triple vertex. The form of V has not been calculated to LL($1/x$) accuracy, and so it is necessary to resort to the strong ordering

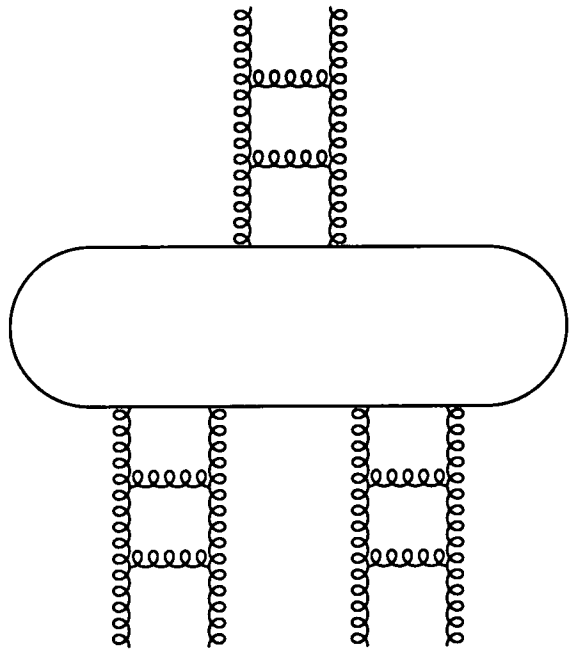

Figure 5.8. The "triple Pomeron vertex"

approximation in which $V(k,k')$ is replaced with $\theta(k^2-k'^2)$. This approximation leads to the shadowing term present in Eq. (5.33). Even if it were known to LL($1/x$) accuracy, the non-linear term represents only a "first order" approximation to the possible shadowing contributions. As we go to smaller and smaller values of x further sets of Feynman diagrams will become important and we can monitor the importance of these higher-order contributions by studying the value of the parameter W. When this parameter is small ($\lesssim O(\alpha_s)$) it is sufficient to include only the first order term, but when it is large ($\gtrsim O(\alpha_s)$) the higher orders can no longer be neglected. No-one has yet attempted a calculation of these higher terms, although Mueller has presented a possible model of shadowing in the ultra-high gluon limit, $W \sim 1$ [58]. Of course if we go to very small values of x then eventually any perturbative approach will break down and we find ourselves in the Regge domain of non-perturbative physics.

5.5 Summary

In this chapter we have seen how parton evolution at small x can be calculated using perturbative QCD techniques. This is despite the fact that ultimately perturbation theory must fail as $x \to 0$. We began by noting that the $x \to 0$ limit corresponds to the Regge limit $s \gg Q^2$ and so, as a consequence, we reviewed some of the fundamental aspects of Regge theory. One of the most important predictions of this theory is the domination of the high-energy cross section by the Pomeron, an exchange mechanism responsible for diffractive scattering.

After Regge theory we turned our attention to the evolution equations of perturbative QCD and saw that the LL(Q^2) equations of Altarelli-Parisi do not include the large logarithms of $1/x$ which are present at small x. The equation which correctly resums these logarithms is the LL($1/x$) equation of Balitsky, Fadin, Kuraev and Lipatov [48] (The Lipatov equation). Not only does this equation generate the perturbative (hard) Pomeron of QCD, but it also predicts that the gluon density will increase rapidly as $x \to 0$. This results in cross sections which rise faster than the Froissart bound allows, resulting in a violation of unitarity. The cure to this problem exists in the form of the parton-parton recombination diagrams which become important at small x. The size of these recombination effects is dependent on the size of the area in which the gluons are concentrated in the proton. The two extremes which we considered were: firstly, gluons spread evenly throughout the entire hadron; and secondly, gluons concentrated in "hot-spots" around, for example, individual valence quarks. The region of the (x, Q^2) plane where the recombination effects are important is known as the transition region and lies between the regions of perturbative and non-perturbative physics. In our analysis we only considered a 'first-order' contribution to these processes, but at very small values of x we expect further corrections to become important.

In the remaining chapters of this thesis we will examine the consequences of the Lipatov equation. Chapter 6 is concerned with the behaviour of the gluon distribution at small x. It is here that we will see the gluon distribution develop the predicted $x^{-\lambda}$ type behaviour and how this growth is tamed by the shadowing contributions. We will also study the location of the transition region and examine its relevance to the HERA ep collider. Following this, in Chapter 7, we will study in detail a suggestion that a powerful way to identify the Lipatov Pomeron is the measurement of deep-inelastic scattering events which contain an extra jet. Finally, in Chapter 8 we will examine whether such events can be reliably measured at HERA.

6 QCD predictions for the small x behaviour of the gluon

6.1 Introduction

The behaviour of the gluon distribution inside the proton is of extreme interest for experiments now in progress at HERA [59]. These experiments are expected to probe down to very small values of x ($x \sim 10^{-4}$) which are well beyond the (perturbative) range of current fixed target experiments. In order to make predictions at such low values of x we can no longer use the LL(Q^2) approach of traditional QCD, but must solve the Lipatov equation instead [48].

In this chapter we present a numerical solution of the Lipatov equation in the low x region. We include in our evolution the possibility of gluon-gluon recombination and, moreover, vary the shadowing strength parameter $1/R$ over a range of values. These values are designed to represent saturation occurring either uniformly within the whole proton ("weak" shadowing), or concentrated within smaller "hot-spots" [60] located around the valence quarks ("strong" shadowing). The resulting transition region, which lies between perturbative and non-perturbative (Regge) physics, may be relevant to experiments at HERA. One of the advantages of our study is that it yields a possible indication of where in the (x, Q^2) plane this transition region lies. Its presence is signalled by the need to include higher-order terms in our perturbative (LL($1/x$)) approach.

We begin with the evolution in the form of the following non-linear integro-differential equation

$$x\frac{\partial f(x,k^2)}{\partial x} = \frac{3\alpha_s(k^2)}{\pi}k^2\int_{k_0^2}^{k_F^2}\frac{dk'^2}{k'^2}\left[\frac{f(x,k'^2)-f(x,k^2)}{|k'^2-k^2|}+\frac{f(x,k^2)}{(4k'^4+k^4)^{\frac{1}{2}}}\right] - \frac{81\alpha_s^2(k^2)}{16R^2k^2}[xg(x,k^2)]^2\,. \tag{6.1}$$

This is just the Gribov, Levin, Ryskin (GLR) equation [51] with suitable cut-offs imposed on the transverse momentum, k'. We expect the solution of this equation to demonstrate two different effects. Firstly, we expect the gluon to acquire a singular behaviour $x^{-\lambda}$ generated by the Lipatov kernel (specifically, we expect this behaviour to be controlled by the kernel's leading eigenvalue). Secondly, we expect the inclusion of recombination effects to dampen this rapid increase, producing distributions with a more acceptable small x behaviour. Notice that, unlike the Altarelli-Parisi equations, Eq. (6.1) is an evolution equation in x rather than Q^2. This means that its solution requires suitable boundary conditions, $f(x_0,k^2)$, to be imposed at some fixed $x=x_0$, rather than at some $Q^2=Q_0^2$. The choice of x_0 is rather important, we need to choose a value small enough so that a LL$(1/x)$ evolution down to lower values of x is valid. At the same time we require x_0 to be large enough so that we can derive the boundary conditions $f(x,k^2)$ from the available parton experimental data. In other words, we need x_0 to lie in the small region in which both the LL$(1/x)$ and LL(Q^2) approximations are valid. If we assume that such a choice is possible then we can proceed in the following manner: we take a set of parton distributions which have been determined from a global fit to experimental data and evolve them both upwards and downwards in Q^2 using the (leading-order) Altarelli-Parisi equations; the unintegrated gluon distribution $f(x,k^2)$ can then be taken directly from the gluon evolution equation

$$f(x,k^2) = \frac{\partial(xg(x,Q^2))}{\partial\ln(Q^2)} = q\otimes \mathrm{P}_{gq} + g\otimes \mathrm{P}_{gg} \tag{6.2}$$

where $\otimes$ denotes the standard convolution over the longitudinal momentum fraction, x. For our analysis we choose one of the $Q_0^2=4$ GeV^2 parametrizations of a recent analysis

by Kwiecinski, Martin, Roberts and Stirling (KMRS) [50]. One advantage of this choice is that we can compare our results with the corresponding KMRS gluons at small x. This is possible because KMRS extended their distributions down to $x = 10^{-5}$ with the aid of an approximate solution to the Lipatov equation. In what follows we shall use the KMRS B_0 set of parton distributions.

Once we have determined the boundary conditions $f(x_0, k^2)$ we can solve Eq. (6.1) to obtain $f(x, k^2)$ for $x < x_0$ and finally reconstruct the gluon distribution using

$$xg(x, Q^2) = \int_{\tilde{Q}_0^2}^{Q^2} \frac{\mathrm{d}k'^2}{k'^2} f(x, k'^2) \tag{6.3}$$

where the lower limit $\tilde{Q}_0^2$ is chosen to ensure the continuity of $g(x, Q^2)$ at $x = x_0$. We choose $\tilde{Q}_0^2 = 1$ GeV^2 for our analysis, although for precise continuity it should be very slightly above this value.

6.2 Results of the numerical evolution

6.2.1 The solutions

We take the boundary conditions generated from the KMRS B_0 distributions and evolve downwards in x with the evolution equation (6.1). Full details of the numerical method we use to perform this evolution can be found in Appendix B. The resulting solution for $xg(x, Q^2)$ is shown in Fig. 6.1 for two different values of Q^2 ($Q^2 = 4$ GeV^2 and $Q^2 = 100$ GeV^2 respectively). The top curve shows the small x behaviour of the gluon when shadowing is neglected, and the lower curves show the effect of the shadowing contribution assuming first $R = 5$ GeV^{-1} and, second, the more extreme "hot-spot" example with $R = 2$ GeV^{-1}. As was mentioned earlier the approximations we are using

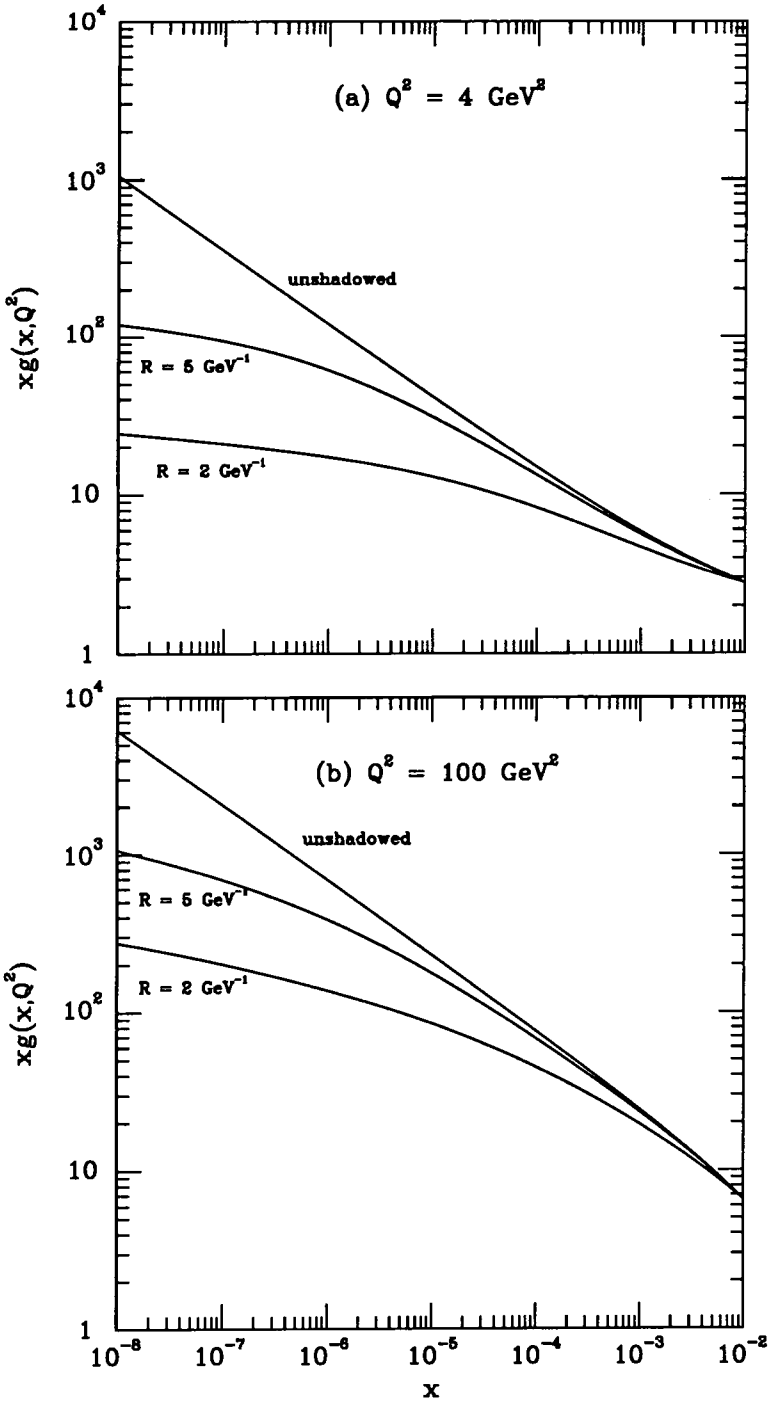

Figure 6.1. The values of $xg(x,Q^2)$ at (a) Q^2= 4 GeV^2 and (b) Q^2= 100 GeV^2 calculated from the solution $f(x,k^2)$ of the integro-differential Lipatov equations [Eqs. (6.1) and (6.3)] with the boundary conditions, $f(x_0,k^2)$, at $x_0 = 10^{-2}$ fixed as described in the text. In each figure the three curves are, in descending order, the solution with shadowing neglected and the solutions with the shadowing term included with $R = 5$ GeV^{-1} and $R = 2$ GeV^{-1}. The validity of the leading-order shadowing approximation at ultra-small x is studied in Fig. 6.2

are expected to break down at very small x and so although the curves of Fig. 6.1 continue down to $x = 10^{-8}$ we do not expect them to be correct in this region. We shall examine the region of validity of the calculations in the next section.

The results for the unshadowed gluon clearly show the $x^{-\lambda}$ behaviour, expected from the Lipatov effect, with a value of $\lambda = 0.47$ (in the small x limit). This value of λ is remarkably stable to evolution in Q^2, although it does depend on the infra-red cut-off, k_0^2. As we saw earlier this dependence takes the form $\lambda \sim \alpha_s(k_0^2)$. For example, if we were to take $k_0^2 = 2$ or 4 GeV^2 then we would find that $\lambda = 0.42$ or 0.37 respectively, in the small-x limit of the unshadowed gluon.

The small x dependence of the gluon shown in Fig. 6.1 has important implications for future *ep* colliders. In the region $x \sim 10^{-4}$ probed by HERA, for example, it is clear that the $R = 5$ GeV^{-1} shadowed case is little different from the unshadowed case. Given that HERA will be unable to probe down to smaller values of x, it seems unlikely that the machine will be able to detect weak shadowing. Indeed, our results suggest that it will be quite difficult to distinguish strong shadowing, given the normalization uncertainties present. Ideally, we need to probe down to $x \sim 10^{-5}$ or even 10^{-6}, where the gluon distribution is clearly flattening off. Unfortunately, measurements at such small values of x are beyond the range of foreseeable experiments. Of course, there is still the possibility that higher-order corrections are important and they may cause the gluon distribution to flatten out at higher values of x.

6.2.2 How important are the higher-order corrections?

As we have often pointed out, the approximations that we are using are not expected to be valid at ultra-small x. The recombination term which we introduced into Eq. (6.1) is only the first of many recombination terms that exist. At smaller and smaller values of

x these other (as yet uncalculated) terms become more and more important. Eventually we will reach the non-perturbative Regge limit. In order to determine the region where our approximations are valid we introduce a parameter W' which is defined as the ratio of the first (quadratic) shadowing term to the (linear) Lipatov term.

$$W' = \frac{\text{shadowing term}}{\text{Lipatov term}} \tag{6.4}$$

As long as this term remains of order α_s then we expect that the higher terms can be safely neglected. However, as we go to smaller values of x, W' will increase, reflecting the growth in importance of the recombination terms in the evolution equation. This behaviour is demonstrated in Fig. 6.2. As anticipated from the α_s^2 dependence of the recombination term, the approximation improves dramatically with increasing Q^2.

If we use the criterion that $W'(x,Q^2) \lesssim \alpha_s(Q^2)$ then we see from Fig. 6.2 that for $R = 5$ GeV^{-1} the leading-order shadowing contribution should be a reasonable approximation for $x \gtrsim 10^{-5}$—even at low Q^2. Thus, provided that the shadowing is weak, HERA is unlikely to probe the region where higher-order recombination terms are important. This agrees with the results of the previous section where we saw that the effect of weak shadowing on the gluon distribution was not noticeable in the HERA region. Alternatively, if the shadowing is stronger ($R = 2$ GeV^{-1}) then we find—not surprisingly—that the breakdown of the approximation is much faster. For low values of Q^2 ($Q^2 \sim 10$ GeV^2) we see from Fig. 6.2 that we cannot rely on our numerical solution much below $x \sim 10^{-3}$. This means that, for "strong" shadowing, the region where higher-order terms are important is accessible to HERA. In the previous section our results (with only leading-order corrections present) suggested that it would be quite difficult to observe shadowing effects at HERA. Now, however, we see that, for strong shadowing, we should take higher-order contributions into account. These extra recombination diagrams will flatten the distribution away from the $x^{-\lambda}$ behaviour faster than the case with only a leading-order term present. It is still possible, therefore, that strongly-shadowed gluon distributions will be observed at HERA.

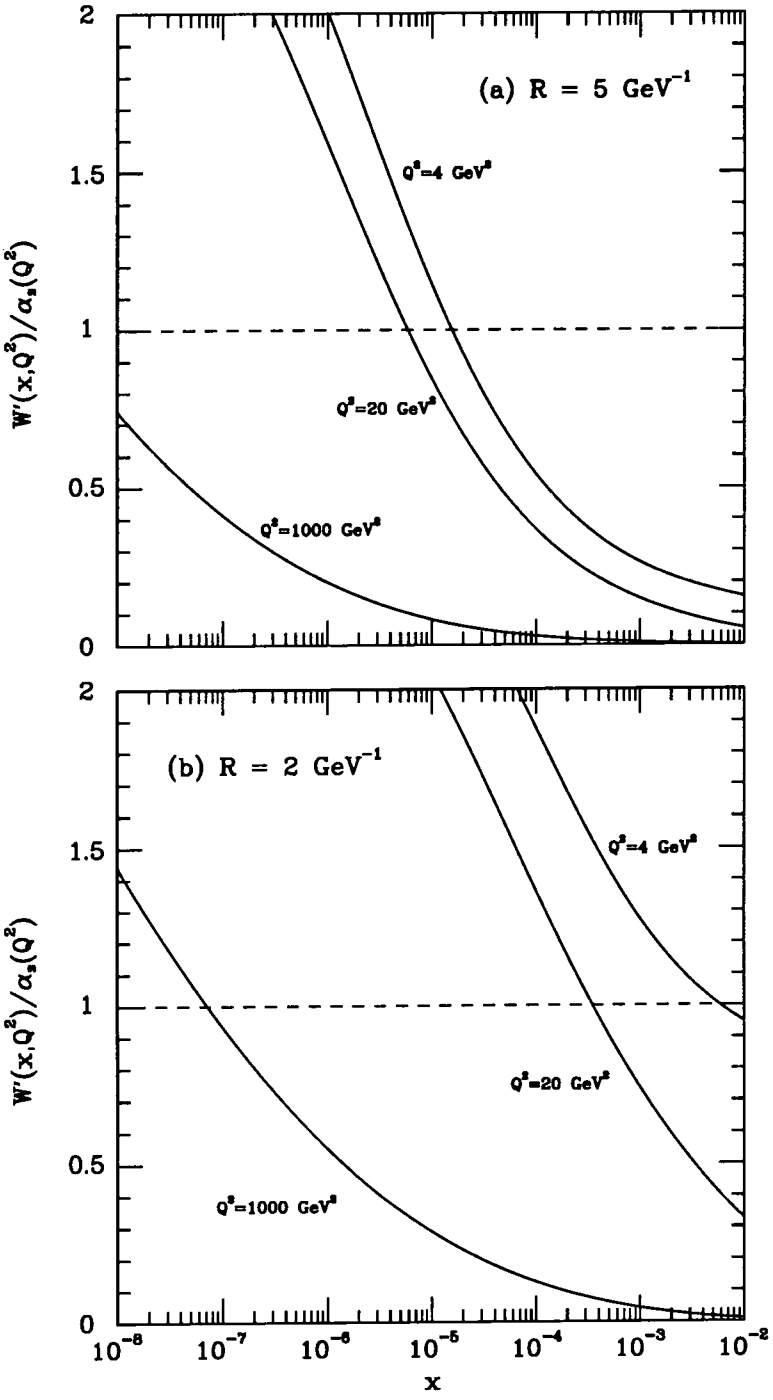

Figure 6.2. The values of $W'(x,Q^2)/\alpha_s(Q^2)$ which correspond to the solutions of the Lipatov equation (6.1) with (a) "weak" ($R = 5$ GeV^{-1}) and (b) "strong" ($R = 2$ GeV^{-1}) shadowing. The solutions are only expected to be valid below the dashed line which represents $W'(x,Q^2)/\alpha_s(Q^2) = 1$.

6.3 Comparison with other approximations

The Lipatov equation is not the only way of calculating the gluon's small x behaviour. There are several other (usually less accurate) ways of doing so. In this section we compare our numerical solutions of the Lipatov equation with these approximations in order to gain some feeling for how well they perform. We begin with the DLLA.

6.3.1 The DLLA

As we saw in the previous chapter, the DLLA keeps only those terms in the perturbative expansion which contain large logarithms of both $1/x$ and Q^2. Obtaining the resulting gluon distribution is straightforward. We merely replace the Lipatov kernel in Eq. (6.1) with the strongly ordered kernel

$$K(k_T, k'_T) = \frac{3\alpha_s}{\pi} \frac{1}{k_T^2} \theta(k_T^2 - k'^2_T) \tag{6.5}$$

resulting in an evolution equation of the form

$$\frac{\partial f(x,k^2)}{\partial \ln(1/x)} = \frac{3\alpha_s(k^2)}{\pi} xg(x,k^2) - \frac{81\alpha_s^2(k^2)}{16R^2k^2}[xg(x,k^2)]^2 \tag{6.6}$$

The boundary conditions for this equation are the same as for the Lipatov evolution. Figure 6.3 compares our solution of the Lipatov equation with the solution of the corresponding DLLA evolution equation. Notice that the unshadowed Lipatov solution is much steeper than the unshadowed DLLA solution.

The results of Fig. 6.3 show that on its own the DLLA is not very good at determining the small x behaviour of the gluon. It is simply not capable of generating the singular effects expected from a full treatment of the $\log(1/x)$ terms. One can, however adopt a different procedure which relies on the fact that the singular behaviour of the Lipatov solution is stable to evolution in Q^2.

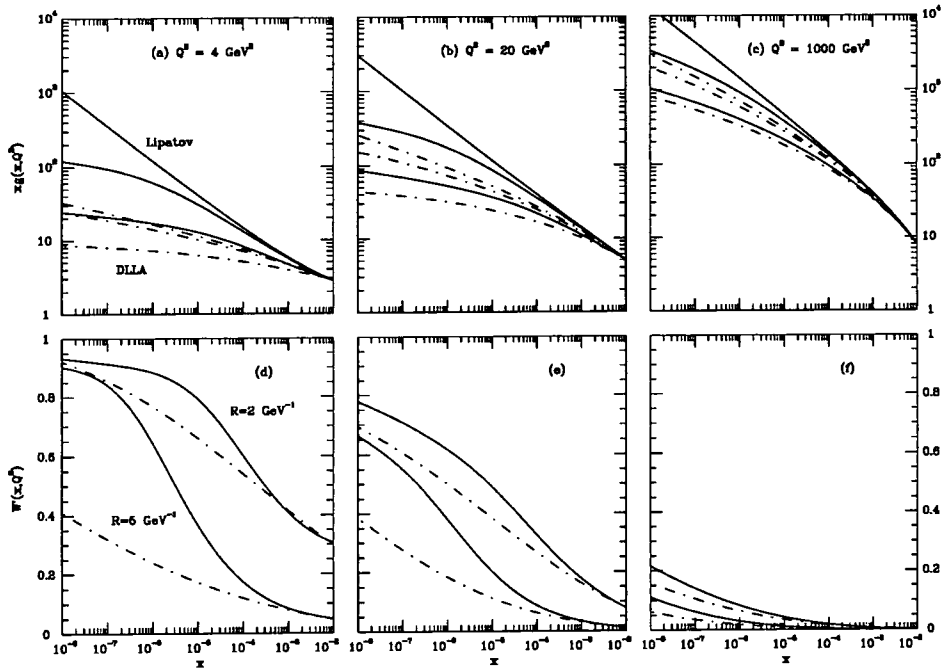

Figure 6.3. (a)-(c): the continuous curves are the values of $xg(x, Q^2)$ determined from the Lipatov equation (exactly as in Fig. 6.1) for Q^2=4, 20 and 1000 GeV^2 respectively. The dot-dashed curves are the values obtained by replacing the Lipatov kernel with the DLLA expression given in Eq. (6.5). (d)-(f) show the values of W', calculated as in Eq. (6.4), which correspond to solutions with shadowing that are shown in (a)-(c) respectively. The upper (lower) two curves correspond to the Lipatov and DLLA solutions with $R = 2$ GeV^{-1} ($R = 5$ GeV^{-1}). The shadowing corrections are only reliable if $W' \lesssim \alpha_s(Q^2)$.

If we start our DLLA evolution from a solution which already contains the Lipatov shape then we find very good agreement between the two solutions. The curves of Fig. 6.4 are evolved from an input distribution, $xg(x, Q^2 = 4\ \text{GeV}^2)$, obtained from Lipatov evolution (Fig. 6.1). The equation which defines the gluon distribution is now

$$xg(x,Q^2) = xg_{\text{Lip}}(x, Q_i^2 = 4\ \text{GeV}^2) + \int_{Q_i^2}^{Q^2} \frac{\mathrm{d}k^2}{k^2}\, f(x,k^2) \tag{6.7}$$

with

$$xg_{\text{Lip}}(x,Q^2) = \int_{\tilde{Q}_0^2}^{Q^2} \frac{\mathrm{d}k^2}{k^2}\, f_{\text{Lip}}(x,k^2) \tag{6.8}$$

as in Eq. (6.3). With this definition of the gluon we can once again use the evolution equation (6.6), except that now we generate the distributions of Fig. 6.4 rather than the distributions of Fig. 6.3. The agreement in shape between the new DLLA evolution and the Lipatov evolution is remarkable, both are faster than the LL(Q^2) evolution, however, as we shall see in the next section.

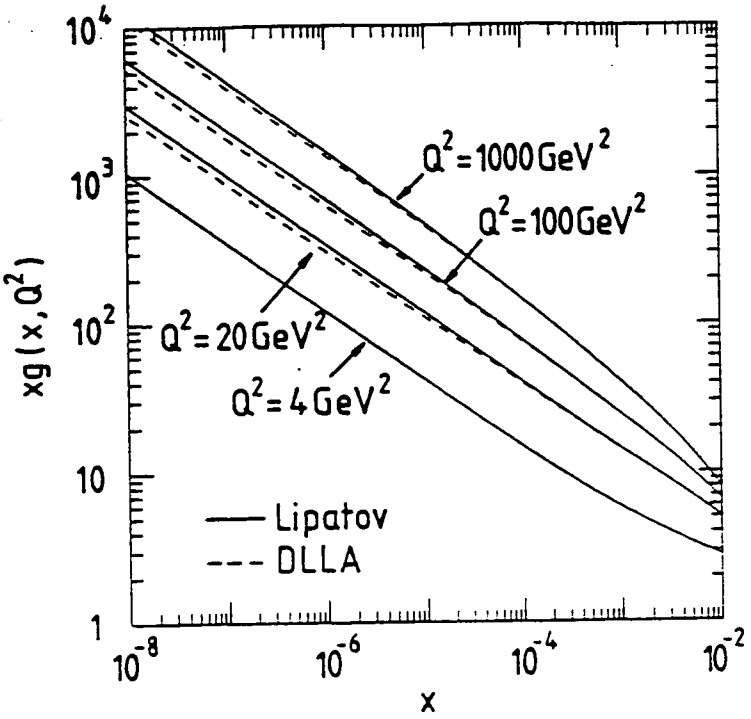

Figure 6.4. A comparison of the Q^2 evolution generated by the Lipatov equation (continuous curves) with that obtained in the DLLA of Eqs. (6.7) and (6.8) (dashed curves)

6.3.2 Altarelli-Parisi evolution and the KMRS analysis

Although the standard Altarelli-Parisi evolution equations are not expected to work in the small x region, it is, nevertheless, interesting to compare the predictions obtained with those of the Lipatov evolution. We have already seen that inclusion of the small x

Lipatov shape into the DLLA evolution can generate a very good approximation for all Q^2. This was due to the stability of λ to evolution in Q^2. We anticipate, therefore, that an Altarelli-Parisi evolution from a starting distribution which includes an $x^{-\lambda}$ behaviour at small x, should also be a good approximation. This was the approach adopted by Kwiecinski, Martin, Roberts and Stirling (KMRS) in their global analysis of parton data [50]. Although the shape of the gluon distribution at large x is constrained by the data, they were able to modify the shape at small x to imitate the behaviour of both shadowed and unshadowed gluons. The unshadowed gluon distribution, xg^u, was assumed to take the form

$$xg^u(x,Q_0^2) \simeq C(x)x^{-\lambda}\,, \tag{6.9}$$

where $\lambda \simeq 1/2$. This distribution was evolved upwards using the (next-to-leading order) Altarelli-Parisi equations, and preserved the Lipatov-like shape. For the shadowed gluon they modified xg below $x_0 = 10^{-2}$ to have the form

$$xg(x,Q_0^2) \;=\; \frac{xg^u(x,Q_0^2)}{[1+\theta(x_0-x)(C(x)x^{-1/2}-C(x_0)x_0^{-1/2})/xg_{\rm sat}(x,Q_0^2)]} \tag{6.10}$$

where, if the (leading-order) shadowing correction continued to be valid as $x \to 0$, then $xg_{\rm sat}$ would be the saturation limit of the gluon distribution. $xg_{\rm sat}$ is defined to be the gluon distribution which makes the right-hand side of the evolution equation (6.6) identically zero in the DLLA at very small x. That is

$$\frac{3\alpha_s}{\pi}xg_{sat} \;=\; \frac{81\alpha_s^2}{16R^2Q^2}(xg_{\rm sat})^2 \tag{6.11}$$

which gives

$$xg_{sat}(x,Q^2) \;=\; \frac{16R^2Q^2}{27\pi\alpha_s(Q^2)}\,. \tag{6.12}$$

The shadowed ($R = 5$ and $R = 2$ GeV^{-1}) gluons were evolved upwards with the Altarelli-Parisi equations modified to include a shadowing term

$$Q^2\frac{\partial(xg(x,Q^2))}{\partial Q^2} \;=\; {\rm P}_{gg}\otimes g \;+\; {\rm P}_{gq}\otimes q - \frac{81\alpha_s^2(k^2)}{16R^2k^2}[xg(x,k^2)]^2\,. \tag{6.13}$$

Figure 6.5 shows a comparison of our numerical solution with the B_- set of KMRS partons (dashed curves) at four different values of Q^2 (Q^2 = 4, 20, 100 and 1000 GeV^2). Some general trends are apparent. For the KMRS gluons we see that the $x^{-\lambda}$ behaviour sets in a little more rapidly, with decreasing x, and that the shadowing effects at low Q^2 are somewhat larger than those of our numerical solutions. Most important of all, however, is the rate of evolution with Q^2. Figure 6.5 shows that the Lipatov evolution is faster than the corresponding LL(Q^2) evolution. This can be traced to the treatment of the gluon splitting function, P_{gg}, by both approximations. In the LL(Q^2) approach the gluon splitting function takes the form

$$P_{gg}(z) = 2N_c\left[\frac{z}{(1-z)_+} + \frac{(1-z)}{z} + z(1-z)\right] + \frac{\beta_0}{2z}\delta(1-z) \tag{6.14}$$

However, the DLLA and Lipatov equations both use the approximation that $x_j \ll x_{j-1}$ and, consequently, $z \equiv x_j/x_{j-1} \ll 1$. With this assumption the splitting function P_{gg} is approximated by

$$P_{gg}(z) \simeq \frac{2N_c}{z} \tag{6.15}$$

which has the effect of increasing the rate of evolution in Q^2.

With our present limited knowledge, the results we have seen so far suggest a procedure to obtain the 'best' solution for the small x gluon distribution. We should begin by solving the Lipatov equation at small x and low Q^2 ($\sim$ 5 GeV^2) and then evolve upwards using the Altarelli-Parisi equations. This will not only preserve the correct small x behaviour, but will also generate the correct Q^2 dependence.

6.3.3 The semi-classical approximation

The last case that we shall consider is the semi-classical approximation [61]. This is traditionally formulated as an approximation of the DLLA, although, more recently, there

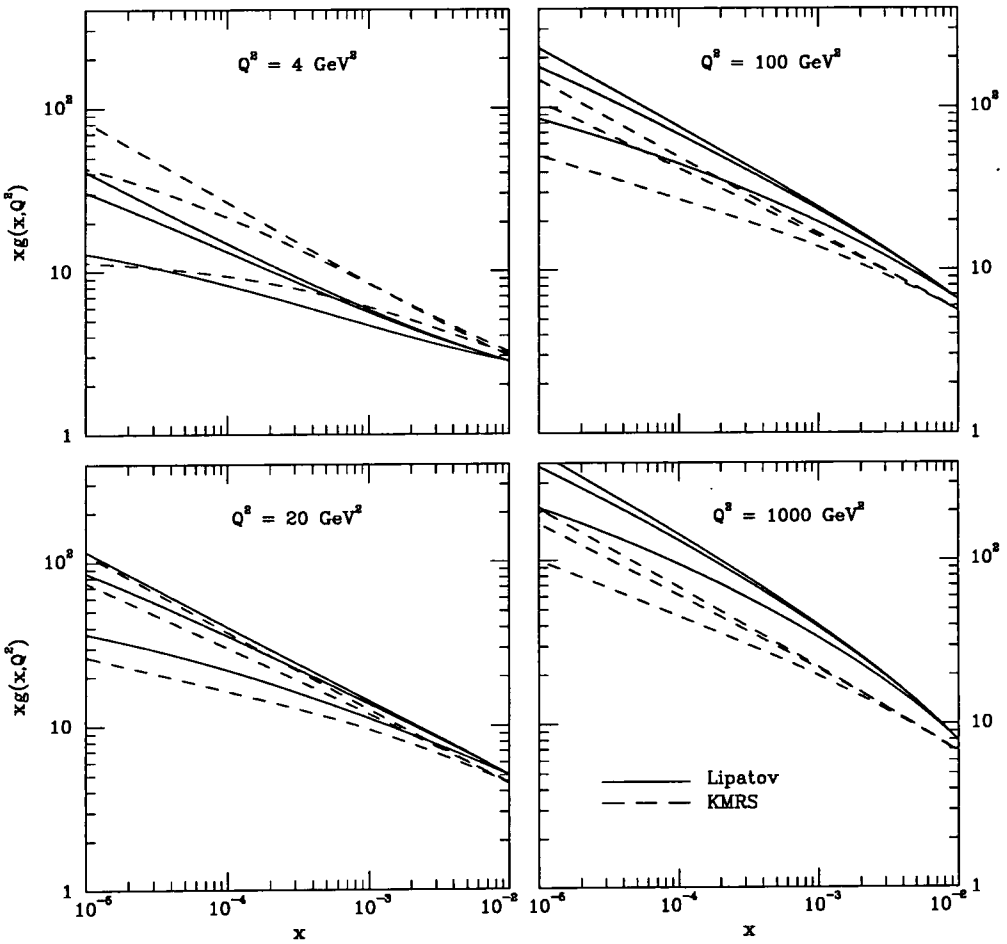

Figure 6.5. The continuous curves are the values of $xg(x, Q^2)$ determined by solving the Lipatov equation (exactly as in Fig. 6.1) for Q^2 = 4, 20, 100, 1000 GeV^2. The dashed curves are $xg(x, Q^2)$ of set B_- of the KMRS [50] next-to-leading order parton distribution analysis (with and without shadowing). The small difference at $x = 10^{-2}$ arises because the input, $g(x_0, Q^2)$, to the Lipatov equation was determined by evolving up and down in Q^2 starting from $g(x, Q^2 = 4\ \text{GeV}^2)$ of set B_0 of KMRS using the leading-order Altarelli-Parisi equation.

has been a semi-classical formulation of the Lipatov equation itself [62]. We shall examine the former case as we would like to investigate some claims made about the properties of the so-called "critical line" which exists within this approach. Recall that the DLLA (with shadowing terms added) is written as

$$\frac{\partial f(x,k^2)}{\partial \ln(1/x)} = \frac{3\alpha_s(k^2)}{\pi} xg(x,k^2) - \frac{81\alpha_s^2(k^2)}{16R^2k^2}[xg(x,k^2)]^2 \tag{6.16}$$

If we introduce the variables $y \equiv \ln(1/x)$ and $\xi \equiv \ln(\ln(Q^2/\Lambda^2))$ then we can re-write this equation as

$$G_{y\xi} = cG - \lambda \exp(-\xi - e^{\xi})G^2 \tag{6.17}$$

where $G(y,\xi) \equiv xg(x,Q^2)$ and

$$c = \frac{12}{11 - 2n_f/3} \quad , \quad \lambda = \frac{9\pi^2 c^2}{16R^2\Lambda^2} \, . \tag{6.18}$$

If we substitute $e^S \equiv G$ into Eq. (6.17) then it can be written as

$$S_y S_\xi + S_{y\xi} = c - \lambda \exp(-\xi - e^{\xi} + S) \, . \tag{6.19}$$

We now apply the semi-classical approximation which consists of neglecting the second-order derivatives and keeping only the first-order derivatives. It is based on the assumption that

$$S_y S_\xi \gg S_{y\xi} \, . \tag{6.20}$$

Applying this to Eq. (6.19) we obtain

$$S_y S_\xi = c - \lambda \exp(-\xi - e^{\xi} + S) \, . \tag{6.21}$$

We thus have an evolution equation which depends only on the first-order derivatives of $S(y,\xi) \equiv \ln[G(y,\xi)]$. This is an equation of the general form

$$F(p,q,\xi,y,S) = 0 \tag{6.22}$$

where $p \equiv S_\xi$, $q \equiv S_y$, and so may be solved by the method of characteristics [63]. We have

$$F = pq - c + \lambda \exp(-\xi - e^\xi + S) = 0 \tag{6.23}$$

and the characteristic equations

$$\frac{\mathrm{d}y(\xi)}{\mathrm{d}\xi} = \frac{p(\xi)}{q(\xi)}\,, \tag{6.24}$$

$$\frac{\mathrm{d}S(\xi)}{\mathrm{d}\xi} = 2p(\xi)\,, \tag{6.25}$$

$$\frac{\mathrm{d}p(\xi)}{\mathrm{d}\xi} = \frac{-\lambda \exp[-\xi - e^\xi + S(\xi)][-1 - e^\xi + p(\xi)]}{q(\xi)}\,, \tag{6.26}$$

$$\frac{\mathrm{d}q(\xi)}{\mathrm{d}\xi} = -\lambda \exp[-\xi - e^\xi + S(\xi)]\,. \tag{6.27}$$

If we are given an input distribution S at $\xi = \xi_0$ we can solve this set of equations and obtain a family of characteristic curves $y(\xi)$ in the (y, ξ) plane. Each of these curves originates from a unique starting point (y, ξ_0). Amongst this family there exists one particular characteristic curve known as "the critical line" which divides the remainder into two distinct classes depending on whether they lie above or below the critical line. On one side the curves tend to flatten out into straight lines, so that $y(\xi)$ increases only slowly with ξ. On the other side of the line, however, the characteristic curves increase rapidly with ξ tending to infinity at some finite value of ξ. Both classes of curve are illustrated in Fig. 6.6 relative to the critical line.

What is the physical interpretation for these two very different types of behaviour? Consider first the curves which lie below the critical line. Their tendency to flatten out and become straight lines indicates that the gradient of Eq. (6.24) eventually becomes a constant. This is achieved by setting $\lambda = 0$ in Eqs. (6.26) and (6.27), and corresponds physically to neglecting recombination effects (as can be seen from the definition of λ (Eq. 6.18)). Now consider the curves which rapidly tend to infinity at finite values of ξ. The gradient of $y(\xi)$ grows rapidly as the function increases and from Eq. (6.24) we see

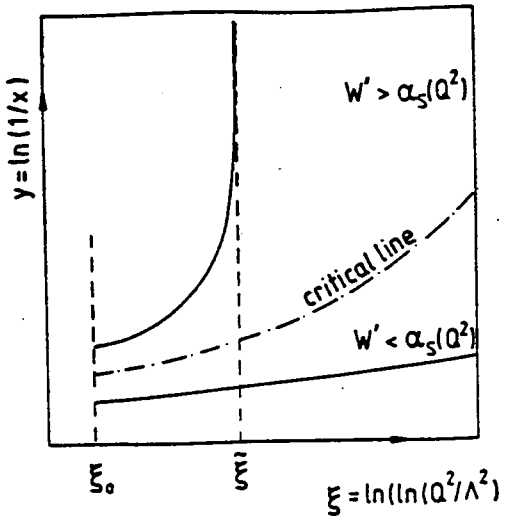

Figure 6.6. A sketch of the characteristic curves, $y(\xi)$, obtained by solving the semi-classical system of equations [Eqs. (6.23) and (6.24)-(6.27)], using input $S(y,\xi)$ at $\xi = \xi_0$. In this approximation the gluon packing fraction, $W' \simeq \alpha_s(Q^2)$ on the critical line. In regions where shadowing is negligible the characteristic curves are straight lines.

that $q(\xi)$ must be tending to zero. As q is just S_y this corresponds to the flattening of the gluon distribution in x, that is to say, $q = 0$ corresponds to the saturation limit. At large ξ the critical line solution behaves as

$$y_c(\xi) \to \frac{1}{8c} e^{2\xi} \tag{6.28}$$

and the value of the saturation parameter W' evaluated on this line is then

$$W' \simeq \alpha_s(Q^2) \tag{6.29}$$

for large ξ. The proof is as follows. W' is the ratio of the second and first terms on the right-hand side of Eq. (6.21)

$$W' = \frac{\lambda}{c} \exp[-\xi - e^{\xi} + S(\xi)] \,. \tag{6.30}$$

The behaviour of S on the critical line for large ξ is

$$S(\xi) = e^{\xi} + \ln(2c/\lambda) \tag{6.31}$$

and so

$$W_c' = 2e^{-\xi} = \frac{2}{\ln(Q^2/\Lambda^2)} = \frac{6}{\pi c}\alpha_s(Q^2) \tag{6.32}$$

for large ξ.

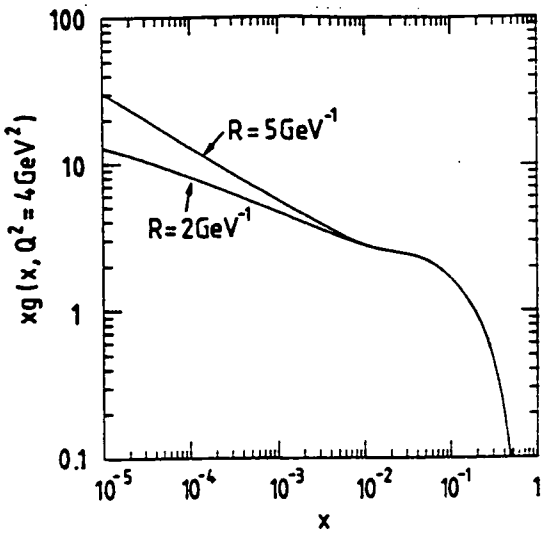

Figure 6.7. The gluon distribution at $Q^2 = 4$ GeV^2 used to give the starting values for the characteristic curves shown in Fig. 6.8. For $x > x_0 = 10^{-2}$ it corresponds to the gluon of set B_0 of KMRS [50] and for $x < x_0$ it is the distribution generated by the Lipatov equation with the shadowing term included (with either $R = 5$ or 2 GeV^{-1}).

Figure 6.8 shows the families of characteristic curves obtained from solving Eqs. (6.23) and (6.24)-(6.27) using the input gluon distributions $xg(x, Q^2)$ of Fig. 6.7 which correspond to shadowing with $R = 5$ and 2 GeV^{-1} in Eq. (6.18). The dot-dashed curves represent characteristics above the critical line which eventually behave as $y(\xi) \to \infty$ for some $\xi = \xi_c$. However, the division of the characteristics by the critical line is not immediately evident from the behaviour shown in Fig. 6.8. In fact, to determine where the separation actually occurs, we redraw the characteristic curves on a $(\ln y, \xi)$ plot, as shown in Fig. 6.9. On this plot the critical curve may be readily identified as a straight line of slope 2 at large ξ as expected from Eq. (6.28).

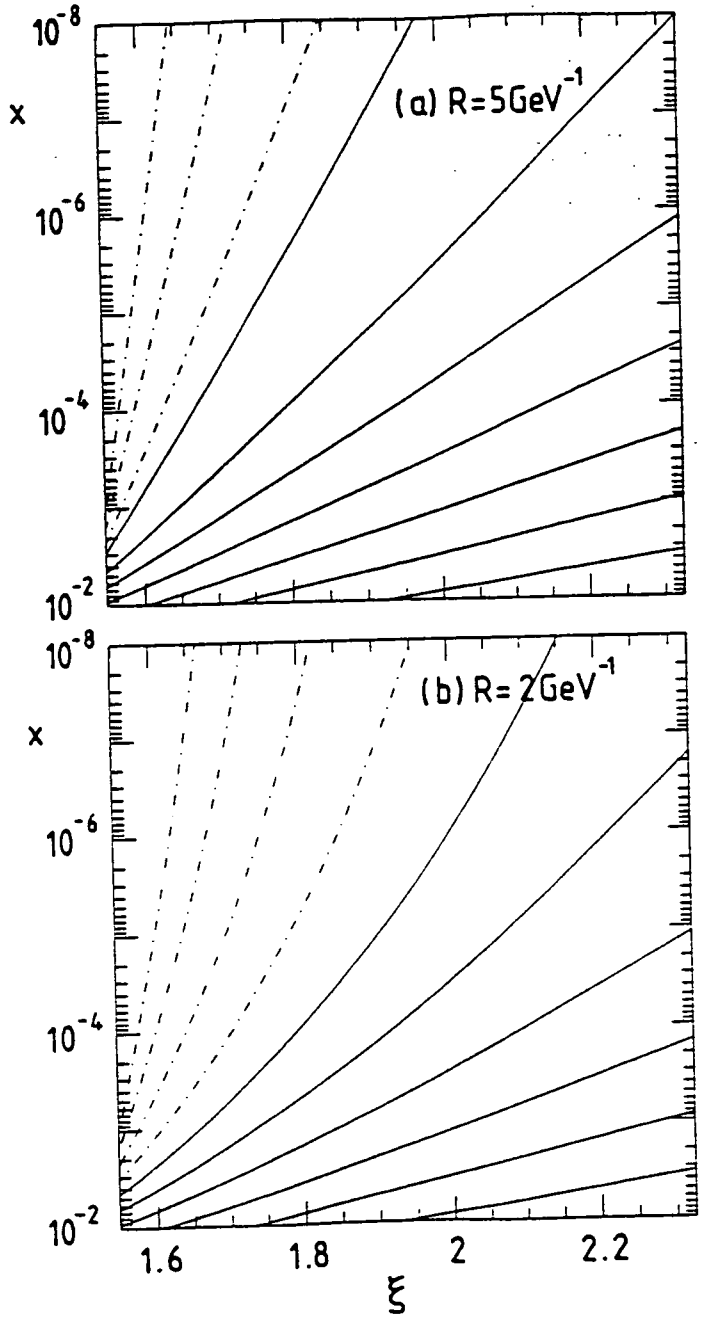

Figure 6.8. The characteristic curves, $y(\xi)$, obtained by solving the semi-classical equations 6.23 and 6.24-6.27 using the gluon distribution of Fig. 6.7 at $Q^2 = 4$ GeV^2 as input, where $\xi = \ln(\ln(Q^2))$ and $y = \ln(1/x)$. We show the families of characteristics for (a) the conventional choice of the shadowing radius, $R = 5$ GeV^{-1}, and (b) "hot-spot" shadowing with $R = 2$ GeV^{-1}. The dot-dashed curves correspond to characteristics above the critical line.

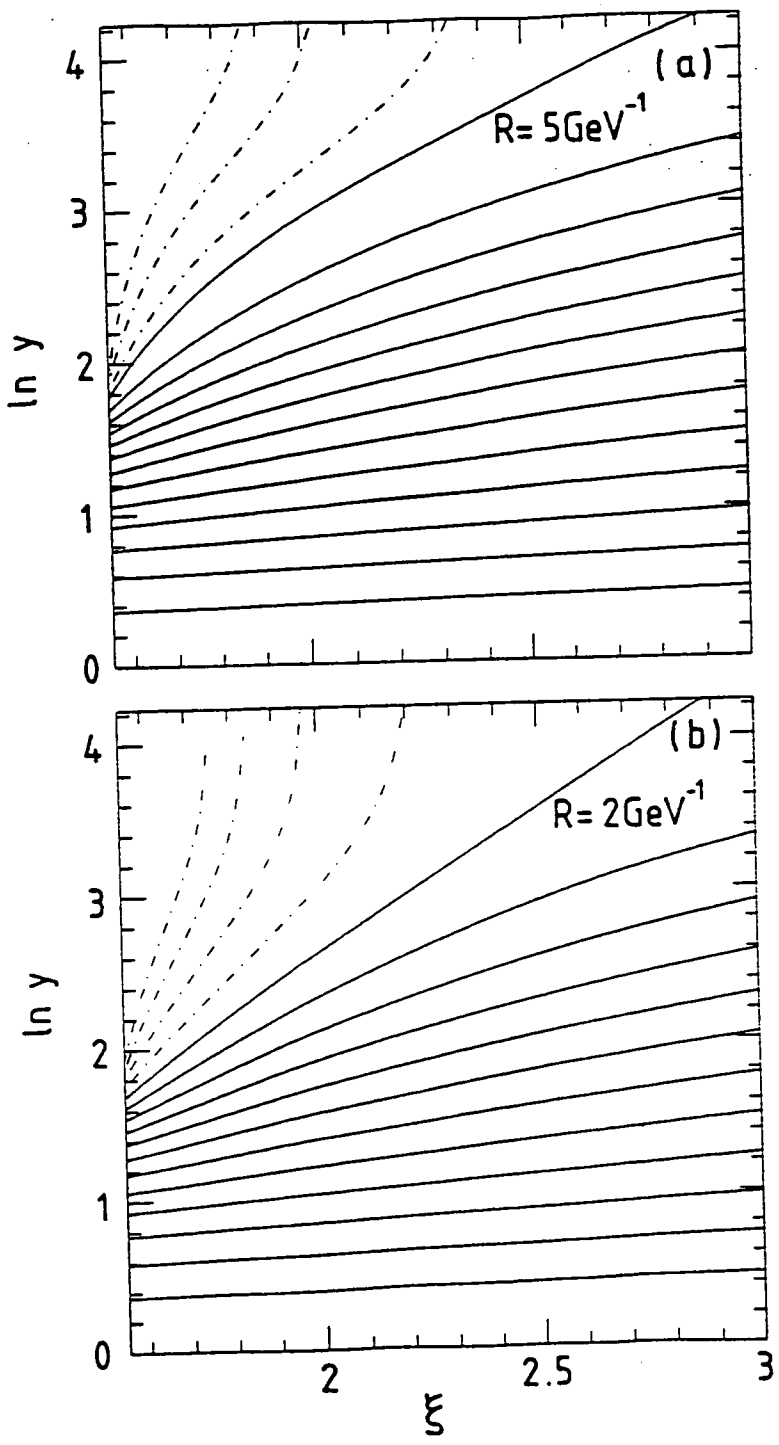

Figure 6.9. The characteristic curves of Fig. 6.8 redrawn on a (ln y,ξ) plot. On this plot the critical curve behaves at large ξ as a straight line of slope 2, [see Eq. (6.31)]. The dot-dashed characteristic curves above the critical line are now very evident.

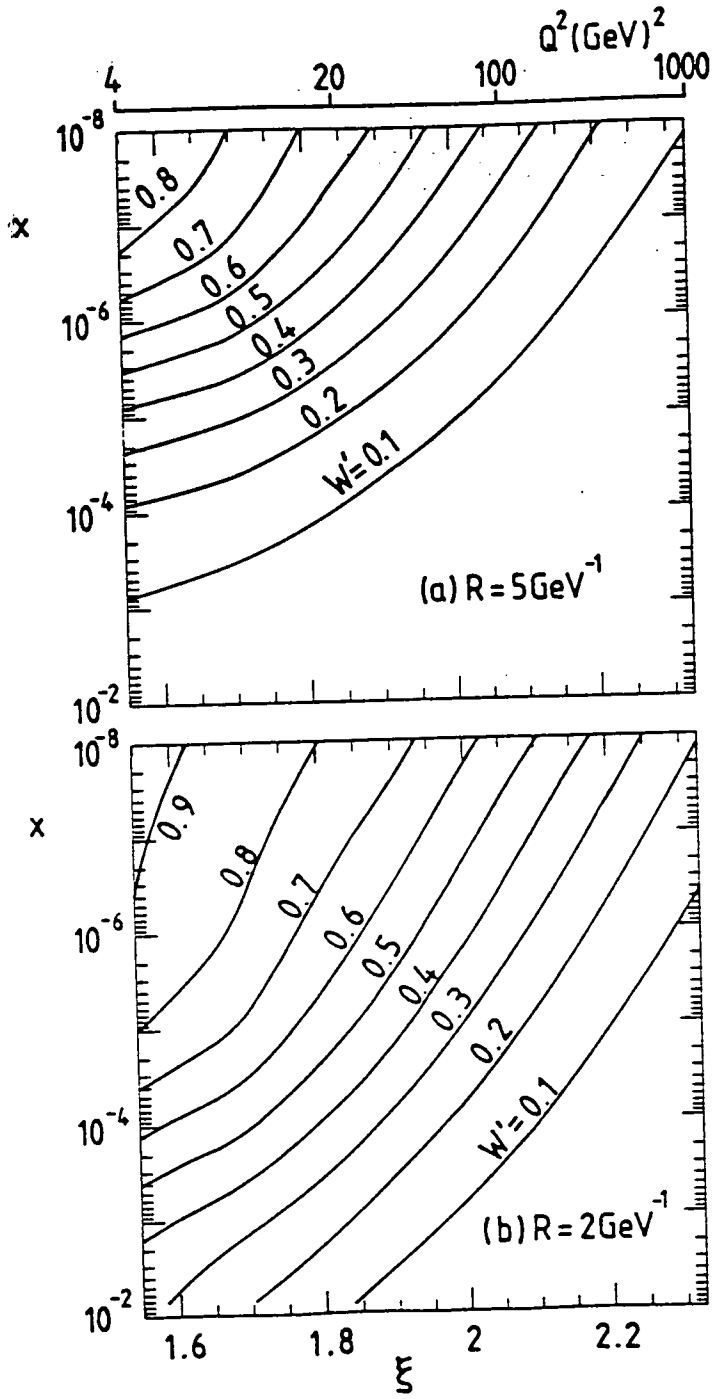

Figure 6.10. Contour plots of constant W' in the (y,ξ) plane, where $y = \ln(1/x)$ and $\xi = \ln(\ln(Q^2))$, obtained from solving the (exact) Lipatov equation with shadowing included with (a) $R = 5\ \mathrm{GeV}^{-1}$ and (b) $R = 2\ \mathrm{GeV}^{-1}$, as described in the text. The leading-order shadowing approximation should be valid in the domain satisfying $W' \lesssim \alpha_s(Q^2)$.

It should now be clear just why the critical line has often been regarded as the division between the "low-density gluon" region of perturbative QCD and the "high-density gluon" region where saturation occurs and perturbation theory breaks down. Remember, however, that the semi-classical approximation is based on the DLLA which is itself an approximation of the Lipatov equation. We should feel rather uneasy about any precise predictions based on its solution. In order to test the predictions of the semi-classical model we plot the critical line produced by our boundary conditions (Fig. 6.7) together with contours of W' which are obtained from our exact numerical solution to the Lipatov equation. The results are shown in Fig. 6.10.

We can see from Fig. 6.10 that, in the region of the (y, ξ) plane probed by HERA, the critical line is not a good indicator of where higher-order shadowing effects should become important. The value of W' can still be small in the region lying above the critical line. We thus conclude that the semi-classical approximation is too crude an approximation to have any real predictive power at non-asymptotic values of ξ.

6.4 Summary

In this chapter we have presented the results of a numerical solution of the Lipatov evolution equation. These results show a gluon distribution with the predicted $x^{-\lambda}$ small x behaviour as well as distributions in which this growth is slowed by the leading-order shadowing contributions. We have used the relative size of the linear and non-linear terms in the evolution equation as an indication of the importance of the (uncalculated) higher-order terms. When this ratio exceeds $\alpha_s(Q^2)$ we note that higher-order contributions should be included in the evolution. We have also found that, for HERA values of x and Q^2, the unshadowed and weakly shadowed ($R = 5$ GeV^{-1}) gluons are almost indistinguishable,

whilst for the strongly shadowed case ($R = 2$ GeV^{-1}) we have seen that the higher-order terms may be important, at least at the lower values of Q^2. This may make it possible to observe the effects of shadowing at HERA.

A comparison of possible evolutions shows that only the LL($1/x$)A is capable of producing the correct small x behaviour, but that this behaviour is stable to Q^2 evolution in all three methods (DLLA, LL(Q^2)A and LL($1/x$)A). The Q^2 evolution of the DLLA and the LL($1/x$)A is faster than that of the LL(Q^2)A and we note that this was due to an approximation of the gluon splitting function P_{gg}. We have argued that, at present, the best way to generate the correct Q^2 behaviour is to apply the Altarelli-Parisi equations to a distribution which possess the correct small x behaviour. Finally, we have examined the semi-classical approximation and the importance of the "critical line" which occurs in its solution. Although this line has been considered a boundary between perturbative and non-perturbative physics, we have seen that it is not very dependable at non-asymptotic values of Q^2.

7 Deep-inelastic events containing a measured jet as a probe of QCD behaviour at small x

7.1 Introduction

So far experiments have not been able to probe down to small enough values of x (at least for Q^2 large enough to be in the perturbative region) for the behaviour predicted by the Lipatov equation to set in. As a result, there has been no confirmation of the existence of the Lipatov (or QCD) pomeron. Measurements of the deep-inelastic structure functions $F_L(x,Q^2)$ and $F_2(x,Q^2)$ at HERA can probe $g(x,Q^2)$ and $\bar{q}(x,Q^2)$ respectively in this region of low x, but over a limited range of Q^2 [64, 59]. The comparison of the experimentally-determined parton distributions with the QCD predictions is complicated by the need to input some "starting" parton distributions (such as their x behaviour at $Q_0^2 = 4$ GeV^2) in the QCD calculation. Thus if a steep behaviour were to be observed at small x (such as in Eq. (5.26)) which, most reasonably, could be taken to indicate the existence of the Lipatov pomeron, there is always the possibility that the effect could be of non-perturbative origin. A study of the Q^2 dependence would appear to be of little help. The steep behaviour with decreasing x that is generated by the Lipatov equation is stable to evolution in Q^2. Moreover, we have seen that the Q^2 dependence arising from the Lipatov equation is similar to that of the DLLA evolution equation. Finally, only a limited range of Q^2 is accessible at HERA, for small values of x, so the evolution length $\ln(Q^2_{max}/Q^2_{min})$ is small (recall that Q^2_{min} has to be large enough for perturbative QCD to be valid).

It is clearly desirable to look for experiments which focus on the small-x behaviour of QCD (rather than its Q^2 behaviour) and which, unlike the deep-inelastic F_L and F_2 structure function measurements, do not depend on assuming some input x distribution. An intriguing proposal has been made by Mueller [65]. The idea is to study deep-inelastic (x, Q^2) events which contain an identified jet (x_j, k_{1T}^2) where $x \ll x_j$ and $Q^2 \simeq k_{1T}^2$. The process is illustrated in Fig. 7.1 where the jet arises from parton a (which can be either a quark or a gluon). The longitudinal momentum fraction x_j carried by the jet is chosen not to lie in the small-x region and the strong-ordering of transverse momenta at the gluon-a vertex ($k_{0T}^2 \ll k_{1T}^2$) means that the exchanged gluon and the jet have approximately the same transverse momentum, as shown in Fig. 7.1. Since we choose events with $k_{1T}^2 \simeq Q^2$ the Q^2 evolution is neutralised and attention is focused on the small-x, or rather the small-x/x_j, behaviour.

It is convenient to express the rate (or cross section) of deep-inelastic events containing an identified jet as a differential structure function in terms of the jet variables, $\partial F_2/\partial x_j \partial k_{1T}^2$. Recalling that the Lipatov sum of the gluon emissions gave the behaviour shown in Eq. (5.26), we would expect the deep-inelastic + jet events arising from Fig. 7.1 to have the form

$$x_j k_{1T}^2 \frac{\partial F_2}{\partial x_j \partial k_{1T}^2} \sim \alpha_s(k_{1T}^2) \left[x_j \sum_a f_a(x_j, k_{1T}^2) \right] \left(\frac{x}{x_j} \right)^{-\lambda} \tag{7.1}$$

where, assuming t-channel pole dominance, the sum over the parton distributions is

$$\sum_a f_a \;=\; g + \frac{4}{9}(q + \bar{q}). \tag{7.2}$$

The factor α_s arises in Eq. (7.1) because the structure function for events with an identified jet is of $O(\alpha_s)$ in relation to the inclusive deep-inelastic structure function F_2. In the next section we show that the QCD prediction has indeed just this type of behaviour and so a measurement of the x/x_j dependence of deep inelastic + jet events should reveal the Lipatov pomeron; it has been heralded as a landmark measurement of QCD [65].

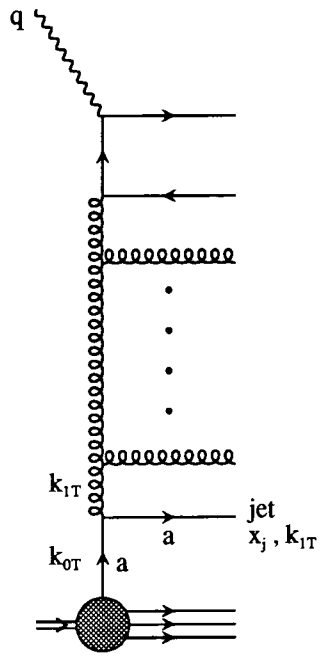

Figure 7.1. Diagrammatic representation of a deep-inelastic event which contains an identified jet with longitudinal and transverse momentum of $x_j p$ and k_{1T} respectively. x_j is chosen as large as experimentally feasible ($x_j \sim 0.1$) and so we assume strong-ordering of the longitudinal, as well as transverse, momentum at the parton a - gluon vertex. Parton a may be either a quark or a gluon.

We have mentioned one reason why this measurement is so special: the choice $k_{1T}^2 \simeq Q^2$ means we have eliminated the strongly-ordered gluon emissions associated with the standard Altarelli-Parisi evolution. However there is a second reason. The small x/x_j behaviour of Eq. (7.1) is directly linked with the high energy behaviour of the virtual photon - virtual parton a cross section. This is evident because the centre-of-mass energy $\sqrt{s_{\gamma a}}$ of this subprocess is given by

$$s_{\gamma a} \simeq 2k_a \cdot q \simeq 2x_j p \cdot q = \left(\frac{x_j}{x}\right) Q^2, \tag{7.3}$$

using $x = Q^2/(2p.q)$. Note that the 4-momentum of the exchanged parton a in Fig. 7.1 is $k_a \simeq x_j p$ on account of the strong-ordering of the longitudinal momenta which holds at

the gluon-a vertex, since x_j is $O(1)$. Thus the proposed experimental determination of the QCD small x behaviour is associated with the high energy behaviour of a *partonic* cross section; as opposed to directly measuring the small x behaviour of parton distributions in a *proton* which necessarily are accompanied by non-perturbative ambiguities (in the form of assumed "starting" x distributions).

The outline of this chapter is as follows. In the next section we will present the QCD form of the differential structure function for deep-inelastic events containing an identified jet. The form of these equations will reveal exactly how the Lipatov Pomeron controls the behaviour of the cross section. Following this, we will describe the equation which generates the Lipatov Pomeron and review its (approximate) analytic solution for the fixed coupling case. In Section 7.3 we will then solve this equation numerically for a running coupling and compare the results with those of the analytic approximation. Our results will show how measurements of the shape of the jet spectrum can reveal the small-x behaviour of QCD.

7.2 The cross section for deep-inelastic + jet events

We are interested in the process in which deep-inelastic scattering is accompanied by a single identified jet. That is the process

$$\gamma^* + p \;\rightarrow\; \text{jet}(x_j, k) + X \tag{7.4}$$

shown in Fig. 7.2 (or Fig. 7.1), where, for convenience, we denote the transverse momentum of the jet as simply $k \equiv k_{1T}$. The differential structure function for this process may be written in the form

$$x_j \frac{\partial F_2(x, Q^2; x_j, k^2)}{\partial x_j \partial k^2} \;=\; \frac{3\alpha_s(k^2)}{\pi k^4} \left[\sum_a x_j f_a(x_j, k^2)\right] F\left(\frac{x}{x_j}, k^2, Q^2\right) \tag{7.5}$$

(cf. Eq. (7.1)), where the sum over the parton distributions is given by Eq. (7.2). The factor F, which has the dimensions of k^2, represents the photon-gluon process shown by the upper blob in Fig. 7.2; that is F/k^2 can be identified with the gluon structure function integrated over the longitudinal momentum of the gluon. The factor k^{-4} in Eq. (7.5) arises from the gluon propagators. Since we are interested in small x/x_j, the magnitude of x_j should be taken as large as is experimentally feasible. In fact it has already been tacitly assumed in Eq. (7.5) (and Eq. (7.1)) that there is strong-ordering of the longitudinal momenta at the gluon-parton a vertex of Fig. 7.2 so that x_j of the exchanged parton, which occurs in $f_a(x_j, k^2)$, is to a good approximation that of the outgoing jet.

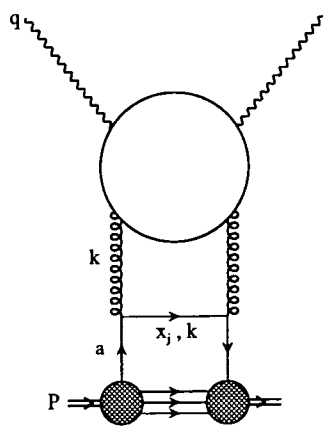

Figure 7.2. The diagram giving the cross section for deep-inelastic scattering events containing an identified jet of longitudinal and transverse momentum $x_j p$ and k respectively.

In the leading $\ln(x_j/x)$ approximation the structure function $F(x/x_j, k^2, Q^2)$ is given by the sum of ladder diagrams shown in Fig. 7.3, together with virtual gluon corrections (not shown). This gives a Lipatov equation for $F(z, k^2, Q^2)$ of the usual form

$$F(z,k^2,Q^2) = F_0(z,k^2,Q^2) + \frac{3\alpha_s}{\pi}k^2 \int_z^1 \frac{dz'}{z'} \int_0^\infty \frac{dk'^2}{k'^2} \left[\frac{F(z',k'^2,Q^2) - F(z,k^2,Q^2)}{|k'^2 - k^2|} + \frac{F(z,k^2,Q^2)}{(4k'^4 + k^4)^{\frac{1}{2}}} \right] \quad (7.6)$$

where the occurrence of $F(z, k^2, Q^2)$ in the integrand is on account of the diagrams with virtual corrections. In Eq. (7.6) the coupling is fixed at $\alpha_s(Q^2)$; we will discuss the effect of allowing α_s to run in the ladder integrations later.

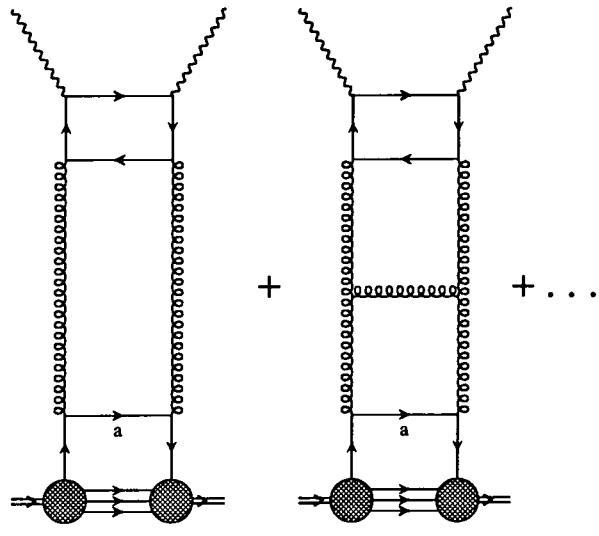

Figure 7.3. The leading $\ln(x_j/x)$ approximation to the process shown in Fig. 7.2.

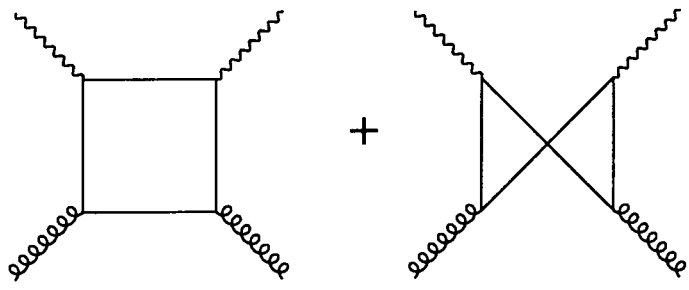

Figure 7.4. The two diagrams embodied in the quark box diagram of Fig. 7.3.

The inhomogeneous or driving term F_0 in Eq. (7.6) corresponds to the sum of the quark box and crossed-box diagrams of Fig. 7.4, shown simply as a box in Fig. 7.3. For transversely polarised photons F_0 has been shown [66] to be

$$F_0(z,k^2,Q^2) \simeq F_0(0,k^2,Q^2) \equiv F_0(k^2,Q^2)$$

where

$$F_0(k^2,Q^2) = 2\sum_q e_q^2 \frac{Q^2}{4\pi^2}\alpha_s \int_0^1 d\beta \int_0^\infty d^2\kappa\, [\beta^2+(1-\beta)^2] \times\left(\frac{\kappa^2}{[\kappa^2+Q^2\beta(1-\beta)]^2} - \frac{\kappa\cdot(\kappa-k)}{[\kappa^2+Q^2\beta(1-\beta)][(\kappa-k)^2+Q^2\beta(1-\beta)]}\right). \quad (7.7)$$

Equation (7.7) applies for arbitrary values of k^2 and Q^2, although here we are interested in $k^2 \simeq Q^2$. In the derivation of Eq. (7.7) the quarks were assumed to be massless and the small longitudinal contribution to F_2 was neglected. This means that, in principle, our results refer to the structure function $2xF_1$ corresponding to transversly polarised virtual photons. For fixed α_s the relative smallness of $F_L = F_2 - 2xF_1$ has been checked [67]. They find that $F_2 : 2xF_1$ are in the ratio $11:9$ (compared with the $1:1$ of the parton model).

The numerical results which we present in Section 7.3 are for values of Q^2 for which it is reasonable to assume that three quark flavours are active. We can rewrite the integrand of Eq. (7.7) in terms of a Feynman integral, which allows the $d^2\kappa$ integration to be performed analytically. In this way we find

$$F_0(k^2,Q^2) = \frac{\sum e_q^2}{4\pi} k^2Q^2\alpha_s \int_0^1 d\beta \int_0^1 d\lambda\, \frac{[\lambda^2+(1-\lambda)^2][\beta^2+(1-\beta)^2]}{[\lambda(1-\lambda)k^2+\beta(1-\beta)Q^2]}. \quad (7.8)$$

As required, F_0 has the dimensions of k^2. Although here we are concerned with the regime where $k^2 \simeq Q^2$, we see from Eq. (7.8) that if $k^2 \ll Q^2$ then $F_0 \sim k^2$ modulo a $\ln(Q^2/k^2)$ factor; whereas if $k^2 \gg Q^2$ we have $F_0 \sim Q^2$, modulo a $\ln(k^2/Q^2)$ factor, which when inserted into Eq. (7.5) leads to the usual k^{-4} behaviour associated with single jet

production. The k^2 behaviour of the driving term F_0 is not transmitted directly to F, but is significantly modified by the Lipatov equation [Eq.(7.6)] particularly at small z, as can be seen by inspection of Eq. (7.9) below.

If, as we have so far assumed, the coupling α_s is fixed then it is possible to use Mellin transform techniques [48, 51, 68] to solve the Lipatov equation (7.6) and obtain an analytic expression for the leading small-z behaviour of $F(z, k^2, Q^2)$. This procedure was adopted in Ref. [66] to yield an analytic approximation for F of the form

$$F(z,k^2,Q^2) = \frac{9\pi^2}{512}\frac{2\sum e_q^2 \alpha_s^{\frac{1}{2}}}{\sqrt{21\zeta(3)/2}}\left(\frac{k^2}{Q^2}\right)^{\frac{1}{2}} Q^2 \frac{z^{-\alpha_P+1}}{\sqrt{\ln(1/z)}}\left[1+O\left(\frac{1}{\ln(1/z)}\right)\right] \qquad (7.9)$$

with $\alpha_P - 1$ given by Eq. (5.27), and where ζ is the Riemann zeta function. When this fixed coupling result is inserted into Eq. (7.5) we obtain the leading small $z \equiv x/x_j$ dependence that was forecast in Eq. (7.1). This analytic approximation, Eq. (7.9), will give at best a rough estimate of the value of $F(z, k^2, Q^2)$. For one thing, the Lipatov equation is based on perturbative QCD and so the transverse momenta of the exchanged gluons along the chains in Fig. 7.1 or Fig. 7.3 should satisfy $k^2 \gg \Lambda^2$, and so should be at least greater than 1 GeV^2 or so. This can be simply achieved by introducing a lower limit cut-off k_0^2 on the transverse momentum integral in Eq. (7.6). Secondly we should allow the couplings α_s to depend on the transverse momenta along the ladder. The conventional way of introducing the k^2 or k'^2 dependence of α_s in Eq. (7.6) is to ensure that, if we were to revert to the strongly-ordered case with $k^2 \ll Q^2$, we would recover the correct evolution equation in the double leading logarithm approximation with a running coupling. Following this procedure we find that the Lipatov equation for $F(z, k^2, Q^2)$ becomes

$$\begin{aligned} H(z,k^2,Q^2) &= H_0(z,k^2,Q^2) \\ &+\frac{3\alpha_s(k^2)}{\pi}\,k^2\int_z^1\frac{dz'}{z'}\int_{k_0^2}^{\infty}\frac{dk'^2}{k'^2}\left[\frac{H(z',k'^2,Q^2)-H(z,k^2,Q^2)}{|k'^2-k^2|}+\frac{H(z,k^2,Q^2)}{(4k'^4+k^4)^{\frac{1}{2}}}\right] \end{aligned} \qquad (7.10)$$

with

$$H(z,k^2,Q^2) \equiv \frac{3\alpha_s(k^2)}{\pi}F(z,k^2,Q^2) \qquad (7.11)$$

and similarly for H_0.

For consistency we should also study the sensitivity of the numerical results to the introduction of a transverse momentum cut-off in the determination of the driving term H_0 or F_0. To do this we write Eq. (7.7) in the form

$$F_0(k^2,Q^2) = \sum e_q^2 \frac{\alpha_s(k^2)}{\pi} k^2\, Q^2 \int_0^1 d\beta \int_0^1 d\lambda \int_{\kappa_0^2}^{\infty} d\kappa'^2 [\beta^2 + (1-\beta)^2]\, \lambda \times \frac{(2\lambda-1)\kappa'^2 + (1-\lambda)[\lambda(1-\lambda)k^2 + \beta(1-\beta)Q^2]}{[\kappa'^2 + \lambda(1-\lambda)k^2 + \beta(1-\beta)Q^2]^3} \tag{7.12}$$

(which is now purely in terms of scalar quantities) and impose the lower cut-off, κ_0^2, on to the transverse momentum integration.

In the next section we describe how we solve the Lipatov equation, [Eq. (7.10)], numerically. We present results for deep-inelastic events with an identified jet for the choice of the transverse momenta cut-offs given by $k_0^2 = \kappa_0^2 = 1$ GeV^2 and we compare with those obtained from the approximate analytic expression, Eq. (7.9). We also investigate the sensitivity of the results to the choice of the value of the cut-offs.

7.3 Numerical QCD estimates of deep-inelastic + jet events

The analytic expression, Eq. (7.9), is only an approximation for the leading small z behaviour of $F(z,k^2,Q^2)$ and thus to make a reliable quantitative estimate of deep-inelastic scattering with a measured jet we must solve the Lipatov equation, Eq. (7.10). This integral equation for $F(z,k^2,Q^2)$ is based on a leading $\ln(1/z)$ summation and so is not expected to be applicable beyond the small z region. On the other hand we anticipate that the inhomogeneous term $F_0(z,k^2,Q^2)$ itself should be a reasonable approximation to $F(z,k^2,Q^2)$ in the large z region, particularly for the $k^2 \sim Q^2$ values that we are studying.

This follows because the standard Altarelli-Parisi QCD evolution should be applicable in this region and when $k^2 \simeq Q^2$ the evolution length ($\sim \alpha_s \ln(Q^2/k^2)$) is very small so that the effects of evolution can be safely neglected. We can therefore restrict the study of the Lipatov equation (7.10) to the small z region, $z < z_0$, by imposing the boundary condition

$$F(z_0, k^2, Q^2) \simeq F_0(z_0, k^2, Q^2) = F_0(k^2, Q^2) \tag{7.13}$$

where z_0 is chosen sufficiently small so that Eq. (7.8) is a reasonable approximation for F_0. This means we can solve the Lipatov equation (7.10) by writing it in the form of an integro-differential equation

$$z\frac{\partial H}{\partial z} = K \otimes H \tag{7.14}$$

where K is the kernel and $\otimes$ denotes the integration over k'^2. We impose the boundary conditions

$$H(z_0, k^2, Q^2) = H_0(k^2, Q^2) \tag{7.15}$$

and choose $z_0 = 0.1$. For any small z the solution $H(z, k^2, Q^2)$ therefore only depends on the behaviour of H in the interval (z, z_0).

Using this procedure we obtain the results shown in Fig. 7.5. To be precise the continuous curves are the values of $F(z, k^2, Q^2)$ determined by solving Eq. (7.14) using three different values of the transverse momentum cut-off, namely $k_0^2 = 1$, 2 and 4 GeV^2. For comparison, the dashed curve is the approximate analytic form [Eq. (7.9)] shown as $F(z/z_0, k^2, Q^2)$ as a function of z, which corresponds to the leading $\ln(z_0/z)$ behaviour of the Lipatov equation with fixed coupling $\alpha_s(Q^2)$ and with the boundary condition $F = F_0$ at $z = z_0$. This asymptotic form is of course not valid for $z \simeq z_0$ and so is only shown in Fig. 7.5 for $z/z_0 < 0.1$.

Several features of Fig. 7.5 are worth noting. First, the $z^{1-\alpha_P}$ behaviour of F soon emerges from the integro-differential equation as z decreases from z_0. As expected the

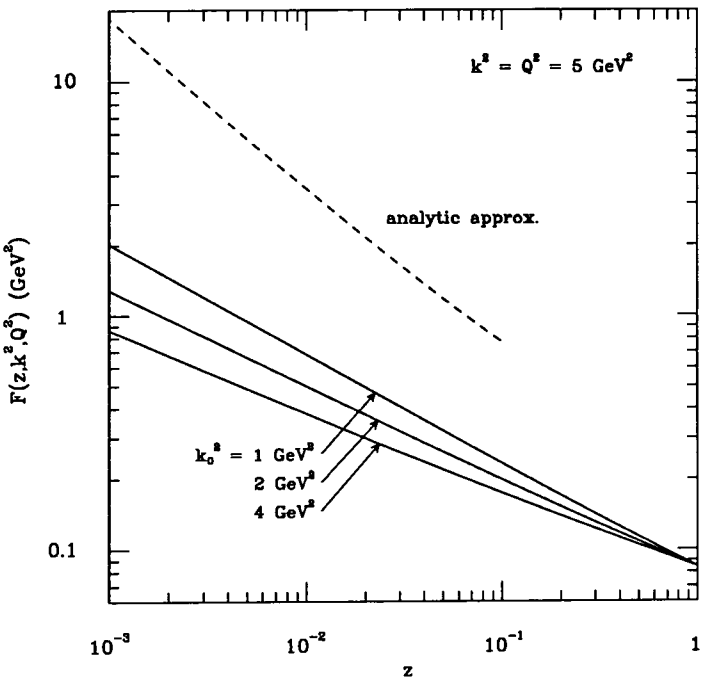

Figure 7.5. The photon-gluon structure function factor $F(z, k^2, Q^2)$ which controls, via Eq. (7.5), the strength of the differential structure function for deep-inelastic (x, Q^2) events with an identified jet (x_j, k^2).The continuous curves are calculated from the integro-differential form Eq. (7.14) of the Lipatov equation Eq. (7.10) for three different choices of the transverse momentum cut-off, $k_0^2 = 1$, 2 and 4 GeV^2 respectively. The solution is matched to the quark-box driving term F_0 at $z = z_0 = 0.1$. The dashed curve shows, for comparison, the analytic leading $\ln(z_0/z)$ approximation, Eq. (7.9), for $F(z/z_0, k^2, Q^2)$. Here we take $\kappa_0^2 = 1$ GeV^2 in Eq. (7.12).

slope $1 - \alpha_P$ is sensitive to the choice of the transverse momentum cut-off and is, in fact, controlled by the value of $\alpha_s(k_0^2)$. The "asymptotic" values of the slopes of the curves in Fig. 7.5 for the cut-off choices $k_0^2 = 1$, 2 and 4 GeV^2 correspond to $\alpha_P - 1 = 0.48$, 0.42 and 0.38 respectively. These are in complete agreement with the behaviour of the solutions of the Lipatov equation for the gluon distribution which we found in Chapter 6. Secondly we see from Fig. 7.5 that the approximate analytic form for F substantially overestimates the numerical solutions and, in particular, that it has a steeper form with

decreasing z. The reason is a little subtle. The (negative) slope, $\alpha_P - 1$, at very small z can be directly identified with the maximum eigenvalue of the kernel of the Lipatov equation (see, for example, [50] for a simplified explanation). In the fixed coupling case the leading eigenvalue $\alpha_P - 1$ is given by Eq. (5.27) with $\alpha_s = \alpha_s(Q^2)$. In the more realistic running coupling case the maximum eigenvalue is controlled by $\alpha_s(k_0^2)$ and, since all the chosen cut-offs k_0^2 are less than Q^2, we would at first sight expect the continuous curves to have steeper slopes than the dashed "fixed coupling" curve. However it turns out that the coefficient of $\alpha_s(k_0^2)$ in the running coupling case is numerically much smaller (and dependent on k_0^2) than the coefficient $12\ \ln 2/\pi$ of the fixed α_s occurring in Eq. (5.27).

We are now in a position to show our main result, which is the behaviour of the differential structure function, $\partial F_2/\partial x_j \partial k^2$, for deep-inelastic (x, Q^2) events containing a measured jet (x_j, k^2) as a function of x and x_j for fixed values of k^2 and Q^2. We evaluate Eq. (7.5) using the values of $F(x/x_j, k^2, Q^2)$ obtained for $k_0^2 = \kappa_0^2 = 1$ GeV^2 and with $\sum f_a$ calculated from the g, q and $\bar{q}$ parton distributions of set B_- of KMRS [50]. The results are shown by the continuous curves in Fig. 7.6 as a function of x_j for different values of x where in the upper figure $k^2 = Q^2 = 5$ GeV^2 while in the lower figure the jet transverse momentum k is increased to $k^2 = 10$ GeV^2.

For comparison we also plot in Fig. 7.6 (as a dashed curve) the approximation where the full solution for $F(x/x_j, k^2, Q^2)$ is replaced in Eq. (7.5) simply by the quark-box driving term $F_0(x/x_j, k^2, Q^2)$. The difference between the continuous and dashed curves for the differential structure function (i.e. inputting F versus F_0) is the Lipatov effect. The input, $F_0(z, k^2, Q^2)$, for the dashed curves is independent of z and the x_j dependence is entirely due to that of the quark and gluon distributions in the proton, whereas the continuous curves also embody the rapid "Lipatov" increase of $F(z, k^2, Q^2)$ with increasing $z = x/x_j$. Inspection of Fig. 7.6 shows that the difference is dramatic, particularly at small $x (x \lesssim 10^{-3})$, in the region $x_j \sim 0.1$. As was explained below Eq. (7.5), the magnitude of

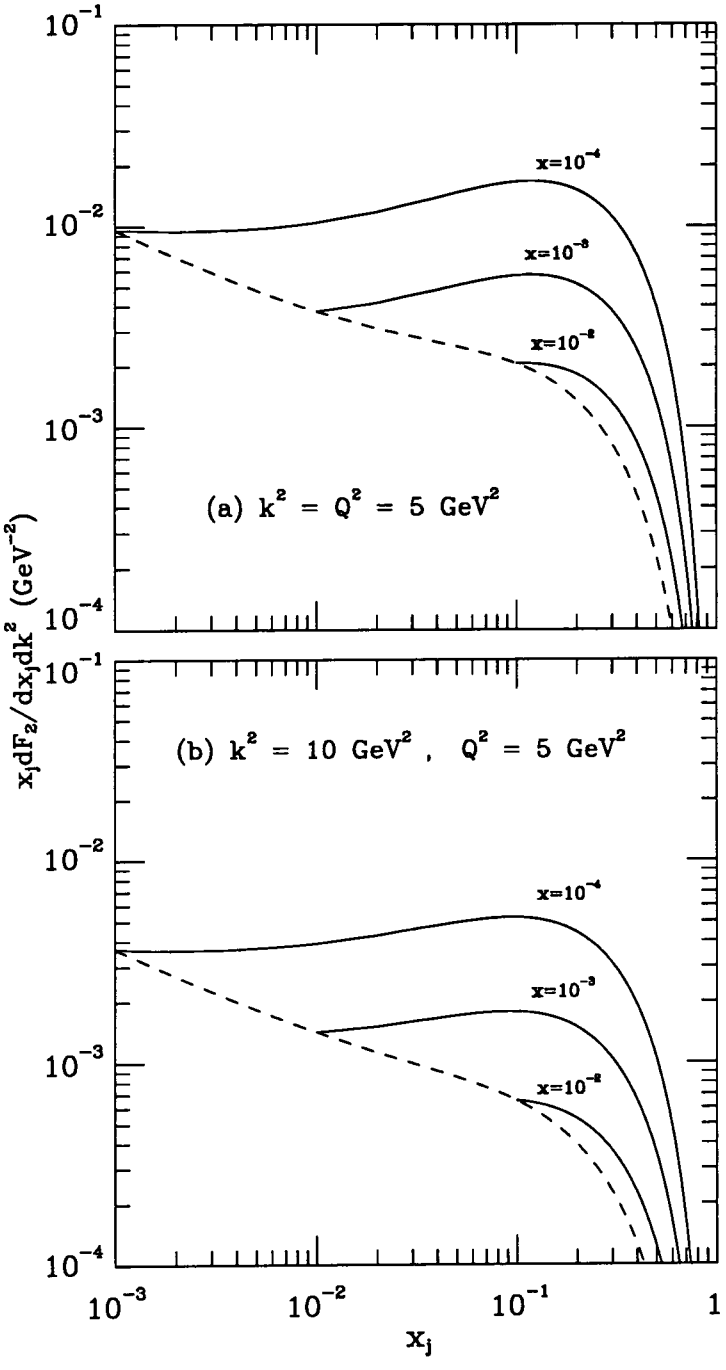

Figure 7.6. The differential structure function, Eq. (7.5), for deep-inelastic (x, Q^2) events with an identified jet (x_j, k^2) as a function of x_j for different values of x, $x = 10^{-4}$, 10^{-3} and 10^{-2}, and for $Q^2 = 5$ GeV^2. The dashed curve is obtained from Eq. (7.5) with F replaced by simply the driving term F_0. The cut-offs are chosen to be $k_0^2 = \kappa_0^2 = 1$ GeV^2. Figures (a) and (b) correspond to jet transverse momentum squared $k^2 = 5$ and 10 GeV^2 respectively.

x_j should be of this order for our formalism to be valid. That is the results of Fig. 7.6 are only expected to be reliable for $x_j \gtrsim 0.05$.

It would be tempting to conclude that measurements of deep-inelastic scattering events with an identified jet can reveal the QCD singular Lipatov behaviour from observing either the shape or the magnitude of $\partial F_2/\partial x_j \partial k^2$. However the (x_j, x) shape is a more reliable discriminator than the magnitude since, as we shall show, the normalisation of the QCD predictions is subject to uncertainties arising mainly from the choice of the cut-offs in the integrations over the transverse momenta. First we show in Fig. 7.7 the dependence of the results to the choice of the cut-off k_0^2 in Eq. (7.10) (or Eq. (7.14)). We give predictions for $k_0^2 = 1$, 2 and 4 GeV^2. Although the choice $k_0^2 = 4$ GeV^2 is extreme, the uncertainty in normalisation is apparent. We now turn to the effect of the cut-off ambiguity in the calculation of the driving term F_0. Fig. 7.8 shows results for the cut-off choices $\kappa_0^2 =$ 0, 1 and 2 GeV^2 in the transverse momentum integration of Eq. (7.12). Again we see a substantial change in normalisation but very little effect on the shape of the differential structure function.

Fig. 7.9 shows the QCD predictions for the differential structure function for deep-inelastic scattering with an identified jet with transverse momentum squared $k^2 > 5$ GeV^2 as a function of x_j for different values of x. That is Eq. (7.5) integrated over k^2 from 5 GeV^2 upwards. If we then carry out the integration over x_j we would find the fraction of such events in relation to an inclusive deep-inelastic measurement of F_2. For example from Fig. 7.9 we find at $x = 10^{-3}$ (and $Q^2 = 5$ GeV^2) that the doubly-integrated structure function is

$$F_2^{jet}(x, Q^2; x_j > 0.05, k^2 > 5 \text{ GeV}^2) = 0.071 \tag{7.16}$$

as compared to the KMRS (set B_-) prediction of $F_2(x, Q^2) = 0.32$, that is roughly an order-of-magnitude reduction as would be expected for an $O(\alpha_s)$ subprocess. We should

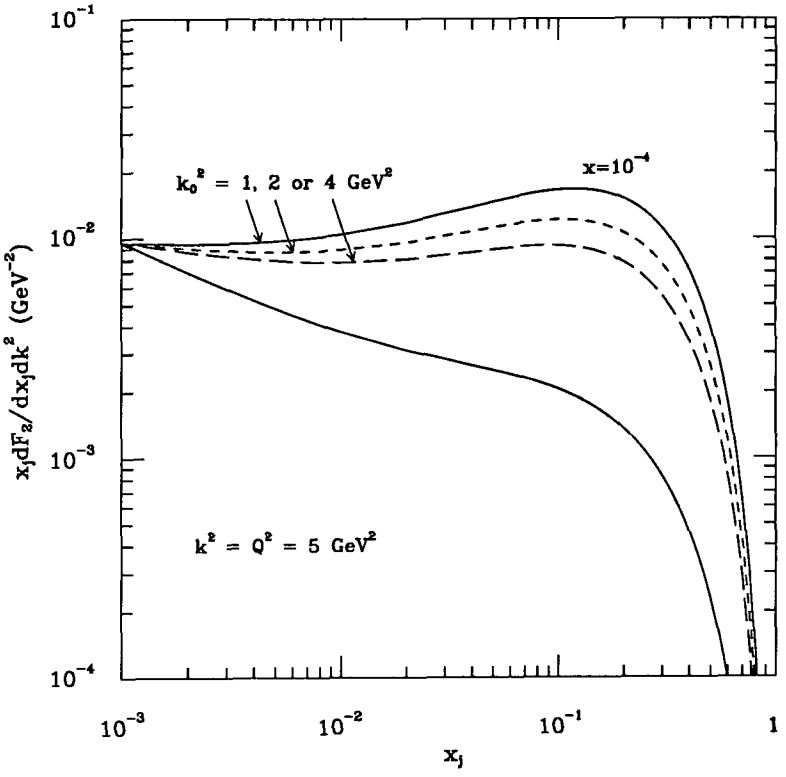

Figure 7.7. The sensitivity of the QCD predictions of the differential structure function Eq. (7.5) to the choice of the cut-off k_0^2 of Eq. (7.10). The lower curve, shown for reference, is for F replaced by F_0 in Eq. (7.5). Here we take $\kappa_0^2 = 1$ GeV^2 in Eq. (7.12).

keep in mind however, that the normalisation of F_2^{jet} has a large uncertainty (of order a factor of 2 either way) arising from the sensitivity of the QCD prediction to the choice of the values of the cut-offs, k_0^2 and κ_0^2, on the integrals over the transverse momenta.

So far we have neglected shadowing corrections. The rapid growth of the photon-virtual gluon subprocess in Fig. 7.2 with decreasing x/x_j cannot go on indefinitely, but must ultimately be suppressed by shadowing or recombination effects. These shadowing corrections in the photon - virtual gluon channel preserve the factorization-like form [Eq. (7.5)] of the differential structure function $x_j \partial F_2/\partial x_j \partial k^2$. The corrections give rise to non-linear terms in the integro-differential equation (7.10) for H which would slow the rapid growth of $F(z, k^2, Q^2)$ with decreasing z.

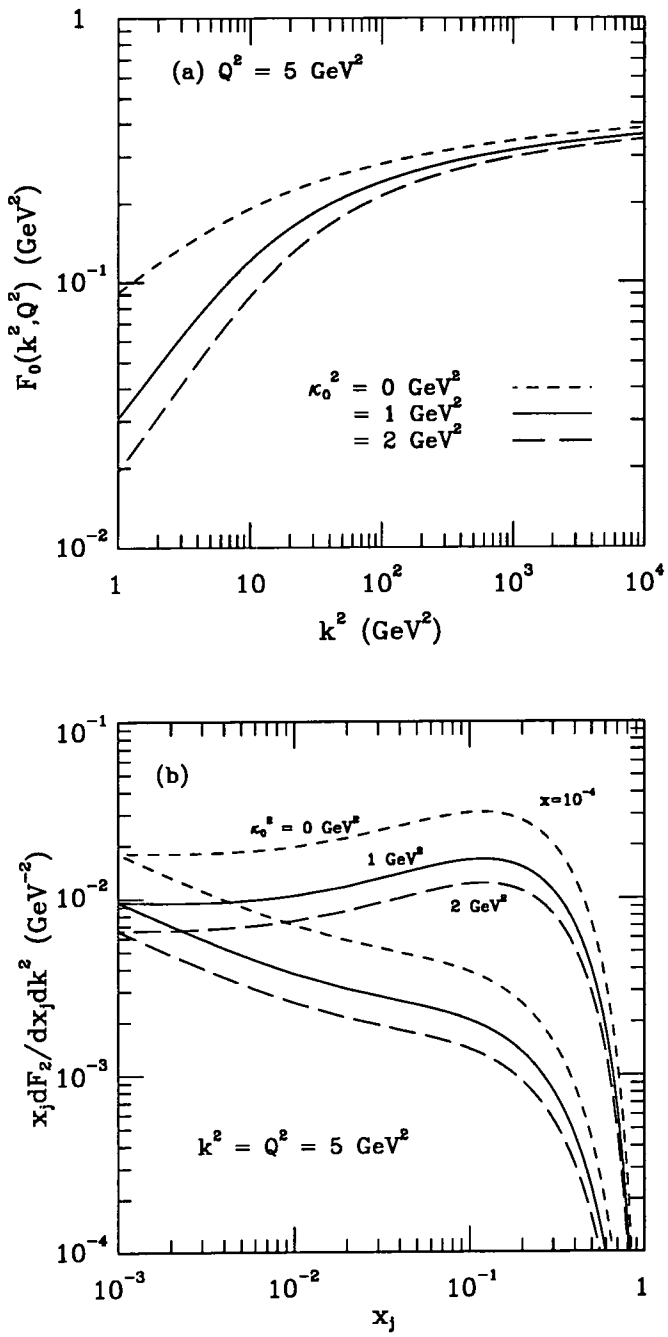

Figure 7.8. (a) The quark-box "driving term" $F_0(k^2, Q^2)$ of Eq. (7.12) calculated as a function of k^2 for three different values of the cut-off, namely $\kappa_0^2 = 0$, 1 and 2 GeV^2. (b) The forms of the differential structure function Eq. (7.5) obtained with F calculated using the three forms of F_0 shown in (a). The three lower curves in (b) are obtained from Eq. (7.5) when F is replaced by F_0.

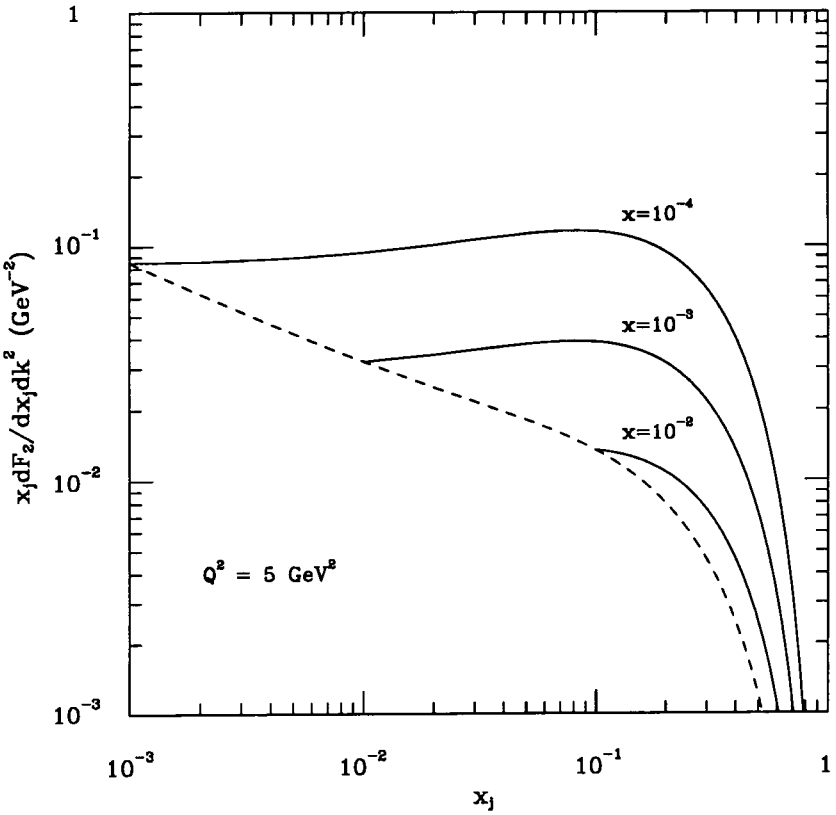

Figure 7.9. The differential function for deep-inelastic (x, Q^2) events with a measured jet (x_j, k^2) with transverse momentum squared $k^2 > 5$ GeV^2, shown as a function of x_j for three values of x. The cut-offs are chosen to be $k_0^2 = \kappa_0^2 = 1$ GeV^2. The dashed curve, shown for reference, is obtained from Eq. (7.5) when F is replaced by F_0.

Conceptually these effects are the same as the shadowing contributions which occur in another process, one for which we have some experience, namely the shadowing corrections to the gluon distribution $g(x, Q^2)$ itself. In this case the rapid rise, with decreasing x, is in the virtual gluon-proton channel, and the suppression is found [50, 62] to be small for $x \gtrsim 10^{-3}$. We would therefore expect that the QCD predictions that we have shown, for which $z \equiv x/x_j > 10^{-3}$, will have negligible corrections for shadowing in the photon-virtual gluon channel. Of course it is possible that shadowing will be more complicated, and even spoil the factorization structure of Eq. (7.5), but it is unlikely that it will significantly distort the shape of the jet spectrum in the region $x/x_j \gtrsim 10^{-3}$ accessible to HERA.

7.4 Summary

In this chapter we have studied the proposal that the measurement of the jet electroproduction spectrum in the small x region allows a unique probe of the novel QCD effects which are expected to occur in this region. Indeed such an experiment offers a particularly clean way to reveal the QCD (pomeron) singularity implied by the leading $\ln(1/x)$ resummation. The measurement has a different character from, and is complementary to, the other proposed experimental probes of the small x behaviour of the parton distributions such as heavy quark [69, 70, 71] and J/ψ [72] electroproduction, prompt photon production [71] and ordinary inclusive deep-inelastic lepton-nucleon scattering. Although such direct measurements of parton distributions are extremely valuable, it will be difficult to use them to identify unambiguously the genuine Lipatov QCD growth with decreasing x. The reason is that these processes (a) involve evolution in Q^2 which steepens the small-x parton behaviour with increasing Q^2 and (b) require us to assume some input form of the parton distributions, $f_a(x, Q_0^2)$ (with, say, $Q_0^2 = 4$ GeV^2), which contain non-perturbative effects. Thus we cannot be sure whether an observed steep small-x behaviour is due to a combination of our input assumptions and the Q^2 evolution or is indeed a genuine Lipatov perturbative QCD effect.

The unique feature of the measurement of deep inelastic (x, Q^2) events containing an identified jet (x_j, k^2) is the potential possibility of eliminating the effect of the conventional QCD evolution by choosing $k^2 \simeq Q^2$ and to isolate cleanly the small x/x_j behaviour directly at the *partonic* level. Recall from our discussion in Section 7.1 that, since

$$\left(\frac{x_j}{x}\right) Q^2 \simeq s_{\gamma a},$$

the small x/x_j behaviour is directly linked to the high c.m. energy $\sqrt{s_{\gamma a}}$ behaviour of a *partonic* subprocess, that is the virtual photon - virtual parton a subprocess in Fig. 7.2.

A similar kinematical *parton* configuration can, in principle, be achieved in di-jet production in hadronic collisions [73], but the study of single jets in *ep* collisions should be experimentally much more accessible, particularly with the advent of HERA.

We found that the singular small-x Lipatov effects dramatically modify both the shape and the normalisation of the jet spectrum in *ep* collisions (see, for example, the difference between the continuous and dashed curves in Fig. 7.6). The overall normalization is found to be subject to ambiguities related to the choice of the low transverse momentum cut-off. It is here that non-perturbative effects enter our study and lead to some uncertainty in the exponent of the QCD singular $z^{1-\alpha_P}$ behaviour with, for different choices of the cut-off, $\alpha_P - 1$ ranging from about 0.35 to 0.5. However, the shape of the jet spectrum is much less sensitive to the choice of the cut-offs and so such measurements should serve as an ideal means of identifying the QCD small-x behaviour.

We conclude that measurements of deep-inelastic (x, Q^2) events accompanied by an identified jet (x_j, k^2), with $k^2 \simeq Q^2$, should provide a clean and unique way of investigating the Lipatov perturbative QCD growth expected at small $z \equiv x/x_j$. Whether such measurements are currently possible will depend on the kinematical region accessible to present particle colliders. In the next chapter we will therefore study the feasability of making these deep-inelastic scattering + jet measurements at the HERA ep collider.

8 Probing the Lipatov $z^{-\lambda}$ behaviour at HERA

8.1 Introduction

The calculations of the previous chapter show that measurements of deep-inelastic scattering events with an extra identified jet should be an excellent probe of the behaviour of perturbative QCD in the small x region. We now turn our attention to the feasability of actually making such measurements at the HERA ep collider. We begin with a brief review of the standard event kinematics for deep-inelastic scattering and the region in which it is possible to reconstruct both x and Q^2 with reasonable accuracy. We then move on to examine the constraints imposed by the need to identify an extra jet which is separate from both the current and fragmentation jets. Finally we compute the cross section for the deep-inelastic scattering + jet process using the predictions for $F(z, k_T^2, Q^2)$ obtained in the previous chapter. The variation of this cross section shows that the identification of the $z^{-\lambda}$ behaviour is feasible if jets with $k_T^2 \simeq Q^2 \simeq 40$ GeV^2 can be measured at HERA.

8.2 Event kinematics

8.2.1 The event kinematics for deep-inelastic scattering

In chapter 2 we saw that only two independent variables are necessary to define completely the deep-inelastic scattering interaction. These variables are traditionally x and Q^2 although sometimes the variable $y \equiv (P.q)/(P.k)$ is more convenient. Each of these variables can be expressed in terms of the scattering angle between the leptons, θ_l, and their respective energies, E_e and E_l shown in Fig. 8.1.

$$Q^2 = 4E_eE_l\cos^2\frac{\theta_l}{2} \tag{8.1}$$

$$y = 1 - \frac{E_l}{E_e}\sin^2\frac{\theta_l}{2} \tag{8.2}$$

and

$$x = \frac{Q^2}{sy} \tag{8.3}$$

where s is the centre of mass squared energy, $s = 4E_eE_p$. Notice that angles are measured from the proton beam direction and that, unlike the traditional fixed-target expressions for deep-inelastic scattering, these equations are valid in any frame, provided the rest masses of the colliding particles can be neglected.

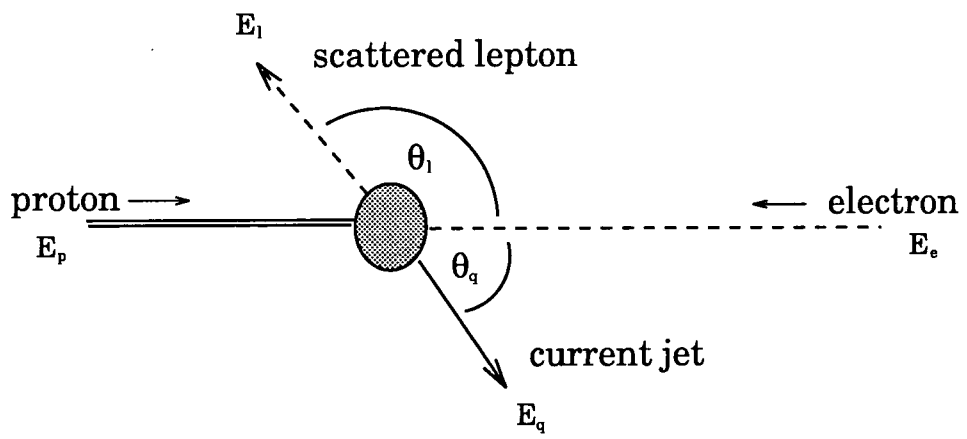

Figure 8.1. The kinematics of deep-inelastic scattering.

When examining the region where good reconstruction of both x and Q^2 is possible there are two considerations which must be taken into account. The first of these is the effect of particle losses due to the beam pipe and the detectors, whilst the second is a knowledge of the errors inherent in any particular event reconstruction technique. Let us examine each limitation in turn. The most serious restriction on the (x, Q^2) plane will be from the beam pipe which will remove a large section of the low Q^2, large x region. This corresponds to electrons which undergo only slight scattering and travel onwards along the beam pipe. The losses from electrons which are backscattered in the beam pipe are not so important. Although they occur at the smallest x values, this region (where $y \sim 1$) also suffers from other, more serious problems. The first of these problems arises from the presence of large backgrounds due to both photoproduction ($\pi\gamma$) and charm decays which can mimic genuine deep-inelastic scattering electrons in the detector. The second problem arises from the increased size of the radiative corrections in the large y region which will reduce the momentum of the incident electron from the measured beam value. In order to ensure that both of these effects are small it is necessary to cut on the y variable at around $y \simeq 0.9$. Lastly we need to consider the errors associated with the reconstruction of the deep-inelastic scattering variables x and Q^2. If we compute these variables from Eqs. (8.1-8.2) then we find that the resolutions are given by

$$\frac{\delta Q^2}{Q^2} = \frac{\delta E_l}{E_l} + \tan\frac{\theta_l}{2}\delta\theta_l \tag{8.4}$$

and

$$\frac{\delta x}{x} = \frac{1}{y}\frac{\delta E_l}{E_l} + \frac{1}{y}\left[\frac{(1-y)}{\sin^2\theta_l/2} - 1\right]\tan\frac{\theta_l}{2}\delta\theta_l \tag{8.5}$$

Notice that whilst the Q^2 resolution is good for all y values, the x resolution is singular as $y \to 0$. As a result, the errors in the x variable will be large for $y \lesssim 0.1$. Possible ways around this problem have been suggested which rely on reconstructions of x and Q^2 from combinations of the angles and energies of both the leptons and hadrons. For example,

the Jacquet-Blondel method [74] uses only the hadronic information to obtain y and Q^2

$$Q^2 = \frac{1}{1-y}\sum P_T^2 \tag{8.6}$$

$$y = \frac{1}{2E_e}\sum (E_H - P_z) \tag{8.7}$$

where the sum extends over all hadrons. One of the advantages of this technique is that the y resolution

$$\frac{\delta y}{y} = \frac{\delta E_q}{E_q} + \cot\frac{\theta_q}{2}\delta\theta_q \tag{8.8}$$

is free of both $1/y$ and $1/(1-y)$ singularities. For our study of deep-inelastic scattering + jets, however, we do not need to resort to such techniques. We will find that we can remain in the small x region where $y > 0.1$ and here the reconstruction of x and Q^2 from the lepton variables is expected to yield the smallest errors [75].

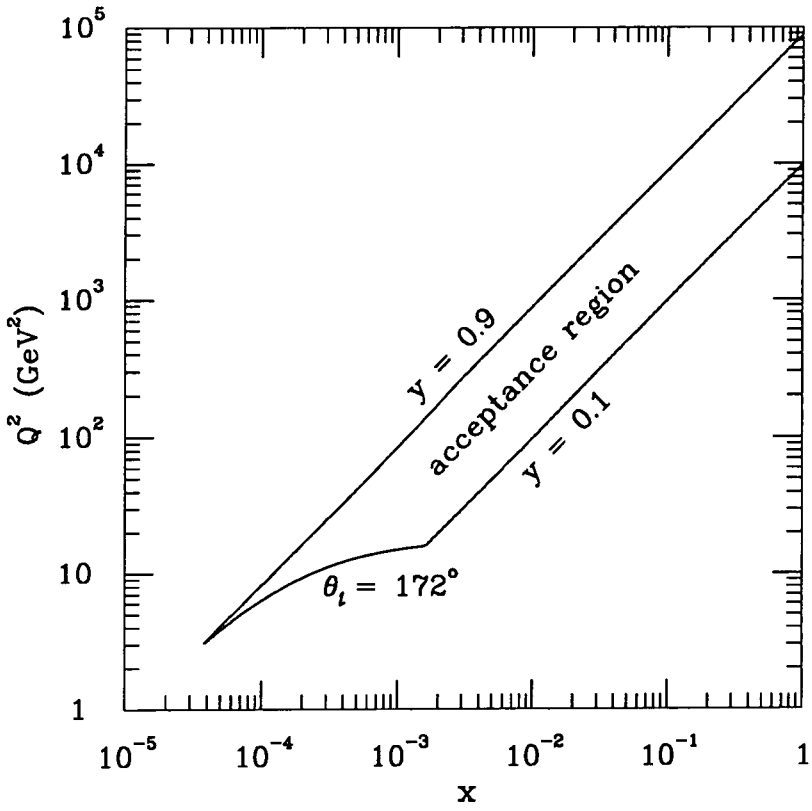

Figure 8.2. The accessible (x, Q^2) range at HERA in which accurate x and Q^2 reconstruction is possible from only lepton scattering measurements.

Figure 8.2 shows the region of the (x, Q^2) plane available for deep-inelastic scattering measurements when the above cuts are applied. Notice that there is no overlap between this region and the region probed by previous fixed target experiments. Even with the extra regions available from other x,Q^2 reconstruction techniques, it will still be necessary to run HERA at a lower proton energy to achieve any comparison with past experiments.

8.2.2 Event kinematics for an extra identifed jet

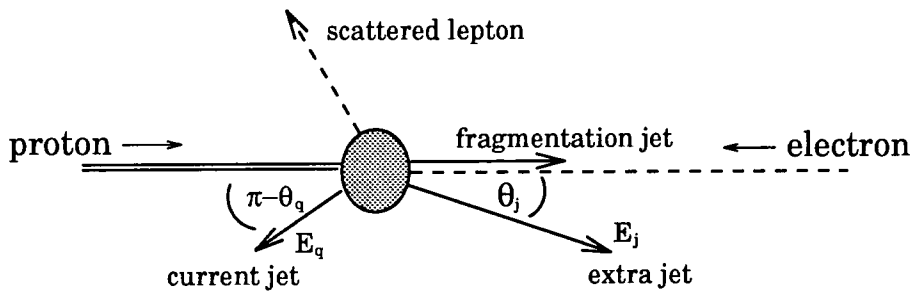

Figure 8.3. Kinematics of the deep-inelastic scattering + jet process

We are interested in events which contain an extra measured jet in the region where the ratio x/x_j is small. This means that we must compute the acceptance regions for these jets, taking into account the beam pipe losses and the restrictions imposed by the requirements that $z = x/x_j < 0.1$ and $k_T^2 \simeq Q^2$. If we work at the parton level then expressions for the jet kinematic variables x_j and k_T^2 can be easily computed from the event kinematics [76]. The resulting equations are

$$2P.k = \frac{k_T^2}{x_j} = 2E_j E_p(1 - \cos\theta_j) \tag{8.9}$$

$$2q.k = x_j s' - \frac{x}{x_j}k_T^2 = 2E_j(E_e - E_l + \Phi) \tag{8.10}$$

where, if we write the four vector k_l as $k_l = (E_l, x_l, y_l, z_l)$, then Φ is given by

$$\Phi = \cos\theta_j E_e - \sin\theta_j \cos\phi_j x_l - \sin\theta_j \sin\phi_j y_l - \cos\theta_j z_l \tag{8.11}$$

s' is given by $s' = 2P.q$. The azimuthal angle of the jet, ϕ_j, is not uniquely defined by the scattering and we therefore average over all possible azimuthal angles. From these equations we can derive the relationship between the relevant jet momenta and the jet angle θ_j.

$$x_j^2 = \frac{Q^2}{x}\left[\frac{k_T^2(E_e - E_l + \Phi)}{E_p(1-\cos\theta_j)} + xk_T^2\right] \tag{8.12}$$

This relationship is shown in Fig. 8.4 and consequently we can see that the large x_j jets of interest are only emitted at small θ_j. This is a fairly serious limitation because jets at small angles are likely to suffer from losses in the beam pipe. If we look for jets with higher transverse momenta then for a fixed x_j we can reach larger θ_j values, but only at the expense of a dramatic drop in the event rate.

Figure 8.5 shows the acceptance regions for these jets for various choices of the cuts on the jet variables x_j and θ_j (together with the constraints $\frac{1}{2}Q^2 < k_T^2 < 2Q^2$ and $z \equiv x/x_j < 0.1$). These regions appear as triangular-like shapes and are superimposed onto the acceptance region for the detected electron (shown by a dashed line). Clearly it is only in the overlap of the jet and electron acceptance regions that the deep-inelastic + jet events can be measured.

To identify the Lipatov $z^{-\lambda}$ behaviour we need deep-inelastic + jet events, with $k_T^2 \simeq Q^2$, over an interval of $z \equiv x/x_j$ which covers values of z as small as is experimentally possible. As a compromise we select the region $x_j > 0.05$ and $x < 2 \times 10^{-3}$, which limits $Q^2 \lesssim 200$ GeV^2, see Fig. 8.5.

All of the above cuts on the deep-inelastic scattering variables are summarised in Table 8.1 [77].

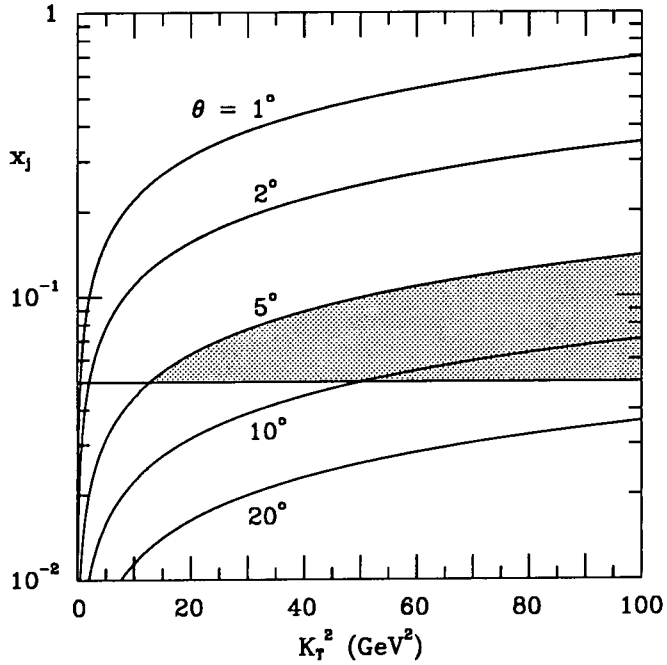

Figure 8.4. The relation between the jet kinematic variables for deep-inelastic + jet events with $x = 5 \times 10^{-3}$ and $Q^2 = 20$ GeV^2; see also Ref. [76]. θ_j, the jet angle to the proton direction in the HERA (30 × 820 GeV) laboratory frame, is not uniquely specified by $(x, Q^2; x_j, k_T^2)$. Varying the remaining azimuthal angle transforms the lines of constant θ_j into narrow bands in the x_j, k_T^2 plane. The lines shown are obtained by averaging over the azimuthal degree of freedom. The plot is insensitive to variations of x, Q^2 over their relevant intervals. The cross sections shown in Fig. 8.6 correspond to jets lying in the shaded band, but subject to the additional constraint $\frac{1}{2}Q^2 < k_T^2 < 2Q^2$.

Table 8.1 *Summary of the cuts used to calculate the acceptance regions for deep-inelastic scattering events with an extra identified jet.*

Cut	Reason for cut
$8° < \theta_l < 172°$	Lepton losses in the beam pipe
$0.1 < y < 0.9$	Backgrounds, radiative corrections and x resolution
E_j, $E_l > 5$ GeV	The energy resolution of the detectors
$\frac{1}{2}Q^2 < k_T^2 < 2Q^2$	The requirement that $k_T^2 \simeq Q^2$
$\theta_j > 5°$	Jet losses in beam pipe
$z < 0.1$	The requirement that we remain in the small z region

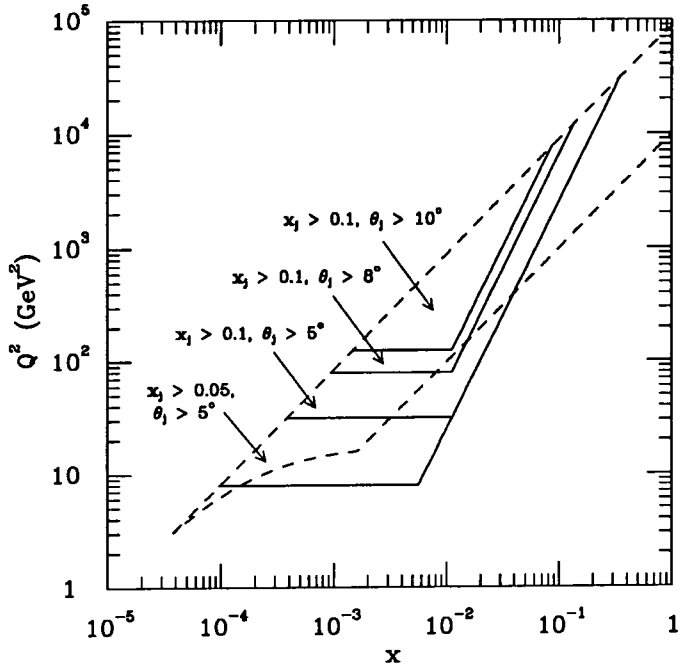

Figure 8.5. The acceptance region for deep-inelastic + jet events at HERA for 30 GeV electrons on 820 GeV protons. The dashed curves outline the acceptance regions for the detected electron ($8° < \theta_e < 172°, E_e > 5$ GeV and $y > 0.1$), whilst the solid curves outline the triangular acceptance regions for jets with different kinematic x_j, θ_j cuts applied (together with the constraints $\frac{1}{2}Q^2 < k_T^2 < 2Q^2$ and $z \equiv x/x_j < 0.1$).

8.3 The cross section for deep-inelastic scattering + jet production

The differential cross section for deep-inelastic scattering + jet production is given by

$$\frac{\partial\sigma}{\partial x \partial Q^2} = \int dx_j \int dk_T^2 \frac{4\pi\alpha^2}{xQ^4}\left[(1-y)\frac{\partial F_2}{\partial x_j \partial k_T^2} + \frac{1}{2}y^2 \frac{\partial(2xF_1)}{\partial x_j \partial k_T^2}\right] \tag{8.13}$$

where the differential structure functions are obtained using the numerical method described in the previous chapter and with the appropriate quark-box boundary conditions (F_0) for F_2 and $2xF_1$. To calculate the (transverse and longitudinal) contributions to F_0 we assume four (massless) active quark flavours. This is a reasonable assumption for the Q^2 values of interest. As usual $y = Q^2/xs$ where $\sqrt{s}$ is the c.m. energy of the incoming

electron-proton system. Figure 8.6 shows the predicted x dependence of the deep-inelastic + jet cross section, (8.13), summed over bins of size $\Delta x = 10^{-4}$ and $\Delta Q^2 = 10$ GeV^2. For reasons given above, we restrict the regions of integration in (8.13) to $x_j > 0.05$ and $\theta_j > 5^0$ (shown shaded in Fig. 8.4, but subject to the additional constraint $\frac{1}{2}Q^2 < k_T^2 < 2Q^2$). We show in Fig. 8.6 predictions for three different Q^2 intervals. The continuous curves give the values of the cross section integrated over the Δx, ΔQ^2 bins when the Lipatov effect is included. These are to be contrasted with the dashed curves which show the values when the Lipatov effect is neglected, that is when just the quark-box approximation, $F = F_0$, is used to evaluate $\partial F_2/\partial x_j \partial k_T^2$ and $\partial(2xF_1)/\partial x_j \partial k_T^2$. The curves are shown only for the region of x for which the cross section can be measured at HERA over the entire individual (Δx, ΔQ^2) bins; that is for those bins which are not cut by the appropriate set of boundary curves of Fig. 8.5. The values of $\langle\sigma\rangle$ are plotted in Fig. 8.6 at the central value of each Δx bin.

The steep rise of the continuous curves with decreasing x (i.e.decreasing $z = x/x_j$) reflects the $z^{-\lambda}$ Lipatov effect. Indeed the Lipatov behaviour is to be identified via the shape (or relative steepness) rather than the value of the deep-inelastic + jet cross section, since the latter is subject to normalisation uncertainties (see Chapter 7). Thus, for example, for the ($20 < Q^2 < 30$ GeV^2) bin we see the integrated cross section $\langle\sigma\rangle$ rises from 3.2 pb to 17.2 pb (a factor of almost 6) as x decreases from the ($1.9\times10^{-3} < x < 2\times10^{-3}$) bin to the ($0.4\times10^{-3} < x < 0.5\times10^{-3}$) bin, whereas without the Lipatov effect the increase would be only about a factor of 3 (that is 1.9 pb to 5.4 pb). The doubling of the steepness of $\langle\sigma\rangle$ is the signature of the Lipatov effect. In practice a larger $k_T^2 \approx Q^2$ will probably be required in order to suppress the background from final state radiation and to ensure that the (x_j, k_T^2) jet can be more readily distinguished from the fragments of the proton. Throughout, we have neglected shadowing corrections since they are not expected to be important in the z range ($z \sim 10^{-2}$) accessible for deep-inelastic + jet events at HERA.

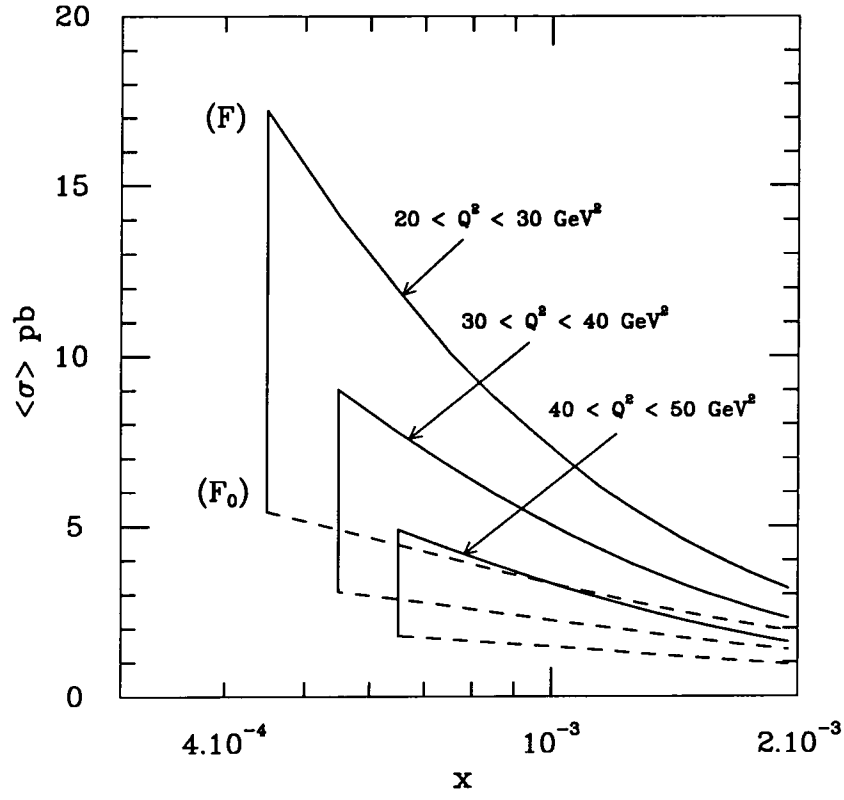

Figure 8.6. The cross section, $\langle\sigma\rangle$ in pb, for deep-inelastic + jet events, integrated over $\Delta x = 10^{-4}$, $\Delta Q^2 = 10$ GeV^2 bins which are accessible at HERA, and integrated over $\theta_j > 5°$ and $x_j > 0.05$, but subject to the constraint $\frac{1}{2}Q^2 < k_T^2 < 2Q^2$. The x dependence of $\langle\sigma\rangle$ is shown for three different ΔQ^2 bins, namely (20,30), (30,40) and (40,50) GeV^2. The $\langle\sigma\rangle$ values are plotted at the central x value in each Δx bin and joined by straight lines. The continuous curves show $\langle\sigma\rangle$ calculated with the inclusion of the Lipatov soft gluon summation, that is to say with the full $F(z, k^2, Q^2)$. The corresponding $\langle\sigma\rangle$ values calculated with just the quark box approximation $F = F_0$ are shown as dashed curves and, for clarity, each is joined with its associated solid curve by a vertical line. The parton distributions used are the B_ set of KMRS [50].

For completeness we also present the integrated cross section $\langle\sigma\rangle$ in the form of numerical values in Fig. 8.7. The number in brackets is the value obtained with the Lipatov effect neglected. Again we can see the growth in the cross section with decreasing x.

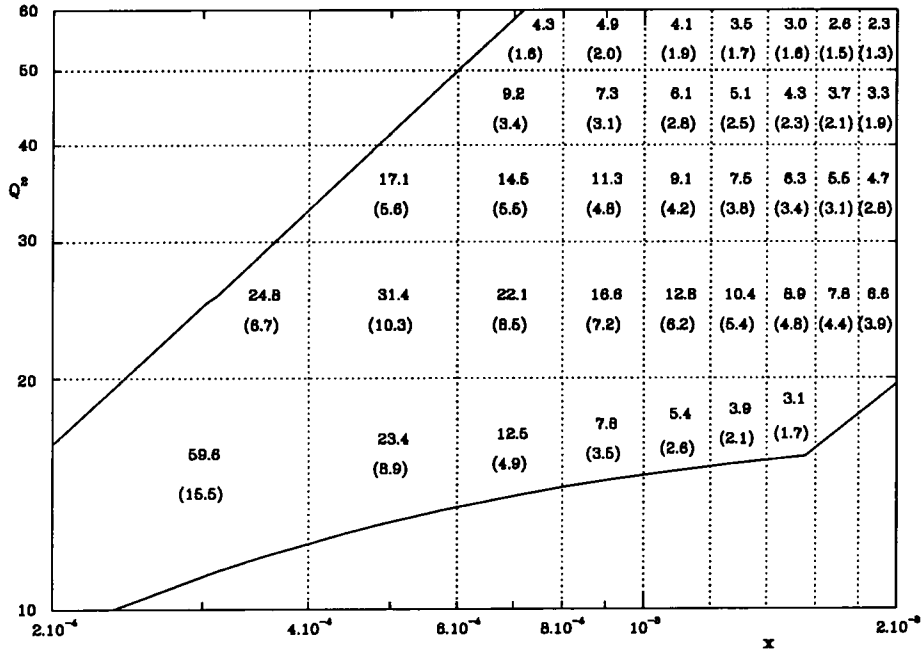

Figure 8.7. The cross section, $\langle\sigma\rangle$ in pb, for deep-inelastic + jet production in various bins which are accessible at HERA. The number in brackets is the value calculated with just the quark box approximation $F = F_0$. The difference between the two numbers is therefore the enhancement due to the Lipatov effect

8.4 Summary

We have seen how measurements of deep-inelastic events, which contain an extra identified jet, can be used to test the Lipatov $z^{-\lambda}$ behaviour at HERA. These measurements need to be at small values of x and large x_j so that the ratio $z \equiv x/x_j$ is as small as possible. However, it is the variation of the cross section with x (rather than its overall normalization) which will ultimately reveal the $z^{-\lambda}$ behaviour. The acceptance region for these deep-inelastic scattering + jet processes is important and will be most seriously limited by the beam pipe. Figure 8.6 shows that, as expected, the larger the value of x_j, the smaller the jet angle, however, measurements below 5° will be prevented by the beam

pipe losses. This problem can be avoided (to some extent) by looking for jets with a higher transverse momentum, k_T^2, although this will result in a smaller event rate and a smaller lever arm in x (and hence z). Inspection of Fig. 8.6 shows that identification of the $z^{-\lambda}$ behaviour is feasible if jets with $k_T^2 \simeq Q^2 \simeq 40$ GeV^2 can be measured at HERA. Finally we emphasize such a determination relies on only a knowledge of parton distributions in a region in which they are well determined, $x_j \gtrsim 0.05$.

9 Summary

In this thesis we have examined the behaviour of parton distributions at both large and small x. A reliable knowledge of these distributions is required for the calculation of hadronic processes within perturbative QCD. Fortunately, the accumulation of high statistics data in recent years, together with the NLO expressions for the accompanying hard scattering sub-processes, has enabled the parton distributions to be fairly well determined in the x range covered by the data. For the proton this range is currently $0.03 \lesssim x \lesssim 0.8$, whilst for the pion it is $0.2 \lesssim x \lesssim 0.8$.

Using the available Drell-Yan data from NA10 and E615, together with prompt photon data from WA70, we have determined the parton distributions for the pion. The Drell-Yan data, whilst constraining the valence quark distributions, allows considerable freedom in the gluon and sea quark distributions. At present, it is the lack of data below $x \simeq 0.2$ which prevents a reliable determination of the pion sea. Despite this problem, we have been able to place upper and lower limits on the sea quark distributions using the momentum sum rules and the Drell-Yan data respectively. The prompt photon data, and, in particular, the $\pi^+ p$ data, has been used to determine the gluon distribution. The advantage of this process is due to the dominance of the Compton terms over the annihilation terms. The largest uncertainty in the resulting gluon distribution arises from the ambiguities contained within the pion sea. Using the parton distributions obtained from our fits, we have compared the predictions for the first two pion moments with those from lattice computations. We find the two calculations to be in agreement.

In addition to our study of the parton distributions relevant to the pion, we have examined the behaviour of parton distributions at very small values of Bjørken x. Small x physics is currently a subject of great interest (both theoretically and experimentally) because of the new effects which are expected to become visible at the next generation of colliders, namely HERA, the LHC and SSC. The equation which determines the behaviour of parton distributions in the small x region is the Lipatov equation with the inclusion of extra non-linear "shadowing terms". These additional terms originate from the gluon-gluon recombination effects which are expected to become important at low values of x. The resulting expression is also known as the GLR equation. Although it has previously been solved (analytically) with fixed α_s, we are the first to obtain a (numerical) solution with a running α_s coupling. Our solution generated the $x^{-\lambda}$ behaviour predicted for the small x gluon distribution. This behaviour is found to be stable to evolution in Q^2, although the value of λ depends on the infra-red cut-off, k_0^2, required for the transverse momentum integration. Our solutions demonstrate how the inclusion of shadowing terms into the evolution dampens the $x^{-\lambda}$ growth, causing the gluon distribution to flatten off towards small values of x. The size of this effect is controlled by the shadowing parameter, R, which determines the size of the area in which gluon saturation occurs. If saturation occurs evenly throughout the proton then R will be comparable to the proton radius ($R \simeq 5$ GeV^{-1}) whilst if saturation takes place in localised regions (hot-spots) then R will be much smaller, (for example, $R \simeq 2$ GeV^{-1}). The effects of conventional shadowing ($R \simeq 5$ GeV^{-1}) will probably not be visible at HERA, whilst the situation for strong shadowing is not so clear. The outcome, in this case, will depend on the size of the (as yet uncalculated) higher-order shadowing terms.

We have compared our numerical solutions with some of the approximations that are used at small x. As a result, we find that the Altarelli-Parisi equations can be used to generate the correct Q^2 dependence of the gluon distribution, provided they are based on an input which contains the appropriate small x behaviour. However, we note that the

semi-classical approximation is not reasonable at the (non-asymptotic) values of $1/x$ and $\ln Q^2$ relevant to modern experiments. In particular, the notion of a critical line dividing the perturbative and non-perturbative regions of the (x, Q^2) plane is not valid at HERA energies.

We have pointed out that the measurement of a steep gluon distribution at HERA should not be taken as conclusive proof of the predicted $x^{-\lambda}$ behaviour. This is due to the ambiguities arising from the non-perturbative nature of the initial gluon distribution. We have therefore examined the proposal that a more reliable probe of the small x behaviour can be obtained from the measurement of deep-inelastic scattering events with an extra jet. These events require the transverse momentum of the jet, k_T^2, to be of the same order as the photon virtuality, Q^2, and the ratio, $z \equiv x/x_j$, to be as small as possible. This procedure should enable an unambiguous identification of the Lipatov Pomeron, free from the uncertainties of its coupling to the (non-perturbative) proton. The $z^{-\lambda}$ growth of the Lipatov Pomeron dramatically modifies both the shape and the normalization of the jet spectrum, although once again the normalization is dependent on an infra-red cut-off. The shape of the jet spectrum is much less sensitive to this cut-off, however, which enters only through $\lambda(k_0^2)$. The large increase in the jet cross section indicates that the effect could be observed and so we have examined the feasability of measuring these events at the HERA collider. From the results of our study we are able to conclude that this should indeed be possible and will be most noticable in the region where $x \lesssim 2 \times 10^{-3}$, and $x_j \gtrsim 0.05$ (so that $z \lesssim 0.04$) and $k_T^2 \simeq Q^2 \simeq 40$ GeV^2.

There is, still much work to be done before we have a thorough understanding of small x physics. The experiments currently in progress at HERA will help to answer some of our questions, but will undoubtedly raise many new ones. Nevertheless, we confidently expect that our knowledge of parton distributions, and in particular their behaviour at small x, will undergo enormous progress in the next few years.

Appendix A

The Drell-Yan cross-section at next-to-leading order

The expressions for the differential cross-sections of the Drell-Yan process to order α_s are given in the literature [16] in the DIS factorization scheme. Here we present the equations for both $d\sigma/dQ^2dx_F$ and $d\sigma/dQ^2dy$ to order α_s in the $\overline{MS}$ scheme. We separate the expressions into the contributions from $q\bar{q}$ annihilation processes and Compton processes

$$\frac{d\sigma^A}{dQ^2dx_F} = \frac{4\pi\alpha^2}{9Q^2s}\sum_i e_i^2 \int_{x_1}^1 dt_1 \int_{x_2}^1 dt_2 \left(\frac{d\hat{\sigma}^{DY}}{dQ^2dx_F} + \frac{d\hat{\sigma}^A}{dQ^2dx_F}\right) \times [q_i(t_1,Q^2)\bar{q}_i(t_2,Q^2) + \bar{q}_i(t_1,Q^2)q_i(t_2,Q^2)] \tag{A.1}$$

and

$$\frac{d\sigma^C}{dQ^2dx_F} = \frac{4\pi\alpha^2}{9Q^2s}\sum_i e_i^2 \int_{x_1}^1 dt_1 \int_{x_2}^1 dt_2 \left(\frac{d\hat{\sigma}^C}{dQ^2dx_F}\, g(t_1,Q^2)\,[q_i(t_2,Q^2) + \bar{q}_i(t_2,Q^2)] + 1 \leftrightarrow 2\right), \tag{A.2}$$

where the leading order Drell-Yan term in Eq. (A.1) is

$$\frac{d\hat{\sigma}^{DY}}{dQ^2dx_F} = \frac{1}{(x_1+x_2)}\,\delta(t_1-x_1)\delta(t_2-x_2). \tag{A.3}$$

The contribution from the order α_s annihilation graphs is

$$\begin{aligned}\frac{d\hat{\sigma}^A}{dQ^2dx_F} =& \tfrac{1}{2}A\frac{\delta(t_1-x_1)\delta(t_2-x_2)}{(x_1+x_2)}\Big[-8+\tfrac{1}{3}\pi^2+\ln^2(1-x_1)+\ln^2(1-x_2)+2\mathrm{Li}_2(x_1)\\ &+2\mathrm{Li}_2(x_2)+2\ln\frac{x_1}{1-x_1}\ln\frac{x_2}{1-x_2}\Big] + \tfrac{1}{2}A\,\frac{\delta(t_2-x_2)}{(x_1+x_2)}\Big[\frac{t_1^2+x_1^2}{t_1^2(t_1-x_1)_+}\ln\frac{(x_1+x_2)(1-x_2)}{x_2(t_1+x_2)}\\ &+\frac{1}{t_1}-\frac{x_1}{t_1^2}-\frac{t_1^2+x_1^2}{t_1^2(t_1-x_1)}\ln\frac{x_1}{t_1}+\frac{t_1^2+x_1^2}{t_1^2}\left(\frac{\ln(1-x_1/t_1)}{t_1-x_1}\right)_+\Big]\\ &+(1\leftrightarrow 2)+\tfrac{1}{2}A\Big[\frac{\tilde{G}^A(t_1,t_2)}{[(t_1-x_1)(t_2-x_2)]_+}+\tilde{H}^A(t_1,t_2)\Big],\end{aligned} \tag{A.4}$$

where $A = 4\alpha_s(Q^2)/3\pi$ and the dilogarithm function, $\mathrm{Li}_2(x)$, is defined by

$$\mathrm{Li}_2(x) = -\int_0^x \mathrm{d}t\, \frac{\ln(1-t)}{t}\,. \tag{A.5}$$

The functions $\tilde{G}^{\mathrm{A}}$ and $\tilde{H}^{\mathrm{A}}$ are given by

$$\tilde{G}^{\mathrm{A}}(t_1,t_2) = \frac{(t_1+t_2)(\tau^2+(t_1t_2)^2)}{(t_1t_2)^2(t_1+x_2)(t_2+x_1)}\,, \tag{A.6}$$

$$\tilde{H}^{\mathrm{A}}(t_1,t_2) = \frac{-2}{t_1t_2(t_1+t_2)}\,. \tag{A.7}$$

The contribution from the Compton graphs is

$$\begin{aligned}\frac{\mathrm{d}\hat{\sigma}^C}{\mathrm{d}Q^2\mathrm{d}x_{\mathrm{F}}} =& \tfrac{3}{16}\mathrm{A}\frac{\delta(t_2-x_2)}{(x_1+x_2)t_1^3}\left[(x_1^2+(t_1-x_1)^2)\ln\frac{(x_1+x_2)(1-x_2)(t_1-x_1)}{x_1x_2(t_1+x_2)}+t_1^2\right]\\ &+\tfrac{3}{16}\mathrm{A}\left[\frac{\tilde{G}^{\mathrm{C}}(t_1,t_2)}{(t_2-x_2)_+}+\tilde{H}^{\mathrm{C}}(t_1,t_2)\right],\end{aligned} \tag{A.8}$$

with

$$\tilde{G}^{\mathrm{C}}(t_1,t_2) = \frac{\tau^2+(t_1t_2-\tau)^2}{t_1^3t_2^2(t_2+x_1)}\,, \tag{A.9}$$

$$\tilde{H}^{\mathrm{C}}(t_1,t_2) = \frac{1}{(t_1t_2)^2(t_1+t_2)^2}[t_1(t_2+x_1)(t_2-x_2)+2\tau(t_1+t_2)]. \tag{A.10}$$

The '+' distributions are defined by

$$\int_x^1 \mathrm{d}t\, \frac{f(t)}{(t-x)_+} = \int_x^1 \mathrm{d}t\, \frac{f(t)-f(x)}{t-x}\,, \tag{A.11}$$

$$\int_x^1 \mathrm{d}t\, f(t)\left(\frac{\ln(1-x/t)}{t-x}\right)_+ = \int_x^1 \mathrm{d}t\, (f(t)-f(x))\left(\frac{\ln(1-x/t)}{t-x}\right), \tag{A.12}$$

and

$$\begin{aligned}&\int_{x_1}^1 \mathrm{d}t_1 \int_{x_2}^1 \mathrm{d}t_2\, \frac{f(t_1,t_2)}{[(t_1-x_1)(t_2-x_2)]_+}\\ &\quad= \int_{x_1}^1 \mathrm{d}t_1 \int_{x_2}^1 \mathrm{d}t_2\, \frac{[f(t_1,t_2)-f(t_1,x_2)-f(x_1,t_2)+f(x_1,x_2)]}{(t_1-x_1)(t_2-x_2)}\,.\end{aligned} \tag{A.13}$$

Similarly for $\mathrm{d}\sigma/\mathrm{d}Q^2\mathrm{d}y$ we have

$$\frac{\mathrm{d}\sigma^A}{\mathrm{d}Q^2\mathrm{d}y} = \frac{4\pi\alpha^2}{9Q^2s}\sum_i e_i^2 \int_{x_1}^1 dt_1 \int_{x_2}^1 dt_2 \left(\frac{\mathrm{d}\hat{\sigma}^{DY}}{\mathrm{d}Q^2\mathrm{d}y} + \frac{\mathrm{d}\hat{\sigma}^A}{\mathrm{d}Q^2\mathrm{d}y}\right) \times [q_i(t_1,Q^2)\bar{q}_i(t_2,Q^2) + \bar{q}_i(t_1,Q^2)q_i(t_2,Q^2)] \tag{A.14}$$

and

$$\frac{\mathrm{d}\sigma^C}{\mathrm{d}Q^2\mathrm{d}y} = \frac{4\pi\alpha^2}{9Q^2s}\sum_i e_i^2 \int_{x_1}^1 dt_1 \int_{x_2}^1 dt_2 \left(\frac{\mathrm{d}\hat{\sigma}^C}{\mathrm{d}Q^2\mathrm{d}y}\, g(t_1,Q^2)\,[q_i(t_2,Q^2) + \bar{q}_i(t_2,Q^2)] + 1 \leftrightarrow 2\right), \tag{A.15}$$

where now the leading order Drell-Yan term in Eq. (A.14) is

$$\frac{\mathrm{d}\hat{\sigma}^{DY}}{\mathrm{d}Q^2\mathrm{d}y} = \delta(t_1 - x_1)\delta(t_2 - x_2)\,. \tag{A.16}$$

The contribution from the order α_s annihilation graphs is

$$\begin{aligned}\frac{\mathrm{d}\hat{\sigma}^{\mathrm{A}}}{\mathrm{d}Q^2\mathrm{d}y} =& \tfrac{1}{2}\mathrm{A}\,\delta(t_1 - x_1)\delta(t_2 - x_2)\Big[-8 + \tfrac{1}{3}\pi^2 + \ln^2(1-x_1) + \ln^2(1-x_2) + 2\mathrm{Li}_2(x_1) \\ &+2\mathrm{Li}_2(x_2) + 2\ln\frac{x_1}{1-x_1}\ln\frac{x_2}{1-x_2}\Big] + \tfrac{1}{2}\mathrm{A}\,\delta(t_2 - x_2)\Big[\frac{t_1^2 + x_1^2}{t_1^2(t_1 - x_1)_+}\ln\frac{2x_1(1-x_2)}{x_2(t_1+x_1)} \\ &+\frac{1}{t_1} - \frac{x_1}{t_1^2} - \frac{t_1^2 + x_1^2}{t_1^2(t_1 - x_1)}\ln\frac{x_1}{t_1} + \frac{t_1^2 + x_1^2}{t_1^2}\left(\frac{\ln(1 - x_1/t_1)}{t_1 - x_1}\right)_+\Big] \\ &+(1 \leftrightarrow 2) + \mathrm{A}\Big[\frac{G^{\mathrm{A}}(t_1,t_2)}{[(t_1 - x_1)(t_2 - x_2)]_+} + H^{\mathrm{A}}(t_1,t_2)\Big],\end{aligned} \tag{A.17}$$

where the functions G^{A} and H^{A} are given by

$$G^{\mathrm{A}}(t_1,t_2) = \frac{(\tau + t_1t_2)(\tau^2 + (t_1t_2)^2)}{(t_1t_2)^2(t_1 + x_1)(t_2 + x_2)}\,, \tag{A.18}$$

$$H^{\mathrm{A}}(t_1,t_2) = \frac{-2\tau(\tau + t_1t_2)}{t_1t_2(t_1x_2 + t_2x_1)^2}\,. \tag{A.19}$$

The contribution from the Compton graphs is

$$\begin{aligned}\frac{\mathrm{d}\hat{\sigma}^C}{\mathrm{d}Q^2\mathrm{d}y} =& \tfrac{3}{8}\mathrm{A}\,\delta(t_2 - x_2)\Big[\frac{x_1^2 + (t_1 - x_1)^2}{2t_1^3}\ln\frac{2(1-x_2)(t_1 - x_1)}{x_2(t_1 + x_1)} + \frac{1}{2t_1}\Big] \\ &+\tfrac{3}{8}\mathrm{A}\Big[\frac{G^{\mathrm{C}}(t_1,t_2)}{(t_2 - x_2)_+} + H^{\mathrm{C}}(t_1,t_2)\Big],\end{aligned} \tag{A.20}$$

with

$$G^{C}(t_1,t_2) = \frac{x_2(\tau + t_1 t_2)(\tau^2 + (\tau - t_1 t_2)^2)}{t_1^3 t_2^2 (t_1 x_2 + t_2 x_1)(t_2 + x_2)} , \tag{A.21}$$

$$H^{C}(t_1,t_2) = \frac{\tau(\tau + t_1 t_2)(t_1 t_2^2 x_1 + \tau(t_1 x_2 + 2 t_2 x_1))}{(t_1 t_2)^2 (t_1 x_2 + t_2 x_1)^3} , \tag{A.22}$$

and $A = 4\alpha_s(Q^2)/3\pi$ as before.

Appendix B

A method for the numerical solution of the Lipatov equation

The Lipatov equation, with a fixed coupling constant can be solved analytically with the aid of Mellin transform techniques [48, 51, 68]. However, when one includes a running coupling constant then it is necessary to resort to numerical methods. In this appendix we present one possible method for the numerical solution of the Lipatov equation. This is the method used in Chapter 6 to obtain solutions for the gluon distribution inside the proton and in Chapters 7 and 8 to determine the behaviour of the Lipatov Pomeron.

We begin by studying the case in which no shadowing corrections are present in the evolution equation. We take as our example the Lipatov equation of (5.25), namely

$$\frac{\partial f(x,k^2)}{\partial \ln(1/x)} = \frac{3\alpha_s(k^2)}{\pi}\, k^2 \int_{k_0^2}^{k_F^2} \frac{dk'^2}{k'^2}\left[\frac{f(x,k'^2)-f(x,k^2)}{|k'^2-k^2|} + \frac{f(x,k^2)}{(4k'^4+k^4)^{\frac{1}{2}}}\right] \tag{B.1}$$

Our first step is to approximate the function $f(x,k^2)$ by a series of n Chebyshev polynomials, $T_i(\tau)$, between k_0^2 and the high k^2 cut-off, k_F^2. Chebyshev polynomials are well suited to this type of problem as the error, introduced by the truncation of their series at finite n, is amongst the smallest of all polynomials. We write $f(x,k^2)$ as

$$f(x,k^2) \;=\; \sum_{i=0}^{n-1} \nu_i\, a_i(x)\, T_i(\tau(k^2)) \tag{B.2}$$

where

$$\nu_i \;=\; \begin{cases} \frac{1}{2} & i=0 \\ 1 & i \geq 1 \end{cases} \tag{B.3}$$

The argument, τ, of each Chebyshev polynomial, $T_i(\tau)$, ranges from -1 to 1 and so we

need to perform the following change of variable

$$\tau(k^2) = -1 + 2\,\frac{\ln(k^2/k_0^2)}{\ln(k_F^2/k_0^2)} \tag{B.4}$$

Consequently, $\tau(k^2)$ varies linearly from -1 to $+1$ as $\ln(k^2)$ varies from $\ln(k_0^2)$ to $\ln(k_F^2)$. The (x dependent) coefficients $a_i(x)$ are given by

$$a_i(x) \;=\; \frac{2}{n}\sum_{j=0}^{n-1} T_i(\tau_j)\, f_j(x) \tag{B.5}$$

where the τ_j are simply the nodes of the nth order Chebyshev polynomial

$$\tau_j = \cos\left(\frac{2j+1}{2n}\,\pi\right) \tag{B.6}$$

and the function $f_j(x)$ is just the value of $f(x,k^2)$ at these nodes. When we insert the approximation (B.2) into Eq. (B.1) we obtain

$$\frac{\partial f(x,k^2)}{\partial \ln(1/x)} \;=\; \frac{3\alpha_s(k^2)}{\pi}\,k^2\sum_{i=0}^{n-1}\nu_i\left[\mathcal{I}_i^{(1)} \;+\; T_i(\tau(k^2))\,\mathcal{I}^{(2)}(k_0^2,k_F^2,k^2)\right] \tag{B.7}$$

where

$$\mathcal{I}_i^{(1)}(k_0^2,k_F^2,k^2) \;=\; \int_{k_0^2}^{k_F^2}\frac{\mathrm{d}k'^2}{k'^2}\left(\frac{T_i(\tau(k'^2)) - T_i(\tau(k^2))}{|k'^2-k^2|}\right). \tag{B.8}$$

and

$$\begin{aligned}\mathcal{I}^{(2)}(k_0^2,k_F^2,k^2) \;&=\; \int_{k_0^2}^{k_F^2}\frac{dk'^2}{k'^2}\,\frac{1}{k'^2(4k'^4+k^4)^{\frac{1}{2}}}\\ &=\; \frac{1}{2k^2}\left[\ln\left(\frac{\sqrt{k^4+4k_F^4}-k^2}{\sqrt{k^4+4k_F^4}+k^2}\right) - \ln\left(\frac{\sqrt{k^4+4k_0^4}-k^2}{\sqrt{k^4+4k_0^4}+k^2}\right)\right]\end{aligned} \tag{B.9}$$

The integration of Eq. (B.1) is thus converted into a series of integrations over Chebyshev polynomials and these can easily be computed. Equation (B.7) can now be written as a set of linear differential equations

$$\frac{\partial f(x,k^2)}{\partial \ln(1/x)} = \sum_{j=0}^{n-1}\mathcal{B}_j(k^2)\,f_j(x) \tag{B.10}$$

where the $\mathcal{B}_j(k^2)$ are known functions of k^2. Given an initial function $f(x_0,k^2)$, it is thus possible to solve these differential equations using standard numerical techniques such as the Runge-Kutta method [78].

Appendix B : A method for the numerical solution of the Lipatov equation

The inclusion in the evolution equation of shadowing terms which behave as $xg^2(x,k^2)$ is straightforward. It only requires that we reconstruct the gluon distribution from

$$xg(x,k^2) = \int_{k_0^2}^{k^2} \frac{dk'^2}{k'^2} f(x,k'^2) \tag{B.11}$$

at each step of the calculation and then subtract the appropriate term from the linear part of the equation.

References

1. M. Gell-Mann, Phys. Lett. **8** 214 (1964); G. Zweig, CERN *Rep.* 8182/TH 401.

2. For a review of the early experiments, see J. Friedman and H. Kendall, Ann. Rev. Nucl. Sci. **22**, 203 (1972).

3. R. Feynman, Photon-hadron interaction. Benjamin, Reading, Massachusetts

4. EMC collab., J.J. Aubert *et al.*, Nucl. Phys. **B259** 189 (1985); Nucl. Phys. **B293** 740 (1987); Nucl. Phys. **B321** 541 (1989); BCDMS collab., A.C Benvenuti *et al.*, Phys. Lett. **B223** 485 (1989); Phys. Lett. **B237** 599 (1990); NMC collab., P. Amaudruz *et al*, Nucl. Phys. **B371** 3 (1992);

5. See, for example, F. Close, *Introduction to quarks and partons.* Academic Press, New York (1979); F. Halzen and A.D. Martin *Quarks and Leptons.* Wiley, New York (1984).

6. E. Berger and S. Brodsky, Phys. Rev. Lett.**42** 940 (1979); E. Berger, Z. Phys. **C4** 289 (1980).

7. Yu. L. Dokshitzer, Phys. Rep. **58**, 269 (1980).

8. G. Altarelli ,and G. Parisi, Nucl. Phys. **B126**, 298 (1977); Yu. L. Dokshitzer, Zh. Eksp. Teor. Fiz. **73**, 1216 (1977) [Sov. Phys. JETP **46**, 641 (1977)]; V. Gribov and L. Lipatov, Yad. Fiz. **15**, 137 (1973) [Sov. J. Nucl. Phys. **15**, 78 (1972)]; L. Lipatov, *ibid.* **20**, 340 (1974) [**20**, 181 (1974)].

9. CCFR collaboration, C. Foudas *et al.*, Phys. Rev. Lett. **64**, 1207 (1990).

10. S. Brodsky and G. Farrar Phys. Rev. Lett. **31**, 1153 (1973).

11. I. R. Kenyon Rep. Prog. Phys., **45**, 1261 (1982).

12. P. Aurenche, R. Baier and M. Fontannaz Phys. Rev. **D42**, 1140 (1990).

13. J. Christenson et al., Phys. Rev. Lett. 25, 1523 (1970).

14. S. Drell and T. Yan Phys. Rev. Lett. **25** 316 (1970).

15. G. Altarelli, R.K. Eliis and G. Martinelli, Nucl. Phys. **B157** 461 (1979).

16. J. Kubar, M. Le Bellac, J.L. Meunier and G. Plaut, Nucl. Phys. **B175**, 251 (1980).

17. R. Hamberg, W.L. van Neerven and T. Matsuura, Nucl. Phys. **B359**, 343 (1991).

18. K. Freudenreich, Int. J. Mod. Phys. **A19**, 3643 (1990).

19. E605 Collaboration, C. Brown *et al.*, Phys. Rev. Lett. 63, 2637 (1989).

20. NA10 collab., B. Betev *et al.*, Z. Phys. **C28**, 9 (1985). Note that the cross-sections in this paper have since been revised with a better estimate of Fermi motion effects; see, for example, [18].

21. E615 collaboration., J.S. Conway *et al.*, Phys. Rev. **D39**, 92 (1989).

22. EMC collab., J.J. Aubert *et al.*, Phys. Lett. **B123** 275 (1983).

23. E772 collab., D.M. Alde *et al.*, Phys. Rev. Lett. **64** 2479 (1990).

24. P. Aurenche *et al.*, Phys. Lett. **B140**, 87 (1984); Phys. Lett. **B169**, 441 (1986); Nucl. Phys. **B297**, 661 (1988).

25. P.M. Stevenson and H.D. Politzer, Nucl. Phys. **B277**, 758 (1986).

26. For a review of the early prompt photon data see T. Ferbel and W.R. Molzon, Rev. Mod. Phys. **56** 181 (1984).

27. P. Aurenche and M. Whalley, Rutherford preprint RAL-89-106 (1989).

28. WA70 collaboration., M. Bonesini *et al.*, Z. Phys. **C37**, 535 (1988).

29. UA2 collab., J.Alitti *et al.*, Phys. Lett. **B263**, 544 (1991); Phys. Lett. **B288**, 386 (1992).

30. E706 collab., G. Alverson it al., Phys. Rev. Lett. **68** , 2584 (1992).

31. CDF collab., F. Abe *al.*, Phys. Rev. Lett. **68**, 2734 (1992).

32. A.D. Martin, R.G. Roberts and W.J. Stirling, Durham preprint DTP/92/16 (1992); M. Diemoz, F. Ferroni, E. Longo and G. Martinelli, Z. Phys. **C39**, 21 (1988); P. Aurenche, R. Baier, M. Fontannaz, J.F. Owens and M. Werlen, Phys. Rev. **D39**, 3275 (1989); J. Morfin and Wu-ki Tung, Fermilab preprint 90/74 (1990).

33. NA3 collab., J. Badier *et al.*, Z. Phys. **C18**, 281 (1983); J.F. Owens, Phys. Rev. **D30**, 943 (1984); NA10 collaboration., B. Betev *et al.*, Z. Phys. **C28**, 15 (1985); P. Aurenche, R. Baier, M. Fontannaz, M.N. Kienzle-Focacci and M. Werlen Phys. Lett. **B233**, 517 (1989); E615 collaboration., J.S. Conway *et al.*, Phys. Rev. **D39**, 92 (1989).

34. P.N. Harriman, A.D. Martin, W.J. Stirling and R.G. Roberts, Phys. Rev. **D42**, 798 (1990) [HMRS].

35. P. Aurenche, R. Baier, M. Fontannaz, M.N. Kienzle-Focacci and M. Werlen Phys. Lett. **B233**, 517 (1989).

36. NA10 collaboration., P. Bordalo *et al.*, Phys. Lett. **B193**, 368 (1987).

37. A.D. Martin, R.G. Roberts and W.J. Stirling, Phys. Rev. **D43**, 3648 (1991).

38. NA3 collab., J. Badier *et al.*, Z. Phys. **C18**, 281 (1983).

39. J.F. Owens, Phys. Rev. **D30**, 943 (1984).

40. G. Martinelli and C.T. Sachrajda, Nucl. Phys. **B306**, 865 (1988).

41. H. Plothow-Besch, Proceedings of the 3rd Workshop on Detector and Event Simulation in High Energy Physics, Amsterdam, April 1991.

42. P.J. Sutton, A.D. Martin, R.G. Roberts and W.J. Stirling, Phys. Rev. **D45** , 2349 (1992).

43. J. Bartels and E. Levin, DESY preprint DESY-92-033 (1992).

44. T. Regge, Nuovo Cimento **14** 951 (1959); Nuovo Cimento **18** 947 (1960);

45. M. Froissart, Phys. Rev. **123** 1053 (1961).

46. I. Pomeranchuk, Sov. Phys. JETP **7** 499 (1958).

47. F.J. Gilman, Phys. Rep. **4C** 95 (1972)

48. E.A. Kuraev, L.N. Lipatov and V.S. Fadin, Sov. Phys. JETP **45**, 199 (1977); Ya.Ya. Balitsky and L.N. Lipatov, Sov. J. Nucl. Phys. **28**, 822 (1978); J.B. Bronzan and R.L. Sugar, Phys. Rev. **D17**, 585 (1978); T. Jaroszewicz, Acta. Phys. Polon. **B11**, 965 (1980); M. Ciafaloni, Nucl. Phys. **B296**, 49 (1988); S. Catani, F. Fiorani and G. Marchesini, Phys. Lett. **B234**, 339 (1990); Nucl. Phys. **B336**, 18 (1990).

49. L.N. Lipatov in Perturbative Chromodynamics ed. A.H. Mueller (World Scientific, 1989) p. 411.

50. J. Kwiecinski, A.D. Martin, W.J. Stirling and R.G. Roberts, Phys. Rev. **D42**, 3645 (1990).

51. L.V. Gribov, E.M. Levin and M.G. Ryskin, Phys. Rep. **100**, 1 (1983).

52. J.C. Collins and P.V. Landshoff, Phys. Lett. **276B**, 196 (1992).

53. R.E. Hancock and D.A. Ross, Southampton University preprint SHEP 91/92-14

54. Ya.Ya. Balitzkij and L. Lipatov, Sov. J. Nucl. Phys.. **28** 822 (1978); J.B. Bronzan and R.L. Sugar, Phys. Rev. **D17** 585 (1978); L. Lipatov, Sov. Phys. JETP **63** 904 (1986); T. Jaroszewicz, Acta Phys. Polon. **11** 965 (1980); L.N. Lipatov in Perturbative Chromodynamics ed. A.H. Mueller (World Scientific, 1989) p. 411.

55. J.C. Collins and J. Kwiecinski, Nucl. Phys. **B316**, 307 (1989).

56. A.D. Martin, R.G. Roberts and W.J. Stirling, Durham preprint DTP/92/16 (1992).

57. A.H. Mueller and J. Qiu, Nucl. Phys. **B268**, 427 (1986).

58. A.H. Mueller, Nucl. Phys. **B335** 119 (1990).

59. Proc. of the Workshop on Physics at HERA, DESY, Hamburg, Oct. 1991, eds. W. Buchmüller and G. Ingelman.

60. E.M. Levin and M.G. Ryskin, Phys. Rep. **189** 267 (1990); A.H. Mueller and J. Qiu, Nucl. Phys. **B268**, 427 (1986).

61. L.V. Gribov, E.M. Levin and M.G. Ryskin, Zh. Eksp. Teor. Fiz. **80**, 2132 (1981) [Sov. Phys. JETP **53**, 1113 (1981)]; L.V. Gribov, E.M. Levin and M.G. Ryskin, Phys. Rep. **100**, 1 (1983); L.V. Gribov, E.M. Levin and M.G. Ryskin, Nucl. Phys. **B188**, 155 (1981)

62. J. Kwiecinski, A.D. Martin and P.J. Sutton, Phys. Lett. **B264**, 199 (1991); Phys. Rev. **D44**, 2640 (1991).

63. I.N. Sneddon, *Elements of partial differential equations*, McGrw-Hill, New York, (1957).

64. Proceedings of the HERA Workshop, DESY, Hamburg, Germany, 1987, ed. by R.D. Peccei.

65. A.H. Mueller, Nucl. Phys. B (Proc. Suppl.) **18C**, 125 (1990); J. Phys. **G17**, 1443 (1991).

66. J. Kwiecinski, A.D. Martin and P.J. Sutton, Phys. Rev. **D46**, 921 (1992).

67. J. Bartels, A. De Roeck and M. Loewe, Z. Phys. C (in press); W.-K. Tang, Phys. Lett. **B278**, 363 (1992); S. Catani, M. Ciafaloni and F. Hautmann, Proc. of the Workshop on Physics at HERA, DESY, Hamburg, Oct. 1991, eds. W. Buchmüller and G. Ingelman.

68. L.V. Gribov, E.M. Levin and M.G. Ryskin, Nucl. Phys. **B188**, 155 (1981); Sov. Phys. JETP **53**, 1113 (1981); A.H. Mueller and J. Qiu, Nucl. Phys. **B268**, 427 (1986); A.H. Mueller, Nucl. Phys. **B335**, 115 (1990).

69. B.R. Webber, talk at the Eloisatron Workshop "QCD at 200 TeV", Erice, Italy, June 1991, Cavendish preprint HEP-91/9.

70. S. Catani, M. Ciafaloni and F. Hautmann, Phys. Lett. **B242**, 97 (1990); Nucl. Phys. **B366**, 135 (1991); J.C. Collins and R.K. Ellis, Nucl. Phys. **B360**, 3 (1991); B.R. Webber, Proc. of the Workshop on Physics at HERA, DESY, Hamburg, Oct. 1991, eds. W. Buchmüller and G. Ingelman .

71. R.K. Ellis and D.A. Ross, Nucl. Phys. **B345**, 79 (1990).

72. A.D. Martin, C.-K. Ng and W.J. Stirling, Phys. Lett. **B191**, 200 (1987); Z. Kunszt, Phys. Lett. **B207**, 103 (1988); K.J. Abraham, Phys. Lett. **B240**, 224 (1990).

73. A.H. Mueller and H. Navelet, Nucl. Phys. B**282**, 727 (1987).

74. F. Jaquet and A. Blondel, "An *ep* facility for Europe", Proceedings, Hamburg, ed. U. Amaldi (1979).

75. S. Bentvelson, J. Engelen and P. Kooijman, Proc. of the Workshop on Physics at HERA, DESY, Hamburg, Oct. 1991, eds. W. Buchmüller and G. Ingelman.

76. J. Bartels, J. Blümlein and G. Schuler, Z. Phys. **C50**, 91 (1991).

77. M. Klein, Proc. of the Workshop on Physics at HERA, DESY, Hamburg, Oct. 1991, eds. W. Buchmüller and G. Ingelman.

78. W. Press, B. Flannery, S. Teukolsky and W. Vetterling, *Numerical Recipes—The art of scientific computing*, Cambridge University Press (1986).